Physically-Based Models for Two-Phase Flow Phenomena in Steam Injectors

A One-Dimensional Simulation Approach

David Heinze

KIT Scientific Publishing

David Heinze

Physically-Based Models for Two-Phase Flow Phenomena in Steam Injectors

A One-Dimensional Simulation Approach

Karlsruhe Institute of Technology

KIT SCIENTIFIC REPORTS 7704

Physically-Based Models for Two-Phase Flow Phenomena in Steam Injectors

A One-Dimensional Simulation Approach

by
David Heinze

Report-Nr. KIT-SR 7704

Impressum

KIT Scientific Publishing

Physically-Based Models for Two-Phase Flow Phenomena in Steam Injectors

A One-Dimensional Simulation Approach

Zur Erlangung des akademischen Grades

DOKTOR DER INGENIEURWISSENSCHAFTEN

der Fakultät für Maschinenbau
Karlsruher Institut für Technologie (KIT)

genehmigte

DISSERTATION

von

Dipl.-Ing. David Heinze

26.10.2015

Datum der mündlichen Prüfung: 17.07.2015
Hauptreferent: Prof. Dr.-Ing. Thomas Schulenberg
Koreferent: Prof. Dr.-Ing. Xu Cheng

ABSTRACT

Simulation models for the two-phase condensing flow in steam injectors are presented that allow determination of major flow parameters on a physically sound basis. The investigated phenomena are steam expansion, gas dynamic jet adaptation and direct contact condensation.

Steam expansion in convergent-divergent nozzles is calculated based on the classical nucleation theory in order to account for the non-equilibrium phenomenon of spontaneous condensation of the supersaturated steam. The employed droplet growth model takes into account effects in both the molecular and the continuum regime.

The initial shape of submerged over- and underexpanded steam jets is determined based on a homogeneous equilibrium model. Analytical ideal gas solutions for oblique shocks and Prandtl-Meyer expansion fans are used as initial estimate for an iterative solution based on the two-phase conservation equations.

Direct contact condensation of steam jets in pools and channels is modeled by taking into account steam condensation on entrained droplets and on the jet-water interface. Entrainment of water into the steam jet is determined based on the Kelvin-Helmholtz and Rayleigh-Taylor instability theories. Primary atomization due to acceleration of interfacial waves and secondary atomization due to aerodynamic forces account for the initial size of entrained droplets. An interfacial area transport equation is used to track changes of the interfacial area density due to droplet entrainment and steam condensation on droplets. Condensation at the interface between the steam jet and the surrounding water is calculated according to the surface renewal theory.

The one-dimensional conservation equations of the steam-water two-phase flow during steam expansion and direct contact condensation constitute systems of ordinary differential equations which are solved using Runge-Kutta algorithms. The simulation results are in good qualitative agreement with published experimental data over a wide parameter range without the need for adaptation to specific experimental conditions.

KURZFASSUNG

Es werden Modelle zur Simulation der kondensierenden Zweiphasenströmung in Dampfstrahlpumpen vorgestellt, mit deren Hilfen wichtige Strömungsgrößen auf physikalisch fundierter Basis ermittelt werden können. Die untersuchten Phänomene sind Dampfexpansion, gasdynamische Strahlanpassung und Direktkontakt-Kondensation.

Dampfexpansion in konvergent-divergenten Düsen wird auf Grundlage der klassischen Keimbildungstheorie modelliert, um den Nicht-Gleichgewichts-Vorgang der spontanen Kondensation des übersättigten Dampfes berücksichtigen zu können. Bei der Berechnung des Tropfenwachstums werden Austauschprozesse im Knudsen-Bereich sowie unter Kontinuumsbedingungen berücksichtigt.

Die Form von über- und unterexpandierten Dampfstrahlen beim Eintritt in Wasser wird mit Hilfe eines homogenen Gleichgewichts-Modells ermittelt. Analytische Lösungen der idealen Gasgleichungen für schiefe Verdichtungsstöße und Prandtl-Meyer-Expansionsfächer bilden dabei die Grundlage für eine iterative Lösung der zweiphasigen Erhaltungsgleichungen.

Die Modellierung der Direktkontakt-Kondensation von Dampfstrahlen in Wasserbecken und in Rohrströmungen erfolgt unter Berücksichtigung der Dampfkondensation an mitgerissenen Tropfen sowie an der Zweiphasengrenze zwischen Strahl und umgebendem Wasser. Tropfenmitriss wird mit Hilfe der Kelvin-Helmholtz- sowie Rayleigh-Taylor-Instabilitätstheorien berechnet. Primärzerstäubung durch Beschleunigung der Wellen an der Strahlgrenze und Sekundärzerstäubung durch aerodynamische Kräfte bilden die Grundlage zur Bestimmung der Tropfengröße. Eine Grenzflächentransportgleichung wird verwendet, um Änderungen der Grenzflächendichte aufgrund von Tropfenmitriss und Dampfkondensation an den Tropfen zu ermitteln. Kondensation an der Phasengrenze zwischen Dampfstrahl und Wasser wird anhand der Oberflächenerneuerungstheorie modelliert.

Die eindimensionalen Erhaltungsgleichungen der zweiphasigen Wasser-Dampf-Strömung während Dampfexpansion und Direktkontakt-Kondensation bilden Systeme gewöhnlicher Differentialgleichungen, die mit Hilfe von Runge-Kutta-Algorithmen gelöst werden. Die Simulationsergebnisse zeigen gute qualitative

Übereinstimmung mit veröffentlichten Experimenten, die einen breiten Werte-
bereich abdecken. Dabei war es nicht erforderlich, das Simulationsmodell an
spezifische experimentelle Randbedingungen anzupassen.

PUBLICATIONS

Some ideas and figures have appeared previously in the following publications:

Heinze, D., T. Schulenberg, and L. Behnke (2012). "Verwendung einer Dampf-strahlpumpe zur passiven Not- und Nachkühlung während eines Station Black-outs". In: *Tagungsband der Jahrestagung Kerntechnik 2012*. Stuttgart, Germany.

— (2013). "Modeling of steam expansion in a steam injector by means of the classical nucleation theory". In: *Proceedings of The 15th International Topical Meeting on Nuclear Reactor Thermal Hydraulics (NURETH-15)*. Pisa, Italy.

— (2014a). "Simulation of direct contact condensation of steam jets submerged in subcooled water by means of a one-dimensional two-fluid model". In: *Proceedings of the 10th International Conference on Heat Transfer, Fluid Mechanics and Thermodynamics (HEFAT2014)*. Orlando, USA.

— (2015). "A Physically Based, One-Dimensional Two-Fluid Model for Direct Contact Condensation of Steam Jets Submerged in Subcooled Water". In: *Journal of Nuclear Engineering and Radiation Science* 1.2, pp. 021002-1–021002-8.

Heinze, D., T. Schulenberg, A. Class, and L. Behnke (2014b). "Simulation of direct contact condensation of steam jets based on interfacial instability theories". In: *Bulletin of the American Physical Society*. Vol. 59. San Francisco, USA.

VORWORT

CONTENTS

ABBREVIATIONS AND ACRONYMS

CATHARE	Code for Analysis of THermalhydraulics during an Accident of Reactor and safety Evaluation (best estimate thermal-hydraulic code devoted to LWR accident analyses)
CFD	computational fluid dynamics
DCC	direct contact condensation
DNS	direct numerical simulation
ECCS	Emergency Core Cooling System
GRS	Gesellschaft für Anlagen- und Reaktorsicherheit
GSL	GNU Scientific Library (numerical library for C and C++ programmers)
HPCI	High-pressure Coolant Injection System (emergency core cooling system using a steam turbine-driven pump)
IAEA	International Atomic Energy Agency
IAPWS	International Association for the Properties of Water and Steam
IAPWS-IF97	IAPWS Industrial Formulation 1997 for the Thermodynamic Properties of Water and Steam
IC	Isolation Condenser (passive decay heat removal system based on natural circulation)
INES	International Nuclear and Radiological Event Scale
INPO	Institute of Nuclear Power Operations
ODE	ordinary differential equation
PHOENICS	Parabolic, Hyperbolic Or Elliptic Numerical Integration Code Series (multi-purpose computational fluid dynamics software package)
RCIC	Reactor Core Isolation Cooling System (auxiliary reactor makeup water supply system using a steam turbine-driven pump)

RELAP5/MOD3 Reactor Excursion and Leak Analysis Program (simulation tool for the analysis of transients and accidents in water-cooled nuclear power plants and related systems)

RPV reactor pressure vessel

SBO station blackout (complete loss of alternating current electric power in a nuclear power plant)

NOMENCLATURE

Latin symbols

A	flow cross section, m^2	
a	acceleration, m/s^2	
a_{if}	interfacial area density, m^2/m^3	
B	condensation driving potential – page 60	
b	wave crest thickness, m	
C	constant, coefficient	
c	velocity, m/s	
c_{dm}	dynamic mean velocity, m/s – page 66	
c_{km}	kinematic mean velocity, m/s – page 66	
c_p	specific isobaric heat capacity, $J/(kg\,K)$	
c_v	specific isochoric heat capacity, $J/(kg\,K)$	
Ct	Craya-Courtet number – page 66	
D	mass diffusivity, m^2/s	
d	diameter, m	
E_0	entrainment coefficient – page 65	
f	friction factor	
Fr	Froude number	
G	Gibbs free energy, J	
g	specific Gibbs free energy, J/kg	
h	specific enthalpy, J/kg	
J	mass-specific nucleation rate, $1/(kg\,s)$ – page 24	
k	wave number, 1/m	
L	dimensionless jet penetration length – page 57	
l	jet penetration length, m	
$\bar{l}$	mean free path of gas molecules, m	
l_m	mixing length, m – page 64	
M	volume-specific total interfacial shear force, $kg/(m^2\,s^2)$ – page 81	
m	mass, kg	
$\dot{M}$	mass flow rate, kg/s	
$\dot{m}$	mass flux, $kg/(m^2\,s)$	
Ma	Mach number	

n particle density, 1/kg

$\dot{n}$ particle flux, $1/(\text{m}^2\,\text{s})$

Nu Nusselt number

Oh Ohnesorge number

p pressure, Pa

Pr Prandtl number

$\dot{q}$ sensible heat flux, W/m^2

$\dot{q}_{tot}$ total heat flux, W/m^2

$\dot{Q}$ heat flow rate, J/s

R jet radius, m

r radius, radial distance, m

R_s specific gas constant, $\text{J}/(\text{kg}\,\text{K})$

Re Reynolds number

S saturation ratio – page 22

s specific entropy, $\text{J}/(\text{kg}\,\text{K})$

S_m transport modulus – page 60

Sc Schmidt number

St Stanton number

T temperature, K

t time, s

$\hat{t}$ dimensionless time

v specific volume, m^3/kg

w sonic velocity, m/s

W channel width in stratifed flow, m

We Weber number

x mass fraction

z axial distance, m

$\hat{z}_B$ buoyancy criterion – page 60

Greek symbols

α_{Ma} Mach angle

α heat transfer coefficient, $W/(m^2\,K)$

β mass transfer coefficient, m/s

Γ volumetric mass source term, $kg/(m^3\,s)$ – page 81

γ proportionality factor for the vorticity layer, $m^{1/2}$

Δ deviation, difference

δ thickness, m

ε coefficient of kinematic eddy viscosity, m^2/s – page 64

ϵ volume fraction

$\tilde{\epsilon}$ relative volume fraction – page 79

η auxiliary variable – page 45

Θ non-isothermal factor – page 25

ϑ channel inclination/deflection angle

θ shock angle

$\varkappa$ isentropic exponent

κ thermal diffusivity, m^2/s

λ thermal conductivity, $W/(m\,K)$

$\tilde{\lambda}$ wave length, m

μ dynamic viscosity, $kg/(m\,s)$

ν kinematic viscosity, m^2/s

ρ density, kg/m^3

σ surface tension, kg/s^2

τ shear stress, $kg/(m\,s^2)$

Φ interfacial area source term, $1/(m\,s)$ – page 83

φ azimuthal coordinate

ψ auxiliary variable – page 45

ω amplification rate, $1/s$

Subscripts and superscripts

$*$	critical value
$\odot$	molecule
$\hat{\ }$	post-shock property
$\perp$	normal
$\parallel$	tangential
2ph	two-phase flow region
∞	ambient fluid
0	stagnation condition
1	upstream, primary
2	downstream, secondary
20	surface-averaged mean value
30	volume-averaged mean value
32	Sauter-averaged mean value
b	burst
bbl	bubble
c	continuous phase
calc	calculated
CL	classical nucleation theory
co	condensation
crit	critical condition (at sonic velocity)
D	drag
d	dispersed phase
drp	droplet
e	nozzle exit condition
en	entrainment
ev	evaporation
exp	experimental
g	gas phase
H	hydraulic
h	homogeneous
if	interface property
ini	initiation
KH	Kelvin-Helmholtz
Kn	Knudsen layer
l	liquid phase
m	mixture property
max	maximum
me	mechanical equilibrium

min	minimum
ni	non-isothermal
RMS	root mean square
RT	Rayleigh-Taylor
sat	saturation
SR	surface renewal
τ	shear
t	turbulence
tot	total
w	water
wall	wall
wb	wet-bulb
x	horizontal
y	vertical

Physical constants

$d_{\odot,H_2O}$ diameter of a water molecule, $2.75 \times 10^{-10}\,\mathrm{m}$
k_B Boltzmann constant, $1.380\,648\,8 \times 10^{-23}\,\mathrm{J/kg}$
$m_{\odot,H_2O}$ mass of a water molecule, $2.9916 \times 10^{-26}\,\mathrm{kg}$
R_{s,H_2O} specific gas constant of water, $461.522\,27\,\mathrm{J/(kg\,K)}$

Considéré comme appareil d'alimentation des chaudières à vapeur, l'injecteur de M. Giffard est, sans contredit, le meilleur de tous ceux que l'on ait employés ou même que l'on puisse employer, comme il en est le plus ingénieux et le plus simple.

— Charles-Pierre-Mathieu Combes, "Sur l'injecteur automoteur de chaudières à vapeur imagine par M. Giffard", 1859

1 | MOTIVATION

On March 11th, 2011, the most severe earthquake since the beginning of corresponding records in Japan occurred off the east coast of the Japanese main island Honshū. The earthquake and the tsunami triggered by it claimed more than 18 000 lives and led to the destruction or damage of about one million buildings. On the nuclear power plant site Fukushima Daiichi, the event caused an almost complete loss of power supply at four of the total six boiling water reactors, resulting in a major accident (*International Nuclear and Radiological Event Scale* (INES) 7).

As far as is currently known, the loss of core cooling capabilities resulted in a local core destruction in Unit 2, a severe core destruction in Unit 3 and a complete core destruction in Unit 1 (Band et al., 2015). The following outline of the chain of events leading to these core destructions is based on the detailed reports (Band et al., 2015; INPO, 2011) by the *Gesellschaft für Anlagen- und Reaktorsicherheit* (GRS) and the *Institute of Nuclear Power Operations* (INPO).

Per design, the earthquake caused the automatic reactor shutdown ("scram") in all three units. Due to the loss of external power supply, the emergency diesel generators started as planned and the penetration isolation valves of the main steam valves closed. The subsequent pressure rise resulted in the intermittent operation of the *Isolation Condenser* (IC)[1] in Unit 1. In Units 2 and 3, the safety relief valves opened automatically for pressure control, and the *Reactor Core Isolation Cooling System* (RCIC)[2] began to operate intermittently.

Approximately forty-five minutes after the earthquake, the site was struck by several tsunami waves, which damaged the service water system and the emergency diesels. In Units 1 and 2, the battery-based power supply was incapacitated as well, while it remained partially functional in Unit 3.

In Unit 1, the IC was not in operation when this total loss of power ensued. Without battery power, it could not be restarted, and the operation of all other core cooling systems failed as well. Therefore, no water could be supplied to the *reactor pressure vessel* (RPV) for the next fourteen hours, until fire engines were deployed for water injection.

---

1   passive decay heat removal system based on natural circulation
2   auxiliary reactor makeup water supply system using a steam turbine-driven pump

In Unit 2, the RCIC was in operation at the time of the tsunami impact. The RCIC uses a steam turbine-driven pump and can thus feed water from the pressure suppression pool into the core without electric power supply. Therefore, core cooling could be ensured for four days, until the RCIC failed. Although the cause of failure is not clearly established yet, two probable explanations can be given. On the one hand, saturation conditions could have been reached in the pressure suppression pool, thus rendering the pump unusable. On the other hand, the uncontrolled operation of the RCIC after battery failure may have caused over-filling of the RPV, resulting in two-phase flow instead of vapor flow at the steam turbine inlet and subsequent turbine failure. In consequence of the RCIC malfunction, no water was supplied to the RPV for eleven hours until mobile pumps could be utilized.

In Unit 3, the tsunami did not destroy the complete battery supply, thus the RCIC could be started. However, it failed after twenty-one hours due to exceedance of the maximum steam turbine outlet pressure, thus initiating the automatic start of the steam-driven *High-pressure Coolant Injection System* (HPCI)[3]. Two days after the earthquake, the HPCI was deactivated in an unsuccessful attempt to switch to a mobile pump. Subsequently, neither RCIC nor HPCI could be started, thus no water was injected into the RPV until the mobile pump could be put to use approximately seven hours later.

The Fukushima accident amplified the interest and the research in means to ensure the heat removal from the reactor core during beyond-design scenarios such as a *station blackout* (SBO), when conventional pumping systems cannot be used due to the failure of external and emergency power supply (fig. 1.1). The steam turbine-driven RCIC and HPCI employed in the Fukushima power plants do not require electrical power and were able to mitigate the SBO consequences in Units 2 and 3. However, the vulnerability of these systems when operated beyond design limits is high, as demonstrated by the failure of the RCIC in Unit 2, and start-up may be impeded under these circumstances, as can be seen from the events in Unit 3. Hence, diversified, robust and electricity-independent systems are advantageous to increase the time available to initiate emergency procedures. The steam injector is an example of such systems, because it requires only steam for operation and can therefore make use of the reactor decay heat. It does not contain any rotating parts, and active components are limited to controls and valves for start-up. As such, it fulfills the criteria of a *category D passive system* as defined by the International Atomic Energy Agency (IAEA, 2009). Due to its compact build, the machine could potentially be used for retrofit measures in existing nuclear power plants.

---

3   emergency core cooling system using a steam turbine-driven pump
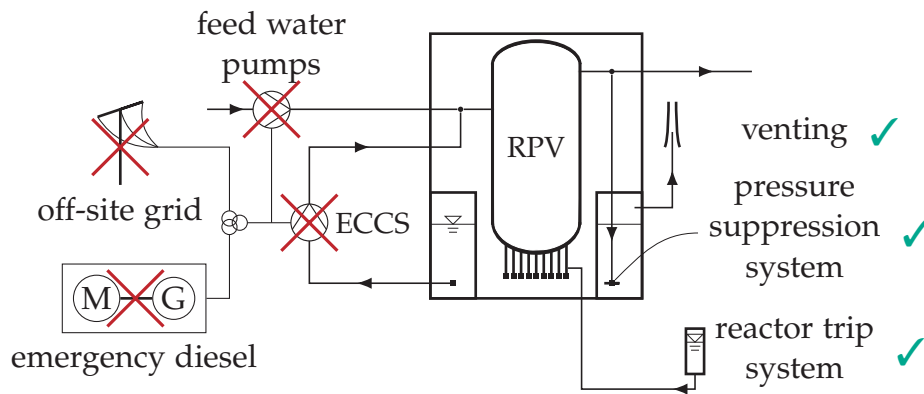
Figure 1.1: The station blackout is a beyond-design scenario with extremely small incidence rate. After a malfunction of the plant auxiliary power system, it is assumed that neither the subsequent automatic switch to off-site power is successful nor the redundant emergency diesel generators can be started. This results in a complete loss of alternating current electric power and thus failure of all electrically driven pumps, in particular the feed water pumps and the motor-driven pumps of the *Emergency Core Cooling System* (ECCS). The uninterrupted power supply of the reactor protection system is guaranteed by batteries and the automatic reactor shutdown is ensured by pressurized tanks. The subsequent pressure increase in the *reactor pressure vessel* (RPV) automatically triggers the pressure control and finally the fill level dependent pressure relief function of the pressure suppression system. Venting can be used for pressure relief of the primary containment via the pressure suppression pool.

Although the mechanical design of the steam injector is straightforward, it is characterized by a complex two-phase flow, and a discharge pressure which is sufficiently high for residual heat removal can only be achieved if the steam injector is applied under optimized conditions. Accordingly, additional research is required to study the operating behavior of the injector, its impact on the water level in the reactor core and to identify the ideal boundary conditions that permit using the injector for emergency core cooling.

Predictions of the performance of steam injectors as well as their reliable operation require a simulation model of the injector that can be integrated into thermalhydraulic system codes for further analysis. Main requirements on a such-like model are the accurate prediction of the major fluid-dynamic parameters (first and foremost the pressure rise of the suction water) and a high simulation speed. For these reasons, the motivation of the present work is the development of a universally valid, computationally efficient simulation model. To this end, the crucial physical phenomena occurring in steam injectors are identified and suitable model approaches are presented.

The *working principle of the steam injector* is described in chapter 2 and results of previous studies, both experimental and theoretical, are summarized. In the

subsequent three chapters, physically-based models for two-phase flow phenomena in different parts of the injector are developed: *Homogeneous nucleation and spontaneous condensation* during steam expansion (chapter 3), *oblique shocks and Prandtl-Meyer expansions* at the steam nozzle exit (chapter 4), and *direct contact condensation* of steam in the mixing chamber (chapter 5). Each of these chapters begins with a comprehensive literature review and a description of the occurring physical processes. Previous studies in related fields of fluid-dynamic research are presented where relevant. The insights gained in this manner are then extended and consolidated to develop suitable model approaches. Lastly, the simulation results obtained by these models are validated by comparison with published experiments. In chapter 6, first steps towards a *complete steam injector simulation model* are presented and the preliminary results for the pressure profile of a steam injector are compared to experimental data. Finally, a *conclusion* of the work is given in chapter 7.

Seldom has an invention caused so much astonishment and wild speculation among mechanics, and even among scientists, as the injector did [. . .]. It was regarded as a case of perpetual motion—the means of doing work without power, or, as Americans expressed it, by the same means a man could raise himself by pulling on his boot-straps.

— Angus Sinclair, *Locomotive engine running and management*, 1887

2 | THE STEAM INJECTOR

A steam injector uses high-pressure steam to draw in and increase the pressure of low-pressure, liquid suction water. It does not require electric power for operation and can be used in passive emergency core cooling systems of light water reactors. Due to the complexity of the occurring flow phenomena, various experimental and numerical studies have been performed to assess the applicability in nuclear power plants. However, additional work is required to develop physically-based simulation models suitable for system studies.

Injectors are devices to pump liquids by transferring energy from a vaporous motive fluid, which is expanded and subsequently mixed with the fluid to be pumped. If steam serves as motive fluid, the term *steam injector* is commonly used. The steam injector was invented by Henri Giffard in 1858 and originally used for feed water supply in steam locomotives (Kneass, 1910).

Injectors and similar types of jet pumps, such as ejectors, allow for efficient, direct contact heat exchange and mixing and are therefore used in various technical applications, such as refrigeration and air conditioning, desalination, and in the petrochemical and chemical industry (Trela et al., 2010).

2.1 PRINCIPLE OF A STEAM INJECTOR

A steam injector (fig. 2.1) uses high-pressure steam (normally either saturated or slightly superheated) to draw in and increase the pressure of low-pressure, liquid suction water. To this end, the steam is first accelerated in a *convergent-divergent nozzle* in order to obtain a static outlet pressure which is below the pressure of the suction water. The nozzle discharges into a tapered *mixing chamber*, where the suction water is taken in through a coaxial, annular conduit. Here, the high-velocity, low-pressure steam entrains and condenses upon the low-velocity liquid water, thus causing a mass, momentum and energy transfer from the vapor to the liquid phase. Ideally, most of the condensation takes place almost instantaneously in the vicinity of the mixing chamber throat. This phenomenon, commonly referred to as *condensation shock*, causes a rapid pressure rise. Finally, the now single-phase liquid is decelerated in a *diffuser*, thus causing a further increase of the static pressure.

(a) Axial profile of the central steam nozzle type

(b) Static pressure from the steam nozzle entry to the diffuser exit
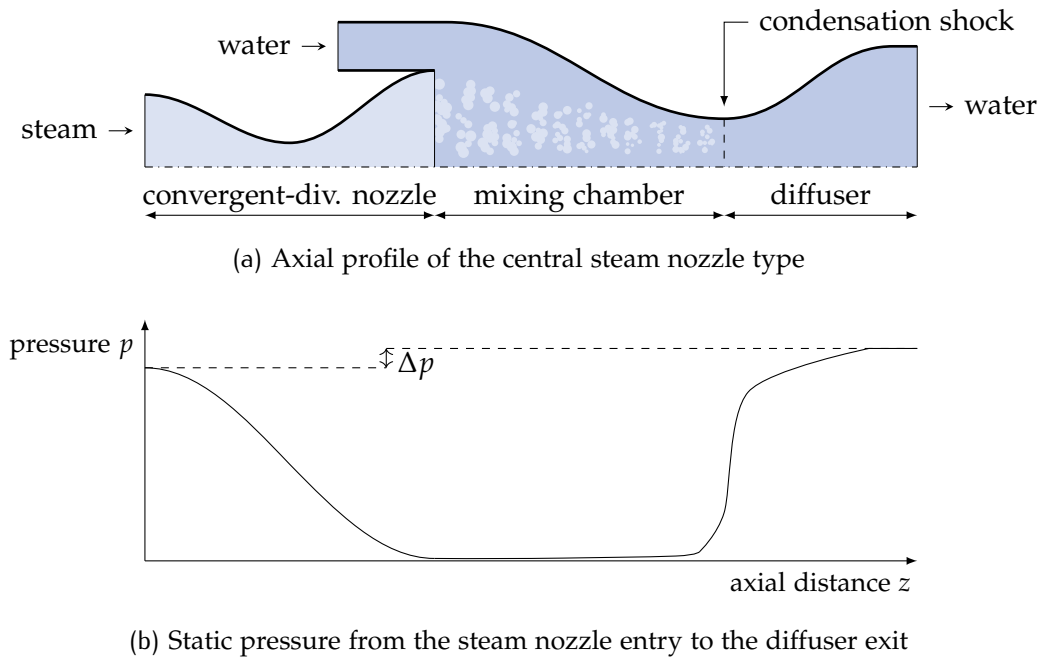
Figure 2.1: Schematic of a steam injector

An *overflow valve* in the vicinity of the mixing chamber throat (not shown in fig. 2.1) is usually included for start-up of the injector, which creates a suction pressure by draining the mixing chamber. The overflow valve is of particular importance when starting up against a high back pressure (Cattadori et al., 1995) or for low water suction pressures (Narabayashi et al., 2000).

The geometrical layout described above is known as *central steam jet* configuration. This injector type is recommended to achieve high discharge pressures (Ohmori et al., 2005) and can be operated if the suction pressure of the inlet water is low (Narabayashi et al., 2000). The layout reduces viscous dissipation, because there is no contact between the high-velocity steam and the mixing chamber walls (Cattadori et al., 1995; Yan et al., 2011). It is easier to design and therefore used more widely in the industry (Yan et al., 2011).

In contrast, the *central water jet* configuration uses an inversed inlet layout, i. e. a central water jet surrounded by an annular steam flow. This type requires higher water inlet pressures (Narabayashi et al., 2000) and is recommended for low-pressure injection (Ohmori et al., 2005).

Due to its applicability at high discharge pressures, the present work focuses on the central steam jet configuration.

2.2 APPLICATION FOR EMERGENCY CORE COOLING IN LIGHT WATER REACTORS

Being a compact, electricity-independent pumping system without rotating parts, the injector fulfills important requirements for a passive emergency core cooling system and has therefore been studied with respect to its applicability in a light water reactor for several decades. The main research focus was on attainable discharge pressures, operating behavior, operation stability, start-up and the development of system configurations.

2.2.1 Attainable discharge pressures

Independent experiments have shown that steam injectors can obtain discharge pressures that exceed the pressure of the motive steam. For instance, Cattadori et al. (1995) achieved outlet pressures of 80 bar using a steam inlet pressure of 70 bar and a water inlet pressure of 4 bar, Deberne et al. (1999) used steam at a pressure of 10 bar to increase the water pressure from 1.3 bar to 14 bar. In principle, the device is therefore capable of using the steam produced by the reactor decay heat to pump water into the core of a boiling water reactor or into the steam generator of a pressurized water reactor (table 2.1 and fig. 2.2).

However, a pressure gain could not be obtained in all experiments. Dumaz et al. (2005) could only achieve a small pressure increase within a limited range of boundary conditions, although their experiments were based on the successfully tested configuration of Cattadori et al. (1995). Zhang et al. (2011) reported unstable operation throughout their entire experiments which was attributed to the employed injector geometry.

Independent of the specific experimental conditions, two main criteria were identified by several authors that strongly influence the attainable discharge pressure:

- Increasing the *temperature of the suction water* leads to a rapid decrease of the discharge pressure. Deberne et al. (1999) found that the maximum discharge pressure decreased from 14 bar to 8 bar when increasing the water inlet temperature from 13 °C to 43 °C. Similar findings were reported by Cattadori et al. (1995), Yan et al. (2011), and Zhang et al. (2011).

- The *injector geometry*, in particular the steam/water cross-section ratio at the mixing chamber inlet (Yan et al., 2011) and the mixing chamber layout (Abe et al., 2006; Deberne et al., 1999; Shah et al., 2014; Yan et al., 2011), has to be precisely adapted to the fluid-dynamic boundary conditions.

	PRESSURE			PRESSURE RATIO	
	steam inlet	water inlet	dis-charge		
	$\dfrac{p_{s,in}}{\text{bar}}$	$\dfrac{p_{w,in}}{\text{bar}}$	$\dfrac{p_{out}}{\text{bar}}$	$\dfrac{p_{out}}{p_{w,in}}$	$\dfrac{p_{out}}{p_{s,in}}$
Cattadori et al. (1995)	87	2	98	49	1.1
Narabayashi et al. (1997)	55	16	90	5.6	1.6
Narabayashi et al. (2000)	70	4	75	19	1.1
Deberne et al. (1999)	10	1.3	14	11	1.4
Yan et al. (2011)	5	1.5	7	4.7	1.4
Zhang et al. (2011)	3.5		5		1.4
Deberne et al. (2000)	6.1	2.1	3.6	1.7	0.59

Table 2.1: Experimentally measured steam injector discharge pressures p_{out} and pressure ratios for different steam and water inlet pressures $p_{s,in}$ and $p_{w,in}$
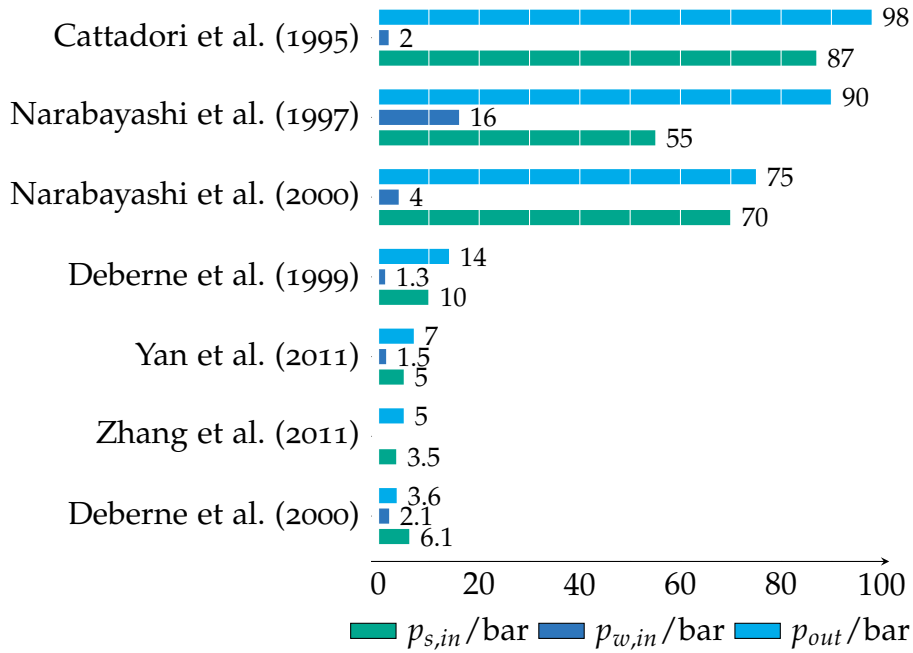
Figure 2.2: Experimentally measured steam injector discharge pressures p_{out} for different steam and water inlet pressures $p_{s,in}$ and $p_{w,in}$

Cattadori et al. (1995) point out that low water-steam mass flow ratios promote high discharge pressures, provided that the water flow rate is sufficient for complete condensation. According to Yan et al. (2011), the ratio between discharge and motive pressure increases with decreasing steam inlet pressure or increasing water inlet pressure.

2.2.2 Operating behavior

A stable and self-controlled injector operation over a large pressure range is possible if above criteria regarding fluid-dynamic boundary conditions and injector geometry are fulfilled (Deberne et al., 2000; Dumaz et al., 2005; Soplenkov et al., 1995; Yan et al., 2011). However, experimental studies have consistently shown a sharp performance limit at high discharge pressures. No stable operation could be achieved above this threshold (Abe et al., 2006; Deberne et al., 2000; Dumaz et al., 2005; Yan et al., 2011). Dumaz et al. observed that the condensation shock moves upstream with rising discharge pressure and suggested that the threshold was reached as soon as the shock entered the mixing chamber.

In the steam nozzle, irreversible losses due to friction, spontaneous condensation (chapter 3) and shock waves at the nozzle exit (chapter 4) deteriorate the performance (Trela et al., 2010). Moreover, incomplete condensation in the mixing chamber (chapter 5) results in a decrease of the discharge pressure (Deberne et al., 2000). Similarly, the presence of non-condensable gases inhibits the condensation efficiency, which decreases the attainable discharge pressures and may lead to unstable operating behavior (Abe et al., 2006; Iwaki et al., 2005).

2.2.3 System developments

Previously proposed steam injector systems for emergency core cooling can be broadly classified by two categories (fig. 2.3):

- The *recirculation configuration* is based on a closed circuit, where a part of the pumped water is being cooled down in a heat exchanger and fed back into the steam injector. High absolute discharge pressures can be attained in this way, as the injector only has to overcome the pressure losses in the circuit.

- The *injection configuration* uses an open circuit to inject directly from an external water reservoir. The attainable discharge pressures depend on the pressure of the water supply and are generally lower than in recirculation configurations. However, the temperature of the suction water can be kept low for a longer time by suitable design of the water reservoir, thus ensuring stable operation.

Howard (1984) proposed a multistage injection configuration with two injectors in serial connection and the additional use of a water-jet pump to achieve higher discharge pressure. Check valves were used to minimize manual operations during start-up.

Similarly, the injection configuration of Narabayashi et al. (1993) used serially connected injectors to increase the discharge pressure. Additionally, a parallel arrangement of multiple injectors was suggested to allow automatic start-up of a failed injector by using the suction force of the parallel injectors still in operation. Oscillations created by the serial connection were dampened by an accumulator to avoid unsteady operation.

Mazzocchi and Galbiati (1994) developed an injection configuration where the injector was placed 10 m below the water reservoir to make use of its static pressure head. The system included a hydraulic control mechanism for the overflow (start-up) valve.

(a) Recirculation configuration   (b) Injection configuration
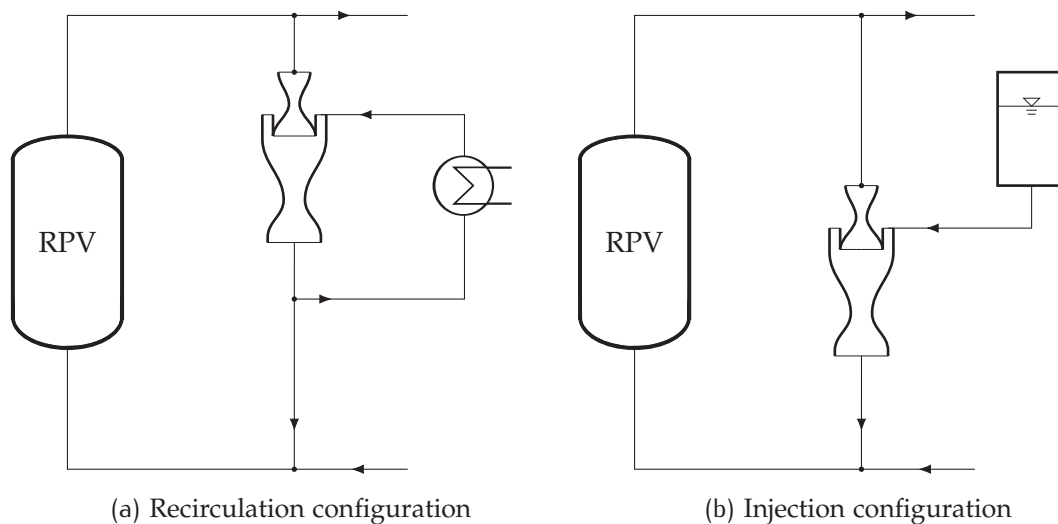
Figure 2.3: General concepts for the application of a steam injector for emergency core cooling in light water reactors. The water can be either directly injected into the *reactor pressure vessel* (RPV) of boiling water reactors, or into the steam generator of pressurized water reactors.

The opposite approach was used in the recirculation configuration by Reinsch (1995), Reinsch et al. (1995), and Soplenkov et al. (1995), where the injector was placed above the reactor pressure vessel to allow for passive, gravity-driven start-up. The authors point out that the supersonic flow in the steam nozzle prevented feedback within the coolant loop, thus allowing for stable operation.

Gautier and Aujollet (1999) combined both the injection and the recirculation configuration, thereby enabling high-pressure injection even at low suction pressures. Water from a pressurized tank was used for start-up, while a portion of the discharge water of the steam injector was recirculated and used in a water-jet pump to suck in water at lower pressures during steady operation.

Dumaz et al. (2005) and Dumaz and Duc (2003) suggested an injection configuration based on an injector with a needle-shaped drain positioned at the injector axis downstream from the mixing chamber. This drain was used instead of an overflow valve to remove excess steam which had not condensed in the mixing chamber, thus increasing the attainable discharge pressure and broadening the application range of the system. The injector was placed 2 m to 5 m below a water reservoir to make use of the static pressure head.

The research group around Narabayashi et al. (1997, 2000), Ohmori et al. (2006), and Ohmori et al. (2005) conducted extensive studies for the applicability of steam injectors in light water reactors. Among others, their results include several concepts for passive emergency core and containment cooling based on injection configurations. They used injectors with a central steam jet at high pressures and injectors with a central water jet at low pressures, thus covering a combined operation range from 1 bar to 80 bar.

2.3 MODELING APPROACHES — STATE OF THE ART

Various numerical studies of steam injectors have been conducted in the past. The approaches can be broadly divided into *global* models, which consider only the inlet and outlet states, and *local* models, which attempt to reproduce the flow structure within the injector.

Anand (1993) developed one-dimensional local models for the different phenomena encountered in central water type steam injectors. Expansion in the steam nozzle was based on compressible gas dynamic equations, allowing for non-equilibrium condensation under assumption of an initial droplet size. In the mixing chamber, condensation of steam on the liquid jet was assumed to be

steam-side limited and solved based on the kinetic gas theory. Cavitational breakup in consequence of turbulent pressure fluctuations was considered as the cause of jet atomization. The condensation shock was presumed to be due to steam bubble cavitation and simulated based on the Rayleigh–Plesset equation in combination with a mass transfer model according to the kinetic gas theory. The trends obtained by these model approaches were reported to be in agreement with literature data, but no complete model validation was possible due to limited experimental data.

Narabayashi et al. (1997) presented a two-dimensional CFD model for central water type injectors based on the separate two-phase flow model of the PHOENICS code. The heat transfer coefficient of condensation at the jet interface in the mixing chamber was calculated according to the kinetic gas theory in combination with the Clausius–Clapeyron equation. Good agreement with experimental data was reported.

Deberne et al. (1999) used a global control volume method which required an empirical correlation to determine the pressure rise in the mixing chamber of a central-water type injector. The condensation shock was assumed to be at the mixing chamber throat and to result in complete steam condensation. This approach was able to predict the influence of geometrical and physical parameters with an accuracy of 15 %.

Beithou and Aybar (2001a,b) proposed a one-dimensional local model for central steam type injectors. Single-phase, frictionless flow was assumed in the steam nozzle. The two-phase flow in the mixing chamber was solved under the assumptions of constant pressure and of thermal equilibrium at the mixing chamber throat. An empirical heat transfer correlation for direct contact condensation of steam jets in stagnant water (Chun and Y.-S. Kim, 1996) was employed. The simulation results for the pressure distribution were compared with the experiments by Cattadori et al. (1995) and good qualitative agreement was reported.

Dumaz et al. (2005) developed a one-dimensional local model to be integrated in the CATHARE2 system code. Empirical correlations derived from experimental data were used for the interfacial heat flux and the interfacial friction factor in the mixing chamber. Their model was able to predict the discharge pressure of a central steam type injector within 10 % of accuracy.

Shah (2012) and Shah et al. (2011, 2013) presented a CFD model for central steam type injectors which was implemented in Fluent 6.3. Expansion in the steam nozzle was calculated assuming one-dimensional, isentropic, single-phase flow. A

three-dimensional Eulerian two-phase flow model in conjunction with the realizable k-ϵ turbulence model was used for the mixing chamber. Here, bubbly flow was assumed, and the bubble diameter was taken as a linear function of local liquid subcooling using a correlation originally developed for condensation in rod bundles (Anglart and Nylund, 1996). The liquid-side heat transfer coefficient was determined according to Hughmark (1967) while a constant value was used for the gas-side, following Brucker and Sparrow (1977). The simulation results of static pressure and temperature matched closely with experimental data.

Neither of these approaches fulfills all requirements on a steam injector system study: The one-dimensional models are based on empirical correlations and thus lack universal validity, while the CFD models are too computationally intensive for system studies. The following chapters are devoted to bridging this gap by developing a physically-based, one-dimensional simulation model without application-specific empirical correction factors.

2.4 GENERAL MODELING ASSUMPTIONS

Typical steam injectors have a rotation-symmetric geometry and a fairly smooth development of the flow cross-section. This allows to assume a one-dimensional flow field, i.e. to consider only changes of flow properties in the axial direction (coordinate z). Accordingly, the thermo-fluiddynamics of the two-phase flow in a steam injector are described by a one-dimensional model throughout this work. Additionally, the flow is taken to be stationary, since no transient phenomena such as start-up or unstable operation are to be studied. Moreover, gravitational forces can be neglected with regard to the high momentum of the flow, and heat conduction is negligible in comparison to the occurring turbulent heat transfer processes.

In one-dimensional models, local flow properties x_i must be replaced by area-averaged quantities $\langle x_i \rangle$. Ishii and Mishima (1984) show that the product of average quantities is not necessarily equal to the average of the product, i.e. $\prod \langle x_i \rangle \neq \langle \prod x_i \rangle$. They account for this so-called *covariance effect* by introducing distribution parameters for various regimes (bubbly, plug, annular, droplet, etc.) of fully developed pipe flow. The flow in a steam injector, however, is far from fully developed and this concept cannot be applied here. Therefore, the distribution parameters are assumed to be equal to unity (i.e. $\prod \langle x_i \rangle = \langle \prod x_i \rangle$). For simplification, the area-averaging notation $\langle \rangle$ will be omitted subsequently, as all quantities will be considered to be area-averaged.

At [...] 200 pounds per square inch steam passes into the atmosphere with a velocity of 1960 feet per second. When steam at this speed strikes like a lightning-flash into the tubes of the injector, it becomes the ram which forces the water towards the boiler [...].

— Angus Sinclair, *Locomotive engine running and management*, 1887

3 | SPONTANEOUS CONDENSATION IN THE STEAM NOZZLE

A one-dimensional modeling approach is presented for the steam expansion in convergent–divergent nozzles. Main objective is a generic model that accurately predicts the pressure at the primary nozzle exit plane of a steam injector while keeping a high simulation speed. The approach uses the classical nucleation theory in order to account for the non–equilibrium phenomenon of spontaneous condensation caused by homogeneous nucleation of the supersaturated steam. The modifications by Courtney and Kantrowitz/Feder are included in order to account for the partial pressure of the nucleation clusters and non–isothermal effects during nucleation, thus allowing an accurate prediction of the nucleation rate over a wide pressure range. Droplet growth is modeled using a theory developed by Peters and Meyer which takes into account effects in both the molecular and the continuum regime. The resulting two–phase flow equations constitute a system of ordinary differential equations which is discretized by means of the Euler method. The model is validated using published data of steam nozzle experiments.

The steam injector can be divided into three major sections, as sketched in fig. 2.1: the steam nozzle, the mixing chamber and the diffuser. In the convergent-divergent steam nozzle, the high-pressure steam expands to a low static outlet pressure and reaches supersonic velocities. This expansion process is examined in the following.

Current steam expansion simulation efforts focus on two- or three-dimensional approaches to model complex flow structures, particularly in the low-pressure stages of steam turbines (e. g. Gerber and Kermani, 2004; Sigg, 2010; Starzmann et al., 2012). They are normally based on existing CFD-codes and are therefore not within the scope of the present work.

In most cases, one-dimensional flow models are sufficient to yield good results for simple geometries such as convergent-divergent nozzles. However, existing one-dimensional models are mostly based on out-dated equations of state or are only valid at low pressures (e. g. Hedbäck, 1982; Ludwig, 1975; Treffinger, 1994).

For these reasons, the objective of this chapter is the development of an efficient simulation model for the steam expansion in convergent-divergent nozzles which does not rely on application-specific correction factors. The model has to take into account the real-gas behavior of steam at high pressures and has to be capable of reproducing two major physical phenomena: The nucleation, i. e. the

creation of stable liquid clusters from the gas phase, and the subsequent growth of these clusters.

3.1 FUNDAMENTALS

3.1.1 Supersaturation and spontaneous condensation

The expansion of saturated or slightly superheated vapor differs from the expansion of a dry gas due to the proximity to the saturation state. This results in a phenomenon known as *spontaneous condensation* and leads to a two-phase flow of small liquid droplets in a continuous gas phase towards the end of the nozzle.

Upon entering the nozzle, the high expansion rate causes the vapor to cool to temperatures below the saturation line without measurable condensation. Defining the *saturation ratio S* as the ratio of vapor pressure p_g [Pa] to the saturation pressure p_{sat} at the vapor temperature T_g [K],

$$S = \frac{p_g}{p_{sat}\left(T_g\right)} \quad , \tag{3.1}$$

the saturation state is then reached at $S = 1$, whereas *supersaturated*, i.e. metastable states are characterized by $S > 1$.

A maximum saturation ratio will be reached at a certain point in the nozzle, whose location depends on the stagnation condition of the steam. At this point, generally referred to as *Wilson point*, measurable condensation can be detected in the flow, resulting in the formation of small liquid droplets. The initial dimension of these droplets is normally in the range of only a few micro- or even nanometers.

The latent heat release during condensation causes a static pressure and temperature rise as well as a deceleration of the flow. The saturation ratio decreases until a state close to the thermodynamic equilibrium, i.e. $S = 1$ is reached.

3.1.2 Classical nucleation theory

Nucleation, i.e. the formation of stable liquid clusters from a gas phase, can in general occur in two ways: *Homogeneous nucleation*, where clusters are spontaneously formed due to density and energy fluctuations in the vapor, and *heterogeneous nucleation*, where condensation takes place on foreign particles. Gerber and

Kermani (2004) point out that heterogeneous nucleation may occur during rapid steam expansion, but only the large number of very small droplets created by homogeneous nucleation is capable of providing the droplet surface area required to revert the flow to equilibrium. This is supported by the experiments of Dibelius et al. (1983) which have shown that heterogeneous nucleation in steam turbine flows is negligible for foreign particle concentrations of less than $10^8/\text{cm}^3$. For this reason, only homogeneous nucleation is considered in the following.

The prevailing model of homogeneous nucleation is the classical nucleation theory, which determines the nucleation rate based on Boltzmann statistics and has been mainly developed by Volmer and Weber (1926) as well as R. Becker and Döring (1935). A short overview is presented in the following, while a more exhaustive summary is given by Bakhtar et al. (2005).

The formation of a single spherical droplet of radius r from a supersaturated vapor at constant pressure p_g and temperature T_g results in a change of Gibbs free energy

$$\Delta G = 4\pi r^2 \sigma - \frac{4}{3}\pi \frac{r^3}{v_l}\Delta g_S \quad , \tag{3.2}$$

where σ is the surface tension [kg/s^2], v_l the specific volume [m^3/kg] of the liquid, and Δg_S the supersaturation term

$$\Delta g_S = g\left(T_g, p_g\right) - g\left(T_g, p_{sat}\left(T_g\right)\right) - v_l \cdot \left[p_g - p_{sat}\left(T_g\right)\right] \quad , \tag{3.3}$$

with $g(T_g, p_g)$ and $g(T_g, p_{sat}(T_g))$ being the specific Gibbs free energy [J/kg] at vapor temperature and pressure or at vapor temperature and saturation pressure, respectively.

In eq. (3.2), the first term describes the creation of the cluster surface and is always positive, while the second term describes the phase change and is negative for $S > 1$ (fig. 3.1). The maximum value of ΔG can be found by derivation of eq. (3.2) by r, which leads to the critical radius r^* and the critical Gibbs free energy change ΔG^*:

$$r^* = 2\frac{\sigma v_l}{\Delta g_S} \tag{3.4}$$

$$\Delta G^* = \frac{16}{3}\pi\sigma^3 \left(\frac{v_l}{\Delta g_S}\right)^2 \tag{3.5}$$

Clusters above this critical radius are stable nuclei that will start growing and thereby initiate the condensation process.
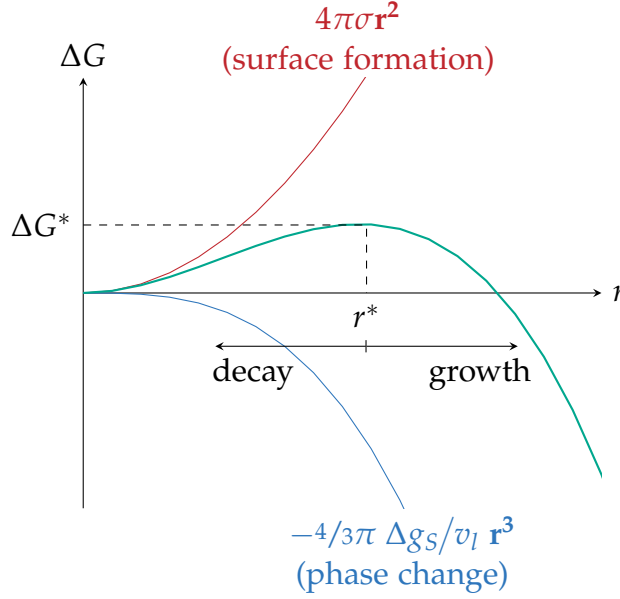
Figure 3.1: Change of Gibbs free energy ΔG (——) during formation of a liquid nucleus with radius r in a supersaturated environment as a sum of the energy increase due to surface formation (——) and the decrease due to phase change (——). Clusters above the critical radius r^* are stable and will start growing.

According to the classical theory (indicated by the index *CL*), the *mass-specific nucleation rate* of critical clusters J [1/(kg s)] can be determined by the following expression (Bakhtar et al., 2005; Ehrler and Schaber, 2006):

$$J_{CL} = C_{co} \cdot \frac{v_l}{v_g} \sqrt{\frac{2\sigma}{\pi m_{\odot}^3}} \cdot \exp\left(-\frac{\Delta G^*}{k_B T_v}\right) \quad . \tag{3.6}$$

Here, v_g is the specific vapor volume, $m_{\odot}$ the mass of a molecule [kg], k_B the Boltzmann constant and $C_{co} \leq 1$ is the *condensation coefficient*.

The radius of critical clusters is normally in the range of few micro- or even nanometers. Nevertheless, the classical nucleation theory is based on macroscopic properties such as specific volume and surface tension, which are not properly defined at these microscopic scales. Particular debate has arisen over the surface tension, which appears in the exponential term of eq. (3.6) to the third power and thus has a considerable effect on the nucleation rate. Several corrections for the surface tension of microscopic droplets have been proposed, but yield contradicting results, as discussed by Bakhtar et al. (2005).

Various refinements and corrections to the classical nucleation theory have been proposed since its development. Upon comparing the major augmentations, Bakhtar et al. (2005) concluded that the correction terms derived by Courtney

(1961) and Kantrowitz (1951) are most suitable to achieve good agreement with experimental data over a wide pressure range, when used in combination with a condensation coefficient of $C_{co} = 1$ and no correction for the surface tension. Courtney's correction term accounts for partial pressure effects, while the correction term developed by Kantrowitz and refined by Feder et al. (1966) accounts for non-isothermal effects during nucleation. Using these correction terms leads to the corrected nucleation rate

$$J = \frac{v_g}{v_{g,sat}\left(T_g\right)} \cdot \Theta \cdot J_{CL} \quad , \tag{3.7}$$

where $v_{g,sat}\left(T_g\right)$ is the specific vapor volume at saturation and Θ the *non-isothermal factor*

$$\Theta = \frac{\left(c_{v,g} + \frac{k_B}{2m_\odot}\right) k_B T_g^2}{\left(c_{v,g} + \frac{k_B}{2m_\odot}\right) k_B T_g^2 + m_\odot \left[T_g \cdot \left(s_g - s_l\right) - \frac{k_B T_g}{2m_\odot} - \frac{2\sigma v_l}{r^{*2}}\right]^2} \quad , \tag{3.8}$$

with $c_{v,g}$ being the specific isochoric heat capacity [J/(kg K)] of the vapor and s_g and s_l the specific entropy [J/(kg K)] of vapor and liquid, respectively.

3.1.3 Thermodynamics of nanodroplets

The definition or derivation of thermodynamic variables and relationships by means of continuum mechanics assumes local equilibrium in the considered system. This assumption is fulfilled if there is a sufficient number of particle interactions in a sufficiently small control volume. For an ideal gas at standard conditions, a cube with an edge length of 1 μm contains approximately 2.7×10^7 molecules and therefore represents a suitable control volume.

The radius of critical clusters created by homogeneous nucleation may be as small as a few nanometers and is thus normally below the validity limit of macroscopic continuum mechanics. Therefore, a universally valid droplet growth model has to consider both transport processes in the molecular and the continuum regime.

For this reason, a *collision free zone* is defined around the droplet, having a thickness of the order of the mean free path of gas molecules $\bar{l}$ [m]. Evaporating molecules from the droplet and incoming vapor molecules are assumed to pass this area without collision, and exchange processes in this region are determined

using the kinetic theory of gases. This region is normally referred to as *Knudsen layer* with the corresponding outer radius r_{Kn}, as depicted in fig. 3.2.

Based on this assumption, Peters and Meyer (1995) have developed and experimentally validated a droplet growth model of pure vapor which will be used in the following. Main aspects of the theory are the calculation of the temperature of a water droplet in a pure vapor atmosphere and the evaluation of the mass and heat flow rates that result from a deviation of the thermodynamic equilibrium between gas and vapor phase (i.e. condensation or evaporation).

Calculation of the droplet temperature

As discussed by Peters and Meyer, the pressure gradient in the continuum region can be neglected as a driving potential for condensation or evaporation with respect to the influence of the temperature gradient. Hence, the pressure at the outer boundary of the Knudsen layer is assumed equal to the vapor pressure ($p_{Kn} = p_g$).

According to the kinetic theory of gases, pressure changes are caused by momentum exchange between particles. Consequently, there is no pressure difference in the Knudsen layer since it is assumed to be collision-free.

Peters and Meyer show that the deviation of the pressure at the droplet surface $p_{drp,if}$ from the equilibrium vapor pressure of small droplets $p_{sat,r}$ is negligible and thus assume $p_{drp,if} = p_{sat,r}$. The equilibrium vapor pressure of small droplets
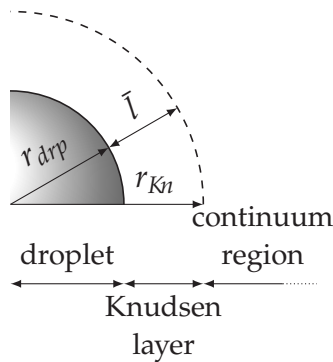
Figure 3.2: Definition of the collision-free Knudsen layer with outer radius r_{Kn} around a liquid droplet with radius r_{drp}. The thickness of the Knudsen layer is assumed equal to the mean free path $\bar{l}$.

can be determined as a function of the droplet radius r_{drp} and temperature T_{drp} using Kelvin's equation[1]:

$$p_{sat,r}\left(T_{drp}, r_{drp}\right) = p_{sat}\left(T_{drp}\right) \cdot \exp\left(\frac{2\sigma v_l}{r_{drp} R_s T_{drp}}\right) \tag{3.9}$$

Here, p_{sat} is the equilibrium vapor pressure for a flat surface and R_s is the specific gas constant [J/(kg K)] of the vapor.

Assuming that ambient pressure, the pressure at the Knudsen boundary and surface pressure are equal ($p_g = p_{Kn} = p_{drp,if} = p_{sat,r}$), T_{drp} can be determined iteratively from eq. (3.9) for a given vapor pressure and droplet radius.

Calculation of the mass and heat flow rate

From a microscopic viewpoint, thermodynamic equilibrium between a liquid and a vapor phase exists if the number of molecules entering the liquid phase is equal to the number of molecules leaving. Net condensation or evaporation occurs as soon as the droplet state deviates from the equilibrium state, i. e. if the droplet temperature T_{drp} and/or surface pressure $p_{drp,if}$ differ from their saturation values.

The heat flow rate $\dot{Q}$ [J/s] is taken to be constant in the continuum region and it is assumed that the latent heat of condensation Δh_{lg} [J/kg] is completely released to the vapor:

$$\dot{Q} = -\dot{M} \cdot \Delta h_{lg} \tag{3.10}$$

This allows determining the mass flow rate $\dot{M}$ [kg/s] in the continuum region ($r \geq r_{Kn}$),

$$\dot{M} = 4\pi \frac{\lambda}{\Delta h_{lg}\left(T_{drp}\right)} r_{Kn} \cdot \left(T_{Kn} - T_g\right) \quad, \tag{3.11}$$

where λ is the thermal conductivity [W/(m K)] of the vapor, $\Delta h_{lg}\left(T_{drp}\right)$ is the latent heat of condensation at the droplet temperature T_{drp}, T_{Kn} is the (yet unknown) temperature at the Knudsen boundary and T_g the ambient vapor temperature for $r \to \infty$. Positive values of $\dot{M}$ indicate condensation.

---

1   derivation in appendix A.2.2

Allowing only small deviations from equilibrium, Peters and Meyer derive an additional equation for the mass flow rate in the collision free zone ($r_{drp} \leq r \leq r_{Kn}$) based on the kinetic theory of gases:

$$\dot{M} = -4\pi r_d^2 \frac{\dfrac{p_{drp,if}}{\sqrt{2\pi R_s T_{drp}}} - \dfrac{p_{Kn}}{\sqrt{2\pi R_s T_{Kn}}}}{1 - \frac{1}{2}\left(\dfrac{r_{drp}}{r_{Kn}}\right)^2} \tag{3.12}$$

Assuming $r_{Kn} = r_{drp} + \bar{l}$, eqs. (3.11) and (3.12) provide two equations for the two remaining unknown variables T_{Kn} and $\dot{M}$. Based on the kinetic theory, the mean free path is calculated as

$$\bar{l} = \frac{k_B T_{Kn}}{\sqrt{2}\pi d_\odot^2 p_g}\ , \tag{3.13}$$

where $d_\odot$ is the molecular diameter.

The numerator of eq. (3.12) describes the difference of molecular impingement rates, where the first term accounts for molecules leaving the droplet (evaporation), and the second term for molecules entering the collision-free zone and hitting the droplet (condensation). Upon comparing their model to experimental data, Peters and Meyer concluded that either the condensation or evaporation term had to be corrected by 1 % to achieve agreement with the experiments.

Similar to common formulas such as the Hertz-Knudsen-Langmuir or the Schrage equation, eq. (3.12) allows to determine the mass flow rate in the Knudsen layer without solving the Boltzmann equation. However, as discussed by Fujikawa et al. (2011), this simplification may yield incorrect solutions. In particular, the mass flow rate does not only vanish under equilibrium conditions ($p_{Kn} = p_{drp,if}$, $T_{Kn} = T_{drp}$), but for all values that satisfy the relation $T_{Kn}/T_{drp} = (p_{Kn}/p_{drp,if})^2$. Furthermore, the correction of the condensation or evaporation term as applied by Peters and Meyer (1995) prevents the mass flow rate from approaching zero even when equilibrium conditions are reached. Accordingly, while being convenient to improve the model accuracy, the approach is not suitable when approaching equilibrium conditions. Nevertheless, good agreement with experimental data justifies the use of such simplifications for practical considerations.

3.2 THEORETICAL MODEL

3.2.1 Two–phase droplet flow

J. Young (1995) provides a general system of conservation equations for the multiphase flow consisting of a continuous gas phase and a discontinuous liquid phase of small dispersed water droplets. Owing to the small volume fraction of droplets, droplets are assumed to be homogeneous and droplet interactions are neglected. Additionally, viscosity, heat conduction and diffusion in the gas phase are neglected, except for interfacial exchange processes. The model is based on a distribution of the continuous droplet spectrum into k discrete droplet groups, each consisting of a number of droplets with equal radii.

The liquid mass fraction x_l can then be obtained using the mass-specific droplet number n_i [1/kg] of a droplet group and the mass of a single droplet $m_{drp,i}$,

$$x_l = \sum_{i=1}^{k} x_i = \sum_{i=1}^{k} n_i m_{drp,i} \,, \tag{3.14}$$

which can be used to define a mixture density ρ_m [kg/m^3]

$$\frac{1}{\rho_m} = \frac{1 - x_l}{\rho_g} + \sum_{i=1}^{k} \frac{x_i}{\rho_i} \,, \tag{3.15}$$

where ρ_g and ρ_i are the densities of the vapor and of the droplet group i, respectively.

In the following, a one-dimensional, stationary flow without the presence of inert gases (pure vapor) and without slip (equal velocity c [m/s] of the liquid and the gas phase) is assumed. This simplifies J. Young's equations to the following form:

$$c \frac{\mathrm{d}n_i}{\mathrm{d}z} = J_i \tag{3.16}$$

$$c \frac{\mathrm{d}x_i}{\mathrm{d}z} = n_i \dot{M}_i + m_{drp,i} J_i \tag{3.17}$$

$$\frac{1}{c} \frac{\mathrm{d}c}{\mathrm{d}z} + \frac{1}{\rho_m} \frac{\mathrm{d}\rho_m}{\mathrm{d}z} = 0 \tag{3.18}$$

$$c \frac{\mathrm{d}c}{\mathrm{d}z} + \frac{1}{\rho_m} \frac{\mathrm{d}p_g}{\mathrm{d}z} = 0 \tag{3.19}$$

$$(1 - x_l) c \left(\frac{\mathrm{d}h_g}{\mathrm{d}z} - \frac{1}{\rho_g} \frac{\mathrm{d}p_g}{\mathrm{d}z} \right) = \sum_{i=1}^{k} \left(m_{drp,i} J_i \Delta h_{lg,i} - n_i \dot{Q}_i \right) \tag{3.20}$$

Equations (3.16) and (3.17) are the droplet number and mass conservation for droplet group i, eqs. (3.18) and (3.19) are the mass and momentum conservation of the mixture, and eq. (3.20) is the energy conservation in the gas phase using the specific enthalpy h [J/kg].

The use of the integral form of the mixture mass conservation instead of eq. (3.18) allows to calculate the flow along the axis of a nozzle (axial coordinate z, flow cross section A [m²]):

$$\frac{1}{c}\frac{\mathrm{d}c}{\mathrm{d}z} + \frac{1}{\rho_m}\frac{\mathrm{d}\rho_m}{\mathrm{d}z} = -\frac{1}{A}\frac{\mathrm{d}A}{\mathrm{d}z} \tag{3.21}$$

3.2.2 Single–phase vapor flow

For superheated vapor or metastable vapor with negligible condensation, the nozzle flow is assumed to be isentropic. Using the sonic velocity of the vapor w, the density change can then be expressed as

$$\frac{\mathrm{d}\rho_g}{\mathrm{d}z} = \left.\frac{\partial\rho_g}{\partial p_g}\right|_s \frac{\mathrm{d}p_g}{\mathrm{d}z} = \frac{1}{w^2}\frac{\mathrm{d}p_g}{\mathrm{d}z} \quad, \tag{3.22}$$

allowing to express the single-phase flow conservation equations in the following well-known form:

$$\frac{\mathrm{d}c}{\mathrm{d}z} = -C_1 \tag{3.23}$$

$$\frac{\mathrm{d}p_g}{\mathrm{d}z} = c\rho_g\cdot C_1 \tag{3.24}$$

$$\frac{\mathrm{d}h_g}{\mathrm{d}z} = c\cdot C_1 \tag{3.25}$$

$$C_1 = \frac{\frac{c}{A}\frac{\mathrm{d}A}{\mathrm{d}z}}{1 - \frac{c^2}{w^2}} \tag{3.26}$$

3.3 SIMULATION MODEL

The conservation equations for the two-phase flow (eqs. (3.16), (3.17) and (3.19) to (3.21)) constitute a system of $3 + 2k$ *ordinary differential equations* (ODEs) for

$4 + 2k$ unknown derivatives ($\mathrm{d}c/\mathrm{d}z$, $\mathrm{d}\rho_m/\mathrm{d}z$, $\mathrm{d}p_v/\mathrm{d}z$, $\mathrm{d}h_v/\mathrm{d}z$, $\mathrm{d}n_i/\mathrm{d}z$ and $\mathrm{d}y_i/\mathrm{d}z$) and thus cannot be solved in this form.

The equation of state provides the necessary additional relationship that allows to eliminate $\mathrm{d}\rho_m/\mathrm{d}z$ from the ODE system. For this purpose, the mixture density, eq. (3.15), is derived by z while neglecting the change of liquid density ($\mathrm{d}\rho_i/\mathrm{d}z = 0$), leading to

$$-\frac{1}{\rho_m^2}\frac{\mathrm{d}\rho_m}{\mathrm{d}z} = \frac{\mathrm{d}v_m}{\mathrm{d}z} = (1 - x_l)\frac{\mathrm{d}v_g}{\mathrm{d}z} + \sum_{i=1}^{k}\left(v_i - v_g\right)\frac{\mathrm{d}x_i}{\mathrm{d}z} . \qquad (3.27)$$

The specific vapor volume can be represented as a function of pressure and enthalpy using the equation of state. Accordingly, $\mathrm{d}v_g/\mathrm{d}z$ can be omitted from eq. (3.27) using the total differential

$$\frac{\mathrm{d}v_g}{\mathrm{d}z} = \left.\frac{\partial v_g}{\partial p_g}\right|_{h_g}\frac{\mathrm{d}p_g}{\mathrm{d}z} + \left.\frac{\partial v_g}{\partial h_g}\right|_{p_g}\frac{\mathrm{d}h_g}{\mathrm{d}z} , \qquad (3.28)$$

where the partial derivatives can be determined from the equation of state.

The numerically convenient form of the conservation equations is given in appendix B.1, eqs. (B.1) to (B.5). The ODE system defined in this way is discretized and solved using the first-order Euler method. Runge-Kutta methods of higher order are not used due to the varying number of equations: Each solver step may result in the creation of a new droplet group, which adds two equations (droplet number and mass conservation) to the system.

3.3.1 Boundary conditions

The critical state at the nozzle throat is used as inlet boundary condition. Assuming single-phase flow at the nozzle throat, the vapor pressure and enthalpy at the throat are first estimated using the ideal gas equations and are then updated iteratively[2] until the conditions of isentropic and isenthalpic flow are fulfilled from the stagnation state to the nozzle throat.

Owing to the exponential nature of eq. (3.6), the nucleation rate starts at very small values and grows by several orders of magnitude before it has any effect on the nozzle flow. For this reason, a lower limit for the nucleation rate $J_{min} = 10^{20}/(\mathrm{kg}\,\mathrm{s})$ is defined and nucleation is neglected up to this limit.

---

2 multidimensional root finding algorithm for $n = 2$ variables according to appendix B.5

The single-phase flow eqs. (3.23) to (3.26) are used to model the nozzle flow up to the onset of spontaneous condensation in the divergent nozzle section. However, eq. (3.26) becomes singular at the nozzle throat ($z = z_{crit}$), where the flow velocity is equal to the sonic velocity and both numerator and denominator approach zero. Application of l'Hôpital's rule allows to transform eq. (3.26) in combination with eqs. (3.23) to (3.25), resulting in

$$C_{1,crit} = -\frac{\frac{c}{w^2}\frac{dw}{dz} \pm \sqrt{\left(\frac{c}{w^2}\frac{dw}{dz}\right)^2 + \frac{2}{A}\frac{d^2 A}{dz^2}}}{\frac{2}{w}} \; . \tag{3.29}$$

The physically correct solution of eq. (3.29) has to fulfill the condition for shock-free nozzle flows

$$\frac{dc}{dz} > 0 \quad \Leftrightarrow \quad C_{1,crit} = -\frac{dc}{dz} < 0 \; . \tag{3.30}$$

Equation (3.29) includes the initially unknown spatial derivation of the sonic velocity dw/dz. Therefore, the approximation

$$\left.\frac{dw}{dz}\right|_z \approx \frac{w(z + \Delta z) - w(z)}{\Delta z} \tag{3.31}$$

is being used in order to solve the first step from z_{crit} to $z_{crit} + \Delta z$: The solver step starts with an estimate for dw/dz and is iterated until eq. (3.31) is fulfilled sufficiently well.

3.3.2 Solution procedure

The single-phase flow equations derived in section 3.2.2 are used until the nucleation rate threshold J_{min} is reached for the first time and the two-phase flow solver is invoked. Subsequently, each solver step consists of the following major sub-steps:

1. The thermodynamic properties of the vapor at the axial coordinate z are determined according to the equation of state using the values of vapor pressure p_g and enthalpy h_g.

2. The thermodynamic state of each droplet group i at the axial coordinate z is determined iteratively[3]. Starting with the values of the previous step as first estimate, the droplet radius $r_{drp,i}$ and temperature $T_{drp,i}$ are used

---

3 multidimensional root finding algorithm for $n = 2$ variables according to appendix B.5

to calculate the internal pressure of the droplet according to the Young-Laplace equation[4]:

$$p_{drp,i} = p_g + \frac{2\sigma}{r_{drp,i}} \tag{3.32}$$

Next, the thermodynamic properties of the droplet are obtained using the values of droplet pressure $p_{drp,i}$ and temperature $T_{drp,i}$. With these values, the equilibrium vapor pressure $p_{sat,r,i}$ is calculated from eq. (3.9) and the droplet mass is calculated using $m_i = 4/3 \, \pi r_{drp,i}^3 \rho_i$. The values for $r_{drp,i}$ and $T_{drp,i}$ are updated until the following two conditions are fulfilled: $m_i = x_i/n_i$; $p_{sat,r,i} = p_g$.

3. Using the value of the previous step as first estimate, the interface temperature $T_{Kn,i}$ is iteratively updated[5] until the droplet mass flow rate $\dot{M}_i$ according to eqs. (3.11) and (3.12) yields the same result. The heat flow rate $\dot{Q}_i$ is then obtained from eq. (3.10).

4. The nucleation rate for the current vapor conditions is calculated using eq. (3.7) and a new droplet group is created if the nucleation rate is above the specified threshold J_{min}.

5. The derivatives dc/dz, dp_g/dz, dh_g/dz, dn_i/dz and dx_i/dz are calculated using eqs. (B.1) to (B.5), which are then used to determine the flow variables at the next step $z + \Delta z$ based on the Euler method.

The iterative calculation of the mass flow rate (step 3 in above-mentioned list) converges only when the initial estimate of the interface temperature $T_{Kn,i}$ is sufficiently close to the final solution. No convergence could be achieved when including the condensation/evaporation coefficient proposed by Peters and Meyer (1995) as described in section 3.1.3. For this reason, the mass flow rate is instead reduced by a fixed factor of 0.64, which is the average correction that would result from applying the condensation/evaporation coefficient suggested by Peters and Meyer. However, this approach overestimates the growth of small droplets and underestimates the growth of large ones.

The thermodynamic fluid properties are calculated using the IAPWS-IF97 equation of state (Wagner et al., 2000). The IAPWS-IF97 is valid for pressures up to 100 MPa and thus covers the extremely high internal pressures of very small droplets. Furthermore, it includes a formulation for metastable vapor that is valid from the saturated vapor line to the 5 % equilibrium moisture line. Additional details on thermodynamic property calculation are given in appendix A.1.

---

4 derivation in appendix A.2.1
5 multidimensional root finding algorithm for $n = 1$ variables according to appendix B.5

3.4 VALIDATION

Two experimental test series based on different nozzle geometries and stagnation conditions were selected for validation of the simulation model.

3.4.1 Low pressure experiments

The first series was conducted by Barschdorff (1971), who used steam with a constant stagnation pressure of $p_0 = 0.7839$ bar and a varying stagnation temperature between $T_0 = 93.8\,°C$ and $T_0 = 135.2\,°C$. As can been seen from fig. 3.3, the simulation is in good agreement with the experimental data, but precise quantitative accordance is not achieved: The axial position of the condensation-induced pressure rise is predicted very accurately, while the pressure rise itself is overestimated. Moreover, the calculated pressure prior to condensation is lower than the value obtained experimentally, and the experimental data indicate a faster pressure drop after the condensation zone than predicted by the model.
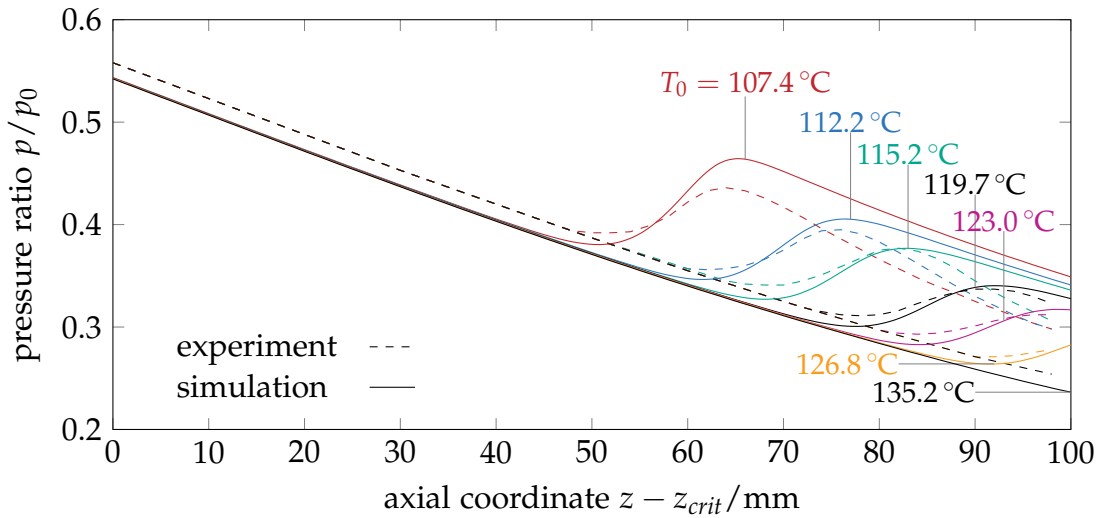
Figure 3.3: Simulation of experiments by Barschdorff (1971), showing the pressure ratio p/p_0 in the divergent nozzle section (axial position of the nozzle throat at $z = z_{crit}$, stagnation pressure $p_0 = 0.7839$ bar) for varying stagnation temperatures T_0.

Barschdorff conducted additional experiments with lower stagnation temperatures than the ones shown in fig. 3.3. This causes the Wilson point to move further upstream and finally leads to a normal shock as soon as the energy release is sufficient to decelerate the flow below the sonic velocity. The ODE system

derived in section 3.2 is not valid for flow discontinuities and cannot be applied in these cases which are therefore not shown here.

3.4.2 High pressure experiments

The second test series, conducted by Gyarmathy (2005), is based on considerably higher stagnation pressures up to over 100 bar and four different nozzle shapes. Figure 3.4a shows results for the nozzle geometry with designation 2/M for three different stagnation conditions. Again, good agreement between simulation and experiment is obtained with respect to the axial position of the pressure rise, while the simulation shows a steeper and higher pressure rise than the experimental data and the pressure before condensation is lower than in the experiment. The arithmetic mean droplet radius determined by the simulation is higher than the experimental value at early stages of condensation, whereas the opposite is true as soon as the flow approaches equilibrium conditions.

Simulation of nozzle 4/B (fig. 3.4b) yielded similar results, whereas simulation of nozzles 5/B and 6/B (appendix, fig. D.1) globally underestimates the droplet radius. In the last-mentioned nozzles, nucleation starts in the subsonic part of the nozzle, while the model assumes single-phase flow up to the throat.

3.4.3 Interpretation of results

The developed model is capable of accurately predicting the Wilson point, i. e. the axial position of the condensation-induced pressure rise, while precise quantitative accordance of the pressure rise itself is not achieved. It is believed that the main source of the pressure deviations is the droplet growth model. As described in section 3.3, the model approach overestimates the growth of small droplets, which can be confirmed when comparing the simulated and the measured mean droplet radius in fig. 3.4. Higher droplet growth rates in the early stages of condensation increase the energy release due to condensation and thus cause a faster pressure rise. Accordingly, additional research is required regarding (i) improvement of the numerical stability when including the condensation/evaporation coefficient proposed by Peters and Meyer and (ii) refinement of the droplet growth model itself to maintain its validity when approaching equilibrium conditions (cf. section 3.1.3).
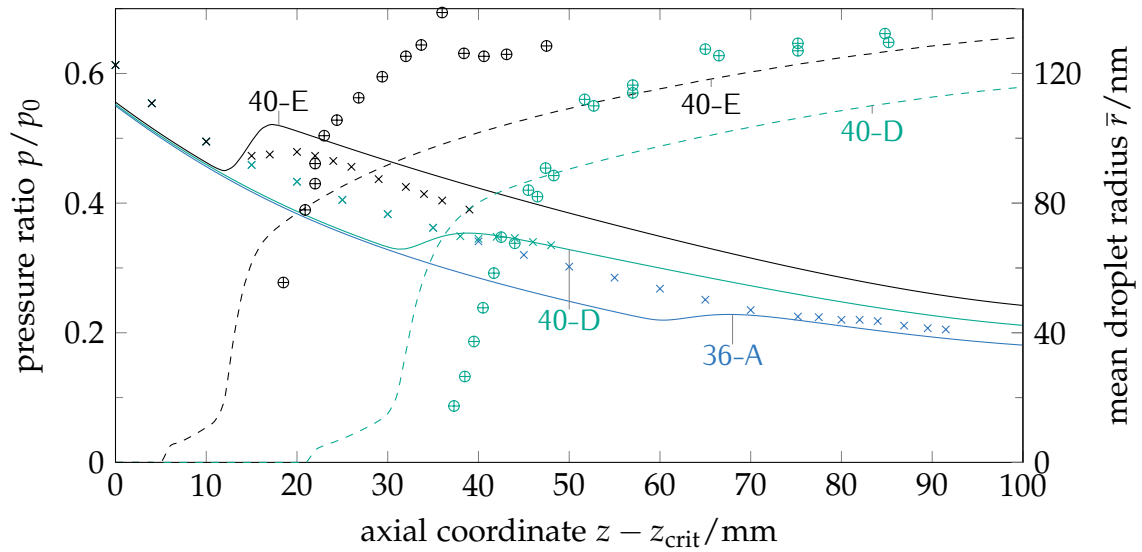
(a) Nozzle 2/M

test run designation	36-A	40-D	40-E
stagnation pressure p_0/bar	107	109	109
stagnation temperature T_0/°C	389	364	346
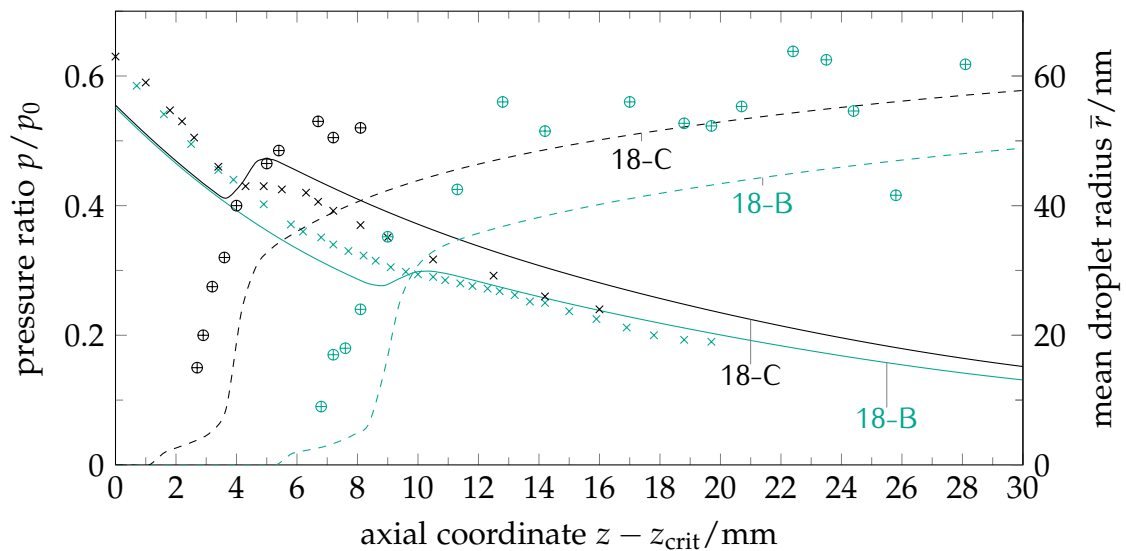
(b) Nozzle 4/B

test run designation	18-B	18-C
stagnation pressure p_0/bar	101	101
stagnation temperature T_0/°C	366	342

Figure 3.4: Simulation of experiments by Gyarmathy (2005), showing pressure distribution p/p_0 and average droplet radius $\bar{r}$ in the divergent nozzle section. The designations of the test runs correspond to the ones used by Gyarmathy.

	p/p_0	$\bar{r}$
experiment	×	⊕
simulation	——	- - -

[The] swelling of the jet is due to the fact that the internal pressure at the moment of discharge is greater than that of the medium into which it is flowing; [...] if [it were] lower, a contraction would be caused by the pressure of the air.

— Strickland Landis Kneass, *Practice and theory of the injector*, 1910

4 | GAS DYNAMIC PHENOMENA AT THE NOZZLE EXIT

A simulation approach for the gas dynamic adaptation of over- and underexpanded steam jets is presented. Analytical ideal gas solutions for oblique shocks and Prandtl–Meyer expansion fans are used as initial estimate for an iterative solution based on the two-phase conservation equations. A simplifying assumption of instantaneous non-equilibrium relaxation allows the use of a homogeneous equilibrium model. The initial shape of submerged steam jets is reproduced accurately by the model.

After expansion in the steam nozzle, the supersonic steam enters the mixing chamber. In this chapter, it is assumed that the steam enters a pool at ambient pressure p_∞ in order to separately study the processes at the nozzle exit.

In supersonic nozzle flow, information about the ambient state cannot propagate upstream. Therefore, the nozzle exit pressure p_e may be below (*overexpanded*) or above (*underexpanded*) the ambient pressure p_∞. Adaptation to the ambient state is then achieved after the nozzle outlet by a series of *oblique shocks* and *expansion fans*. For overexpanded jets, the course of events is as follows (fig. 4.1):

1. An oblique shock wave is formed at the nozzle exit. Across the shock, the pressure increases to the ambient pressure.

2. The shock causes a flow deflection towards the jet axis, i.e. a contraction.
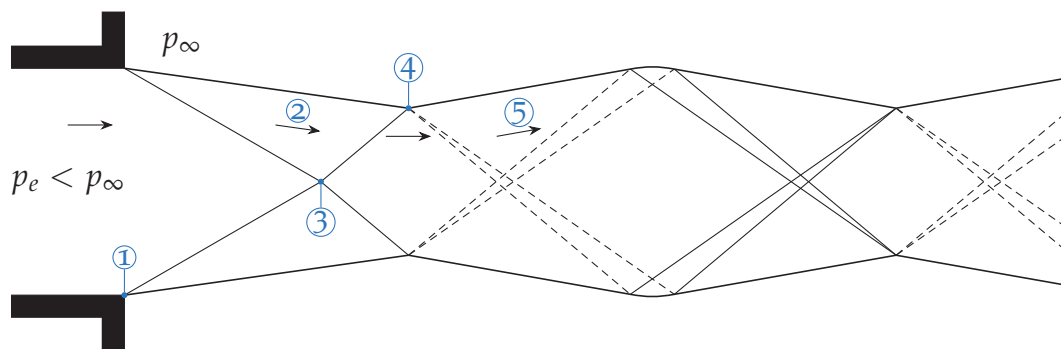
Figure 4.1: Gas dynamic phenomena in an overexpanded supersonic jet (nozzle exit pressure p_e below ambient pressure p_∞): (1) oblique shock wave (2) flow deflection towards jet axis (3) reflected shock (4) expansion fan (5) flow deflection away from jet axis

3. The oblique shock is reflected at the jet axis to maintain the symmetry condition (no radial velocity component at the jet axis), causing a further pressure rise.

4. In order to comply with the free jet boundary condition ($p = p_\infty$), this second shock is reflected at the jet boundary as an expansion fan, resulting in a pressure decrease.

5. Across the expansion fan, the flow is directed away from the jet axis and the jet expands radially.

This compression-expansion sequence recurs periodically until the structure disintegrates due to dissipation. For underexpanded jets, the sequence is analogous, starting with an expansion wave at the nozzle exit (step 4 in above list).

Calculation of oblique shocks and expansion fans is common practice for single-phase gas flows, while research on two-phase flows is less extensive. In the following, the governing equations and solution methods for single-phase gas flows are described. Subsequently, previous research on gas dynamic phenomena in two-phase flows is presented. Finally, a model approach for oblique shocks and expansion waves in pure steam flows is developed and compared to experimental data.

4.1 COMPRESSIBLE TWO–DIMENSIONAL GAS DYNAMICS

4.1.1 Oblique shock

Consider a supersonic flow towards an inwardly bent channel wall with a deflection angle ϑ (fig. 4.2a). Due to the supersonic nature of the flow, the change in flow direction occurs abruptly across an oblique shock wave (shock angle θ). For a given upstream Mach number Ma, the lower boundary of the shock angle is the Mach angle α_{Ma}, and the limiting case of a normal shock represents the upper boundary:

$$\alpha_{Ma} = \arcsin\left(1/Ma\right) \leq \theta \leq \tfrac{\pi}{2} \tag{4.1}$$

Across the shock, the velocity component normal to the shock front $c_\perp$ decreases, while the tangential velocity component $c_\parallel$ remains unchanged. Conservation of mass, momentum and energy requires

$$c_\parallel = \hat{c}_\parallel \quad , \tag{4.2}$$

$$\rho c_\perp = \hat{\rho} \hat{c}_\perp \quad , \tag{4.3}$$

$$p + \rho c_\perp^2 = \hat{p} + \hat{\rho} \hat{c}_\perp^2 \quad , \tag{4.4}$$

$$h + \tfrac{1}{2} c_\perp^2 = \hat{h} + \tfrac{1}{2} \hat{c}_\perp^2 \quad . \tag{4.5}$$

Here, $\hat{*}$ indicates a property downstream of the shock. The velocity components and angles are related as follows (fig. 4.2b):

$$c_\parallel = c \cos\theta = \hat{c}_x \cos\theta + \hat{c}_y \sin\theta \tag{4.6}$$

$$c_\perp = c \sin\theta \tag{4.7}$$

$$\hat{c}_\perp = c \sin\theta - \frac{\hat{c}_y}{\cos\theta} \tag{4.8}$$

$$\tan\vartheta = \frac{\hat{c}_y}{\hat{c}_x} \tag{4.9}$$

$$\tan\theta = \frac{c - \hat{c}_x}{\hat{c}_y} \tag{4.10}$$

Combination of eqs. (4.6) to (4.10) yields a relation between the shock angle and the deflection angle:

$$\tan\vartheta = \tan\theta \frac{1 - \frac{\hat{c}_\perp}{c_\perp}}{1 + \frac{\hat{c}_\perp}{c_\perp} \tan^2\theta} \tag{4.11}$$

(a) flow geometry

(b) velocity triangle
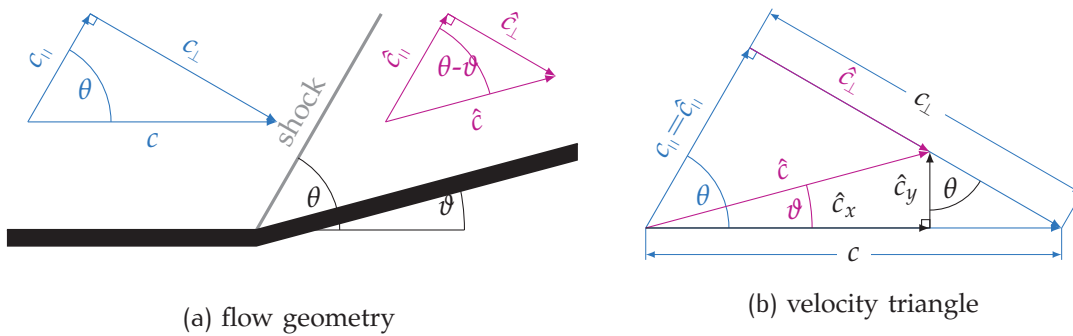
Figure 4.2: Schematic of an oblique shock
θ: shock angle; ϑ: deflection angle; c: velocity; $\parallel/\perp$: tangential/normal to the shock; $\hat{*}$: property downstream of the shock; x/y: horizontal/vertical component

Ideal gas solution

For an ideal gas, the conservation equations and geometric relations can be transformed as follows (Zierep, 1972):

$$\frac{\hat{c}_\perp}{c_\perp} = \frac{\rho}{\hat{\rho}} = 1 - \frac{2}{\varkappa + 1}\left(1 - \frac{1}{Ma^2 \sin^2\theta}\right) \tag{4.12}$$

$$\frac{\hat{p}}{p} = 1 + \frac{2\varkappa}{\varkappa + 1}\left(Ma^2 \sin^2\theta - 1\right) \tag{4.13}$$

$$\frac{\hat{T}}{T} = \frac{\hat{c}^2}{c^2} = \left[1 + \frac{2\varkappa}{\varkappa + 1}\left(Ma^2 \sin^2\theta - 1\right)\right]\left[1 - \frac{2}{\varkappa + 1}\left(1 - \frac{1}{Ma^2 \sin^2\theta}\right)\right] \tag{4.14}$$

$$\tan\vartheta = 2\cot\theta \frac{Ma^2 \sin^2\theta - 1}{Ma^2 \left(\varkappa + \cos 2\theta\right) + 2} \tag{4.15}$$

Here, $\varkappa = c_p/c_v$ is the isentropic exponent, and c_p and c_v are the specific isobaric/isochoric heat capacities [J/(kg K)], respectively.

Combination of eqs. (4.13) and (4.15) results in:

$$\tan\vartheta = \frac{\frac{\hat{p}}{p} - 1}{\varkappa\,Ma^2 - \left(\frac{\hat{p}}{p} - 1\right)}\sqrt{\frac{\frac{2\varkappa}{\varkappa+1}\left(Ma^2 - 1\right) - \left(\frac{\hat{p}}{p} - 1\right)}{\frac{\hat{p}}{p} + \frac{\varkappa - 1}{\varkappa + 1}}} \tag{4.16}$$

By considering the graphic representation of eq. (4.16), the following observations can be made (fig. 4.3):

- A unique solution for the post-shock state can be obtained from eqs. (4.12) to (4.14) if the shock angle θ or a downstream property ($\hat{p}$, $\hat{\rho}$, etc.) is known.

- However, there are multiple solutions for a given deflection angle ϑ: A strong shock solution ($\hat{Ma} < 1$), a weak solution ($\hat{Ma} \lessgtr 1$) and a physically invalid solution (decreasing entropy). The weak solution occurs in most practical applications (Zierep, 1972).

- There is no valid solution above a maximum deflection angle ϑ_{max}. For $\vartheta > \vartheta_{max}$, the shock detaches and a subsonic flow region is created between the shock and the wall corner.
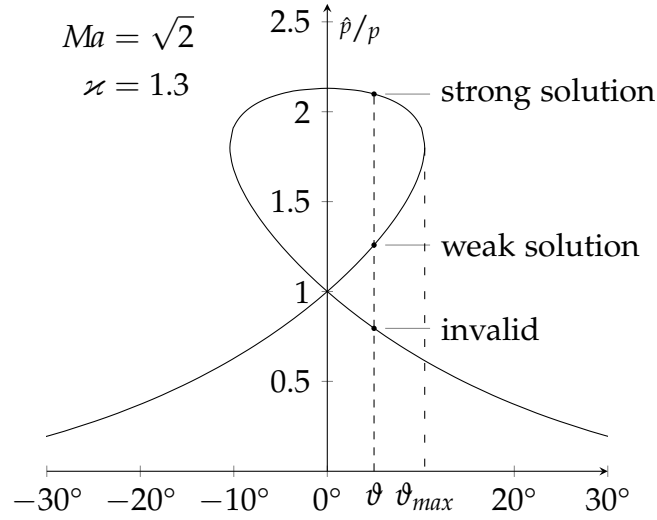
Figure 4.3: Oblique shock solutions (ideal gas) for a given deflection angle ϑ
$\hat{p}/p$: downstream/upstream pressure; Ma: upstream Mach number; $\varkappa$: isentropic exponent

In order to obtain an analytical, exact solution for the shock angle θ as a function of the deflection angle ϑ, Thompson (1950) transformed eq. (4.15) into the following form:

$$a \tan^3 \theta - \tan^2 \theta + b \tan \theta + c = 0 \tag{4.17}$$

$$a = \tan \vartheta \left(\frac{\varkappa - 1}{2} + \frac{\varkappa + 1}{2} \frac{1}{Ma^2 - 1} \right) \tag{4.18}$$

$$b = \tan \vartheta \left(\frac{\varkappa + 1}{2} + \frac{\varkappa + 3}{2} \frac{1}{Ma^2 - 1} \right) \tag{4.19}$$

$$c = \frac{1}{Ma^2 - 1} \tag{4.20}$$

This cubic equation has three solutions:

$$\tan \theta_n = \frac{b + 9ac}{2 (1 - 3ab)} - \frac{d \left(27ac^2 + 9ab - 2 \right)}{6a (1 - 3ab)} \cdot \tan \left[\frac{n}{3} \pi + \frac{1}{3} \arctan \frac{1}{d} \right] ; \tag{4.21}$$
$$n \in \{-1, 0, 1\}$$

$$d = \sqrt{\frac{4 (1 - 3ab)^3}{\left(27a^2c + 9ab - 2 \right)^2} - 1} \tag{4.22}$$

In eq. (4.21), $n = 0$ yields the weak solution, $n = 1$ the strong solution, and $n = -1$ the invalid solution.

4.1.2 Prandtl–Meyer expansion

Consider a supersonic flow towards an outwardly bent channel wall with a deflection angle ϑ (fig. 4.4). Just as in the case of an inwardly bent wall, information about the deflection cannot propagate upstream. However, while the inwardly bent wall causes a sudden, irreversible compression by means of an oblique shock, the outwardly bent wall causes a gradual, isentropic expansion via a sequence of infinitesimal Mach expansion waves.

Heims (1958) proposes to describe the expanding flow in a polar (r, φ)-coordinate system with the origin at the wall corner. Then, continuity and momentum conservation require

$$\frac{\mathrm{d}c_r}{\mathrm{d}\varphi} = c_\varphi = w \quad , \tag{4.23}$$

and the energy conservation can be written as

$$h_{tot} = h + \frac{c_\varphi^2 + c_r^2}{2} = const. \tag{4.24}$$
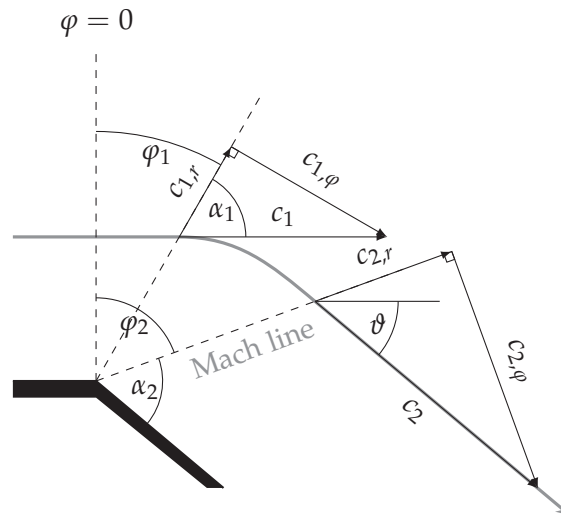
Figure 4.4: Schematic of a Prandtl-Meyer expansion
c: velocity; 1/2: upstream/downstream property; r/φ: radial/azimuthal coordinate; ϑ: deflection angle; α: Mach angle

Here, c_r and c_φ are the radial and azimuthal velocity components, w is the sonic velocity, and h_{tot} is the total enthalpy. Moreover, the following relations hold for the initial (upstream) flow state (index 1):

$$\cos \varphi_1 = 1/Ma_1 \tag{4.25}$$

$$c_{1,r} = w_1 \sqrt{Ma_1^2 - 1} \tag{4.26}$$

In order to integrate eq. (4.23), Heims introduces two auxiliary variables η and ψ:

$$\eta := 1 + \frac{2h}{w^2} \tag{4.27}$$

$$\frac{d\varphi}{d\psi} := \sqrt{\eta} \tag{4.28}$$

The flow field can now be obtained as a function of ψ:

$$c_r = \sqrt{2h_{tot}} \sin \psi \quad ; \quad \psi \geq \psi_1 \tag{4.29}$$

$$c_\varphi = w = \frac{\sqrt{2h_{tot}}}{\sqrt{\eta}} \cos \psi \tag{4.30}$$

$$Ma = \sqrt{1 + \left(c_r / c_\varphi \right)^2} = \sqrt{1 + \eta \tan^2 \psi} \tag{4.31}$$

$$\vartheta = \varphi - \arccos \left(1/Ma \right) \tag{4.32}$$

4.2 GAS DYNAMIC PHENOMENA IN TWO-PHASE FLOWS

Gas dynamic phenomena such as compression shocks or expansion waves may occur in dispersed droplet flows, just as in single-phase gas flows. However, the presence of liquid droplets in the continuous gas phase and the resulting exchange mechanisms have to be accounted for. Research in this field is mostly focused on condensable vapor flows with an inert carrier gas, e. g. moist air.

4.2.1 Two-phase compression shocks

Compression shocks cause an increase in pressure and temperature and a decrease in velocity. In dispersed droplet flows, this leads to a disturbance of the

phase equilibrium and therefore causes heat removal from the gas phase and partial or complete droplet evaporation. Consequently, the final downstream state may be either gas-liquid two-phase flow or superheated gas flow. Droplet evaporation is diffusion controlled in the presence of an inert gas, and heat transfer controlled for pure vapor-droplet flow (J. B. Young and Guha, 1991).

Two shock types may be distinguished in two-phase flows (Guha, 1992; J. B. Young and Guha, 1991): *Fully dispersed* shock waves with a continuous change between two equilibrium states, and *partly dispersed* shock waves. The latter start with a virtually discontinuous shock front, similar to pure gases. However, only the properties of the gas phase change across the shock front. The liquid phase is initially unaffected and a new equilibrium state is attained in the subsequent *droplet relaxation zone*. Even for very strong shocks, no droplet fragmentation occurs across the shock front according to a droplet stability criterion proposed by J. B. Young and Guha (1991).

For partly dispersed shocks, three different relaxation time scales t_{wb}, t_{me} and t_{ev} can be distinguished (Smolders and Dongen, 1992):

t_{wb}: The droplet temperature rises to a quasi-steady state ("wet bulb temperature").

t_{me}: Momentum is transferred from the droplets to the gas phase until mechanical equilibrium is reached.

t_{ev}: The droplets evaporate partially or fully and the gas temperature decreases.

Smolders and Dongen (1992) and J. B. Young and Guha (1991) show that the wet bulb temperature is reached before the mechanical equilibrium, and that droplet evaporation takes significantly longer than both other relaxation processes:

$$t_{wb} < t_{me} \ll t_{ev} \tag{4.33}$$

Model approaches

Kouremenos and Antonopoulos (1989) used a real gas equation of state to model oblique shock waves in pure steam and derived simplified empirical relations. Two-phase flow phenomena were not taken into account by the model.

J. B. Young and Guha (1991) simulated normal shocks in two-phase flows using a mixture model based on the droplet mass fraction and taking into account Knudsen effects in the exchange processes.

Smolders and Dongen (1992) used a similar approach, but assumed instantaneous temperature and velocity relaxation ($t_{wb} = 0$, $t_{me} = 0$) and thus only considered the process of droplet evaporation. The maximum relative error in the total evaporation time due to this simplification was quoted below 5 % for upstream Mach numbers less than $Ma = 2$.

Guha (1992) developed jump conditions between the equilibrium states up- and downstream of the shock region, which required no explicit consideration of the droplet relaxation process. He also presented a unified theory for aerodynamic and condensation shock waves in vapor-droplet flows in the presence of an inert carrier gas based on a mixture model (Guha, 1994).

4.2.2   Prandtl–Meyer expansion with non–equilibrium condensation

Experimental and numerical studies have shown that non-equilibrium condensation may occur during Prandtl–Meyer expansion of a condensable vapor with an inert carrier gas (Delale et al., 2007). The underlying mechanism is equivalent to steam expansion in a nozzle (chapter 3): The rapid expansion results in a metastable, supersaturated vapor state which will revert to equilibrium by means of homogeneous nucleation and droplet condensation. This may result in an oblique shock wave embedded in the expansion fan. Methods for numerical computation of such flows were presented, inter alia, by Delale and Crighton (1998) and Otobe et al. (2006).

4.3   MODEL DEVELOPMENT

As pointed out in the previous section, shocks and expansion waves in two-phase flows lead to a non-equilibrium state. In a steam injector, the subsequent relaxation processes (droplet evaporation for overexpanded flows, metastable condensation for underexpanded flows) occur simultaneously with the steam condensation on subcooled droplets in the mixing chamber.

In light of the objective of a computationally efficient model and the limited experimental data available for validation, a detailed treatment of the relaxation zone seems disproportionate. Therefore, a homogeneous equilibrium mixture (no slip, thermal equilibrium) is assumed in the model development, similar to the approach by Guha (1992) in developing normal shock jump conditions. Then,

the critical two-phase mass flux is characterized by the *homogeneous equilibrium speed of sound* (Oertel, 2012):

$$\frac{1}{w_h^2} = \left(\frac{x_g}{\rho_g} + \frac{x_l}{\rho_l} \right)^{-2} \left[\frac{1}{\rho_l^2 w_l^2} + x_g \left(\frac{1}{\rho_g^2 w_g^2} - \frac{1}{\rho_l^2 w_l^2} \right) - \left. \frac{\partial x_g}{\partial p} \right|_s \left(\frac{1}{\rho_g} - \frac{1}{\rho_l} \right) \right] \quad (4.34)$$

The nozzle exit state is determined iteratively under the assumption of isentropic and isenthalpic equilibrium expansion and a choked flow. Details on the procedure are given in appendix B.2.

4.3.1 Overexpanded nozzle flow

First shock: Adaptation to ambient pressure

At the nozzle exit, the oblique shock is determined by the ambient pressure, thus the downstream pressure is known ($\hat{p} = p_\infty$). Accordingly, a unique and analytical solution exists for ideal gases[1]. For the two-phase mixture, the shock solution is obtained by the following iterative procedure:

1. The shock angle θ is estimated by the ideal gas solution (eq. (4.13)).

2. The shock-normal upstream velocity is calculated according to eq. (4.7) ($c_\perp = c \sin \theta$).

3. The shock-normal downstream velocity is obtained by combining continuity and momentum conservation (eqs. (4.3) and (4.4)).

4. The energy equation (eq. (4.5)) is used to determine the downstream enthalpy $\hat{h}$.

5. The downstream density $\hat{\rho}$ is calculated from the state equation as a function of $\hat{p}$ and $\hat{h}$.

6. Steps 2–5 are iterated[2] until continuity (eq. (4.3)) is fulfilled.

7. The deflection angle ϑ is obtained from eq. (4.11).

update θ

---

[1] For strongly overexpanded jets, there may be no possible stationary solution and the shock will migrate upstream. This situation is not considered here.

[2] root bracketing algorithm algorithm according to appendix B.5

Second (reflected) shock

Across the second shock (reflection at the jet axis), the flow is deflected to maintain center line symmetry. Accordingly, the deflection angle ϑ is given and multiple solutions may exist. Again, an iterative procedure is required for the two-phase mixture flow:

1. The shock angle θ is estimated by the weak ideal gas solution according to Thompson (eqs. (4.17) to (4.22) with $n = 0$).

2. The shock-normal upstream velocity is calculated according to eq. (4.7) ($c_\perp = c \sin \theta$).

3. The shock-normal downstream velocity is obtained from the relation between the shock angle and the deflection angle (eq. (4.11)).

4. Combination of continuity and momentum conservation (eqs. (4.3) and (4.4)) yields the downstream pressure $\hat{p}$.

5. The energy equation (eq. (4.5)) is used to determine the downstream enthalpy $\hat{h}$.

6. The downstream density $\hat{\rho}$ is calculated from the state equation as a function of $\hat{p}$ and $\hat{h}$.

7. Steps 2–6 are iterated[3] until continuity (eq. (4.3)) is fulfilled.

update θ

4.3.2 Underexpanded nozzle flow

Due to the isentropic nature of the Prandtl-Meyer expansion, the thermodynamic state after the expansion can be determined from the equation of state as a function of the downstream pressure p_2 and entropy $s_2 = s_1$. The two-dimensional flow geometry is then calculated as follows:

1. The auxiliary variables η, ϕ for both up- and downstream state are calculated according to eqs. (4.27) and (4.30) based on the local enthalpy and sonic velocity.

2. Equation (4.31) is used to determine the downstream Mach number Ma_2 and thus the downstream velocity ($c_2 = Ma_2 \, w_{h,2}$).

3. The initial azimuthal angle φ_1 is obtained from eq. (4.25).

---

3 multidimensional root finding algorithm for $n = 1$ variables according to appendix B.5

4. Equation (4.28) is integrated from ψ_1 to ψ_2 in order to obtain the downstream azimuthal angle:

$$\varphi_2 = \int_{\psi_1}^{\psi_2} \sqrt{\eta}\, \mathrm{d}\psi + \varphi_1 \qquad\qquad \text{(4.28 revisited)}$$

The integration is performed numerically based on the QUADPACK-routine (Piessens et al., 1983) as implemented in the GNU *Scientific Library* (GSL) (Gough, 2009). An adaptive integration scheme based on the Gauss-Konrod quadrature method (41-point rule) is used (Kronrod, 1965).

5. Finally, the deflection angle is calculated from eq. (4.32).

4.4 VALIDATION

Wu et al. (2010a) measured the axial and radial temperature profiles in overexpanded submerged steam jets. Their results show a sharp temperature peak immediately after the nozzle exit. This can be explained by a partly dispersed shock with a sudden increase of the gas phase temperature, followed by a relaxation zone with heat removal from the gas phase and an associated temperature decrease. The developed model does not consider the relaxation process, and can therefore not predict this temperature peak.

Therefore, the experimental study on over- and underexpanded submerged steam jets by Wu et al. (2009b) is used for validation. Here, initially saturated steam was expanded in a nozzle and injected into a water pool at ambient pressure. Measurements were focused on geometric parameters such as the jet expansion ratio and jet length. A visual comparison between experiments and simulation results is presented in fig. 4.5. The figure shows the jet photographs taken by Wu et al., combined with the simulation results for the shock/expansion wave geometry. The deflection angle ϑ is accurately predicted in all four cases.

For overexpanded jets, the reflection of the shock wave at the jet axis causes an expansion wave when reaching the outer jet boundary (cf. fig. 4.1). This expansion is clearly visible in the experimental photograph. The calculated second shock wave (shock angle θ_2) for the weakly overexpanded jet (fig. 4.5b) reaches the jet boundary approximately at the location where the experimental jet expands outwards. For the strongly overexpanded jet (fig. 4.5b), no valid solution could be obtained for the second shock. This suggests a Mach reflection with a subsequent subsonic flow region instead of a regular shock reflection, which is beyond the scope of the present work.

(a) Strongly over-
    expanded
    flow
    $p_e = 0.54\,\text{bar}$
    $Ma_e = 1.8$
    $\dot{m}_e = 299\,\text{kg}/(\text{m}^2\,\text{s})$

$\theta_1 = 44.00°$ $\vartheta = 16.31°$

(b) Weakly over-
    expanded
    flow
    $p_e = 0.67\,\text{bar}$
    $Ma_e = 1.7$
    $\dot{m}_e = 346\,\text{kg}/(\text{m}^2\,\text{s})$

$\theta_1 = 41.73°$ $\vartheta = 11.12°$ $\theta_2 = 47.37°$

(c) Weakly under-
    expanded
    flow
    $p_e = 1.20\,\text{bar}$
    $Ma_e = 1.4$
    $\dot{m}_e = 484\,\text{kg}/(\text{m}^2\,\text{s})$

$\varphi_1 = 53.54°$ $\varphi_2 = 57.27°$ $\vartheta = 2.37°$

(d) Strongly under-
    expanded flow
    $p_e = 2.03\,\text{bar}$
    $Ma_e = 1.0$
    $\dot{m}_e = 585\,\text{kg}/(\text{m}^2\,\text{s})$

$\varphi_1 = 45.0°$ $\varphi_2 = 66.02°$ $\vartheta = 11.12°$
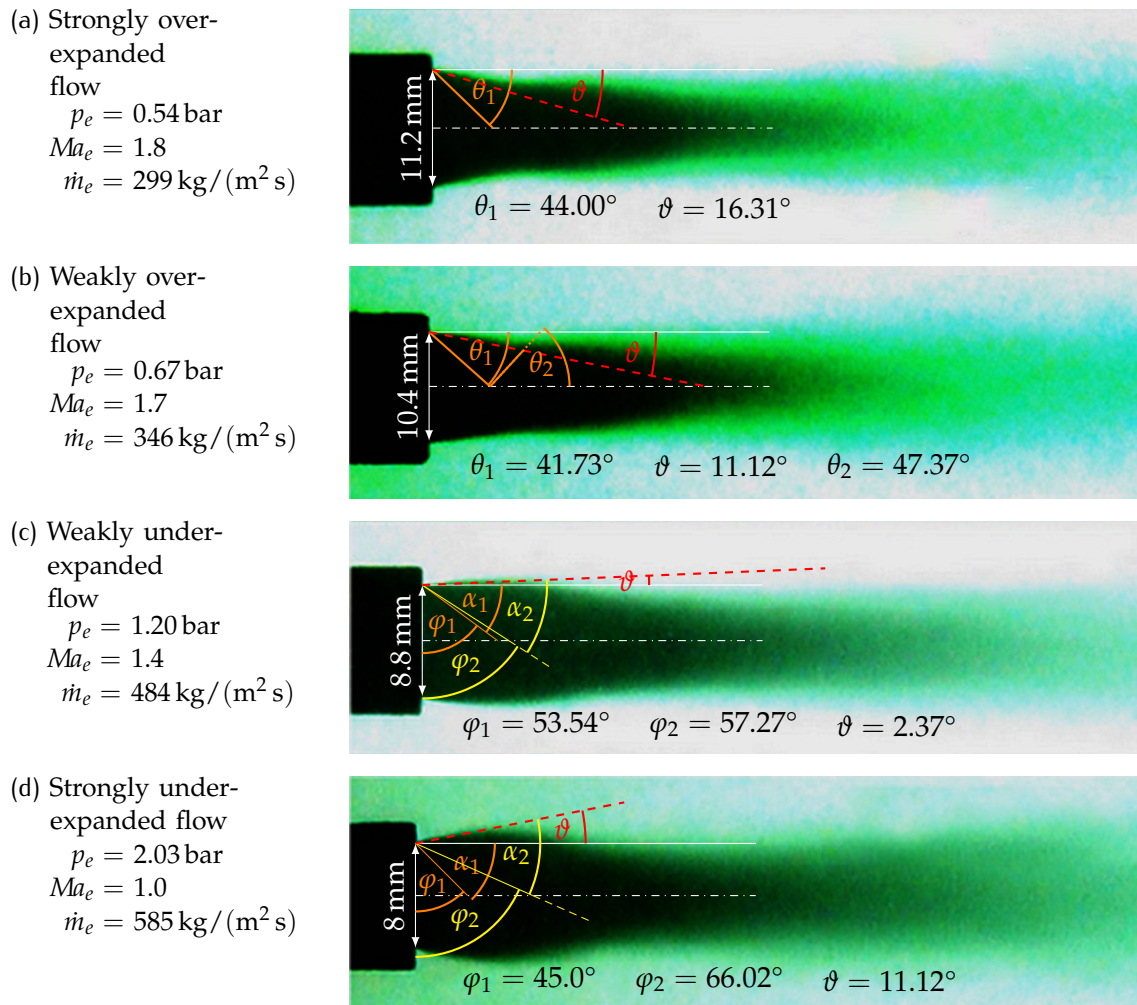
Figure 4.5: Visual comparison between simulation and experimental results of over- and under-expanded submerged steam jets – experimental data by Wu et al. (2009b), steam stagnation pressure $p_0 = 4\,\text{bar}$, ambient pressure $p_\infty = 1.02\,\text{bar}$.
$p_e/Ma_e/\dot{m}_e$: pressure/Mach number/mass flux at nozzle exit; θ: oblique shock angle; ϑ: deflection angle; φ: azimuthal coordinate; α: Mach angle
Jet photographs © 2009 Elsevier B. V., reprinted with permission

Da es sich bei den Strahlapparaten um turbulente Mischvorgänge handelt, könnte man vermuten, daß diese Vorgänge auf Grund des bekannten Ansatzes von Prandtl über turbulente Mischströmungen sich in exakter Weise berechnen lassen würden. Die mathematischen Schwierigkeiten sind aber hier so groß, daß [...] jener Ansatz kaum zu einem brauchbaren Rechenverfahren führen dürfte.

— Gustav Flügel, "Berechnung von Strahlapparaten", 1939

5 | DIRECT CONTACT CONDENSATION IN THE MIXING CHAMBER

A simulation model for the direct contact condensation of steam jets in pools and channels is presented. Entrainment of water into the steam jet is modeled based on the Kelvin–Helmholtz and Rayleigh–Taylor instability theories. Primary atomization due to acceleration of interfacial waves and secondary atomization due to aerodynamic forces account for the initial size of entrained droplets. Condensation at the interface between the steam jet and the surrounding water is calculated according to the surface renewal theory. The resulting steam–water two–phase flow is simulated based on a one–dimensional three–fluid model. An interfacial area transport equation is used to track changes of the interfacial area density due to droplet entrainment and steam condensation on droplets. Interfacial heat and mass transfer rates during condensation are calculated using the two–resistance model. The simulation results are in good qualitative agreement with published experimental data over a wide range of pool temperatures and mass flow rates. The trends for steam jet condensation in channels are also predicted by the model.

The mixing chamber or mixing nozzle is the most important part of a steam injector. Here, the high-velocity steam leaves the steam nozzle, mixes with the inlet water and condenses upon it. This process is called *direct contact condensation* (DCC). Efficient condensation is crucial for stable operation: The strong pressure rise at the mixing chamber throat can only occur if the steam condenses completely before entering the diffuser.

Direct contact condensation of a steam jet in subcooled water is based on two different mechanisms: The condensation directly at the steam-water interface on the one hand, and entrainment, atomization and subsequent droplet condensation on the other hand. Condensation due to atomization can be divided into two parts. First, the interface between the steam jet and the water is disrupted due to the high velocity difference between the two phases. Waves arise, expand into the high-speed gas phase and atomize to form small liquid droplets. The large interfacial area density obtained by this turbulent mixing process then establishes the basis for rapid steam condensation. Accordingly, the initial development of the two-phase jet flow is mainly governed by the momentum transfer from the high-velocity steam to the entrained droplets, while mass and heat transfer dominate with growing interfacial area density.

There is only limited experimental data for DCC in channels, i. e. confined environments. In contrast, DCC in pools, i. e. in free environments, has been broadly studied in the past. In channel DCC, the flow of the water surrounding the jet may be turbulent, which enhances the heat and mass transfer at the jet interface. Apart from this, it is believed that the same physical phenomena occur in both situations.

Therefore, an overview of studies of both pool and channel DCC is given subsequently, followed by a brief outline of the incompressible turbulent jet theory and its extension to two-phase jets. Afterwards, previous investigations concerning the mechanisms of heat and mass transfer at sheared interfaces are presented. The knowledge gained from these fields is then used to develop a simulation model for jet DCC. Finally, the simulation results obtained with this model are compared to experimental data from the literature.

5.1   PREVIOUS STUDIES

Numerous experimental and theoretical studies of DCC have been performed in the past to gain a better understanding of the occurring physical phenomena. However, experimental data is mostly limited to the global flow structure. Reliable information regarding the local fluid-dynamic properties is limited due to the complex two-phase flow which impedes experimental measurements.

5.1.1   Experimental observations

In general, three different DCC modes can be distinguished: *chugging*, *bubbling* and *jetting* (C. K. Chan and Lee, 1982). The oscillating flow modes of chugging and bubbling occur at low steam mass fluxes, while a stable jet flow appears as soon as the steam flow is choked, i. e. for sonic or supersonic steam injection (Song and Y.-S. Kim, 2011). The present work focuses on the jetting mode.

Three flow regimes have been observed during stable jet condensation (e. g. Song et al., 2012; Song and Y.-S. Kim, 2011):

1. The *vapor core* (also called *steam cavity*) in the immediate proximity of the injection nozzle, where the flow velocity is almost constant (Dahikar et al., 2010) and the axial and the radial temperature profiles are independent of the surrounding water temperature (Song et al., 2012; Song and Y.-S. Kim, 2011; Wu et al., 2010a).

2. The *mixing region*, where liquid droplets are entrained into the vapor core and provide a large interfacial area for steam condensation.

3. The *condensation-induced turbulent liquid jet*, which has been shown to be in good agreement with the incompressible turbulent jet theory (section 5.2).

In the first two regions, two exchange mechanisms have been identified (Y.-S. Kim et al., 2004; Song et al., 2012): Wave formation, atomization and droplet condensation on the one hand, and condensation at the interface between the vapor jet and the surrounding water on the other hand. If the surrounding water is stagnant, interfacial eddies are believed to result mainly from the kinetic energy carried by the condensing steam (Liang and Peter-Griffith, 1994), while the bulk liquid turbulence must be considered if the water is in motion (Q. Xu et al., 2013).

The jet shape mainly depends on the steam injection velocity and the water temperature. For subsonic injection, *conical*, *ellipsoidal* and *divergent* shapes (fig. 5.1) have been identified (H. Y. Kim et al., 2001; Song et al., 2012), while four additional shapes were observed for supersonic injection: *double expansion-contraction*, *double expansion-emanative*, *contraction-expansion-contraction*, and *contraction-expansion-emanative*. The supersonic jet shapes result from oblique shocks and expansion waves in over- and underexpanded jets (H. Y. Kim et al., 2001; Wu et al., 2007), as discussed in chapter 4. These phenomena influence the flow structure near the nozzle exit and become more pronounced with increasing water temperature (fig. 5.2).

One of the major parameters to characterize the DCC flow is the *dimensionless jet penetration length L*, which is defined as the ratio of the jet penetration length l [m] to the nozzle exit diameter d_e:

$$L = l/d_e \tag{5.1}$$
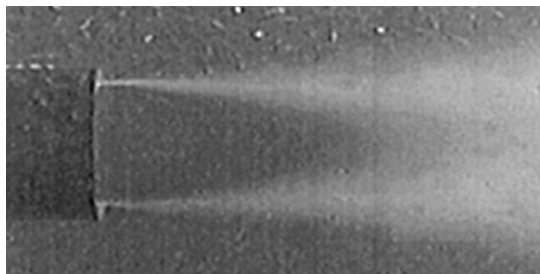
(a) Conical shape (low steam mass flux)   (b) Ellipsoidal shape (high steam mass flux)
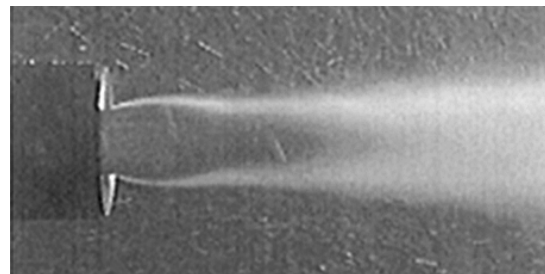
Figure 5.1: Steam jet shapes observed by H. Y. Kim et al. (2001)
© 2001 John Wiley & Sons, Inc., reprinted with permission
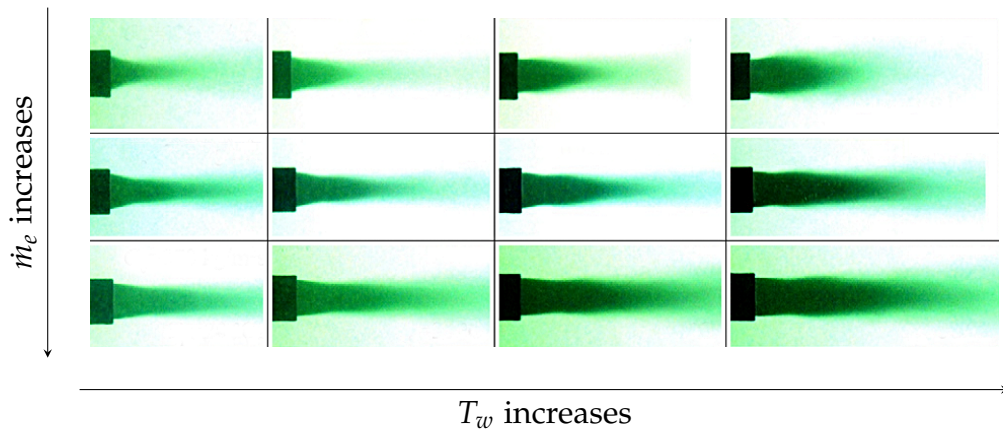
Figure 5.2: Shapes of overexpanded supersonic steam jets ($p_e < p_w$) observed by Wu et al. (2010a). The steam mass flux $\dot{m}_e$ varies with the steam stagnation pressure p_0. Therefore, the nozzle exit pressure p_e rises with increasing steam mass flux, thus reducing the underexpansion of the jet (p_e/p_w) and consequently the contraction angle at the nozzle exit. The evolving contraction-expansion pattern becomes more pronounced with increasing water temperature T_w.
© 2009 Elsevier Inc., reprinted with permission
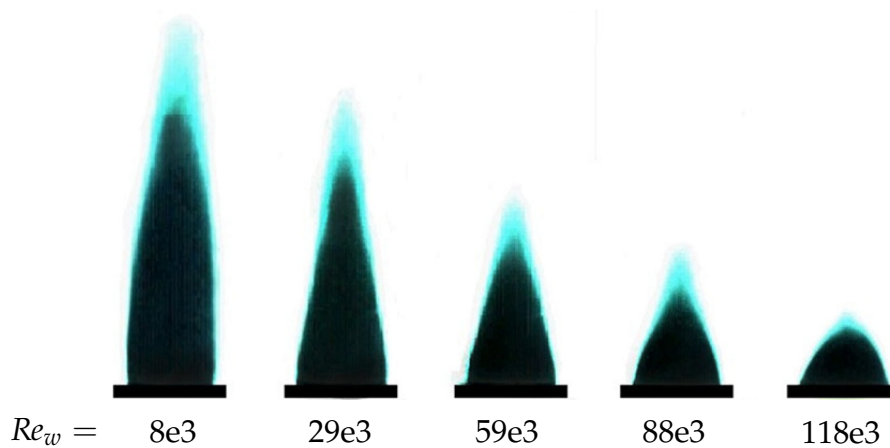
Figure 5.3: Decrease of steam jet length with rising Reynolds number of the surrounding water Re_w during channel DCC as observed by Q. Xu et al. (2013)
© 2013 Elsevier Ltd., reprinted with permission
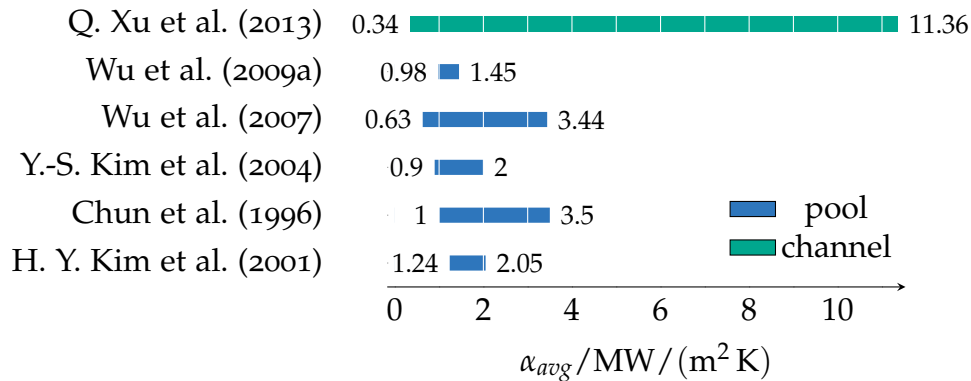
Figure 5.4: Range of measured average DCC heat transfer coefficients α_{avg}

Most measurements of L rely on visual observation and are therefore subject to a large experimental bias (Gulawani et al., 2006). Nevertheless, various investigators have shown that for pool DCC, L is mainly dependent on the steam mass flux and the temperature of the water pool (Song et al., 2012). Both jet length and expansion ratio (maximum jet diameter divided by nozzle diameter) will increase if either of these parameters rises. For channel DCC, jet shape and length furthermore strongly depend on the water flow rate. Q. Xu et al. (2013) report a decrease of the dimensionless jet penetration length L by 64 % to 82 % as the flow Reynolds number Re_w increases from 8×10^3 to 118×10^3 (fig. 5.3). A similar decrease of 60 % to 65 % has been observed by de With (2009) for a Reynolds number of approximately[1] $Re_w \approx 10^5$. With increasing water flow rate, the influence of steam mass flux and water temperature decreases (Q. Xu et al., 2013).

For (super-)sonic jet injection, various authors report average heat transfer coefficients in the order of $10^6\,\mathrm{W}/(\mathrm{m}^2\,\mathrm{K})$ (fig. 5.4), which is five to ten times above the average of subsonic jets (Simpson and C. K. Chan, 1982) and indicates the virtual absence of a laminar sublayer at the jet interface (Liang, 1991). These measurements are generally based on a global energy balance and assume a smooth gas-liquid interface, e. g. a conical jet shape. According to Aya and Nariai (1991), this approach offers engineering conveniences, but one should keep in mind that the "real" jet interface will be wrinkled and additional interfacial area is provided by the entrained droplets. Therefore, the local heat transfer coefficient may be much lower than these global average values. For instance, local measurements by Gulawani et al. (2009) indicate heat transfer coefficients between $10^3\,\mathrm{W}/(\mathrm{m}^2\,\mathrm{K})$ and $10^7\,\mathrm{W}/(\mathrm{m}^2\,\mathrm{K})$.

---

1 estimated assuming a pipe diameter of 60 mm based on a photograph of the experimental setup in Petrovic-de With, 2006 and the provided flow velocity of 1.9 m/s

Measurements by H. Y. Kim et al. (2001) show that buoyancy forces may be neglected with respect to the high inertial forces of the steam jet. This is corroborated by a theoretical criterion given by Richards and Pitts (1993), stating that buoyancy effects can be neglected if

$$\hat{z}_B = Fr^{-1/2} \left(\rho_g \big/ \rho_\infty \right)^{-1/4} z \big/ d_e < 0.5 \quad , \tag{5.2}$$

where ρ_g and ρ_∞ are the densities of the gas phase and the ambient fluid, respectively. Van Wissen et al. (2004) estimate a Froude number $Fr \approx 10^{16}$ and thus $\hat{z}_B \approx 10^{-7} \ll 0.5$.

5.1.2   Modeling approaches

(Semi-)Empirical correlations

Kerney et al. (1972) derived a semi-empirical correlation for the jet penetration length in a pool based on the nozzle diameter, the mass flux at the nozzle exit $\dot{m}_e$ [kg/(m^2 s)] and the rate of subcooling:

$$L = l/d_e = S_m \left(\dot{m}_e / \dot{m}_{crit} \right)^{0.5} B^{-1} \tag{5.3}$$

Here, the *transport modulus S_m* is an empirical parameter analogous to the Stanton number of convective heat transfer, and $\dot{m}_{crit}$ is the critical mass flux of saturated single-phase steam at ambient water pressure (275 kg/(m^2 s)). The *condensation driving potential B* is defined as

$$B = c_p \left(T_{sat} - T_\infty \right) \big/ h_{lg} \quad , \tag{5.4}$$

where c_p is the specific isobaric heat capacity [J/(kg K)], T_{sat} and T_∞ are the saturation temperature [K] and the temperature of the ambient water, respectively, and h_{lg} is the specific condensation enthalpy [J/kg].

This correlation was later revised by Weimer et al. (1973) based on a homogeneous equilibrium mixture model in order to account for the influence of water pressure, droplet entrainment and bubble formation. Nevertheless, most subsequent authors have relied on the original formulation when deriving similar correlations for pool DCC (Chun et al., 1996; H. Y. Kim et al., 2001; Wu et al., 2010a). Wu et al. (2009a, 2007) attempted to account for gas dynamic effects by including the nozzle exit pressure in their correlation, while de With (2009)

derived a correlation based on the Reynolds number Re_e at the nozzle exit and the condensation driving potential B. Moreover, Q. Xu et al. (2013) proposed a correlation for channel DCC which takes into account the influence of the flow Reynolds number Re_w.

In general, these empirical correlations agree well with the experimental data that was used to derive the correlation. However, there is substantial disagreement when applying the various correlations to a single experimental data set (Gulawani et al., 2006).

Additionally, several authors proposed empirical correlations for other jet parameters such as the jet expansion ratio (Wu et al., 2009a,b, 2007) or the average heat transfer coefficient (Aya and Nariai, 1991; Chun et al., 1996; Gulawani et al., 2006; Y.-S. Kim et al., 2004). Here, Gulawani et al. (2006) observed a strong influence of the nozzle exit diameter on the heat transfer and thus distinguished between small ($d_e < 2\,\text{mm}$) and large ($d_e > 6\,\text{mm}$) nozzles, while other authors such as H. Y. Kim et al. (2001) argued that the influence of the nozzle diameter is negligible.

Lastly, Y.-S. Kim et al. (2004) proposed three different semi-empirical models to determine the interfacial heat transfer coefficient:

- An "interfacial transport model due to the turbulent intensity" based on the ratio between the thermal boundary layer thickness and the integral eddy size (assumed to be equal to the value for single-phase turbulence) and an experimental value for the Stanton number;

- a "surface renewal model" based on a predefined jet shape and using an experimental value for the period between turbulent bursts at the interface; and

- a "shear stress model", using a correlation for the Stanton number in addition to the assumptions of the "surface renewal model".

Simulation models

One of the first simulation models was proposed by Weimer et al. (1973). Their measurements indicated that the radial mass and energy transport is faster than the momentum transport. Accordingly, they suggested that the radial density and enthalpy profiles are wider than the velocity profile, just as in turbulent single-phase jets. Furthermore, they presumed isentropic adaptation of the steam nozzle exit state to the ambient pool pressure. Based on these presuppositions, they derived a one-dimensional homogeneous mixture model, assuming

a symmetrical bubbly flow in the two-phase jet region. Turbulent mixing of the surrounding water into the two-phase jet was modeled according to the turbulent entrainment assumption, which requires an empirical entrainment constant (cf. section 5.2). By introducing a second empirical constant to model the radial enthalpy distribution, they used their model to derive a correlation for the dimensionless jet penetration length, as already mentioned in the previous section. It is noteworthy that later experiments on air jets submerged in water (Loth and Faeth, 1989) confirm the validity of the aforementioned assumptions.

Petrovic (2005) used a one-dimensional two-fluid model to determine the dimensionless jet penetration length based on four different predefined jet shapes. The heat transfer coefficient used for the calculation of heat and mass transfer was varied between 1.4 and $8\,\mathrm{MW/(m^2\,K)}$ in order to obtain good agreement with experimental data.

More detailed analyses have been performed using CFD. In most models, the void distribution and the rate of condensation are estimated based on local turbulence values (Gulawani et al., 2009, 2006), often in conjunction with a probability density function (Chen and Faeth, 1982). Additional information can be found in a review article by Gulawani et al. (2007).

5.2   INCOMPRESSIBLE TURBULENT JET THEORY

5.2.1   Free circular jets

The flow of an incompressible single-phase fluid jet into an ambient, stagnant environment of the same fluid has been extensively studied in the past. This section provides a brief outline based on the detailed treatment by Rajaratnam (1976).

Experimental observations have shown that the flow field of incompressible jets can be divided into two regions: The *flow development region* in the immediate proximity of the nozzle exit, followed by the *fully developed flow region* (fig. 5.5).

THE FLOW DEVELOPMENT REGION   consists of an undisturbed *potential core* surrounded by an an annular shear layer. The shear layer arises from the initial velocity discontinuity at the jet boundary and expands inwards into the core region and outwards into the ambient fluid, thereby flattening the radial velocity gradient. The velocity profiles in the shear layer are self-similar and can be
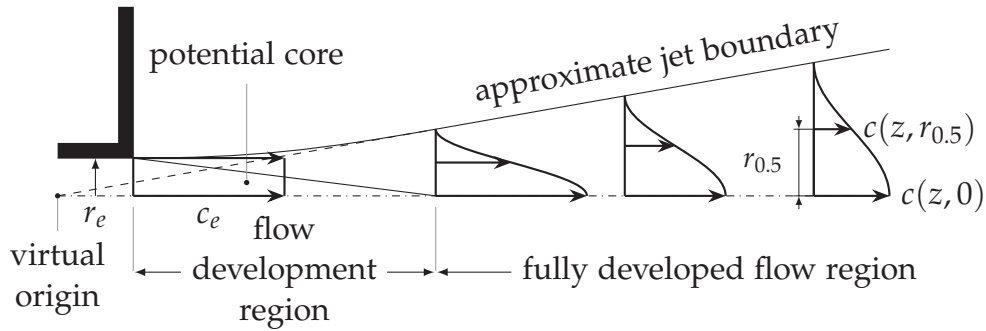
Figure 5.5: Schematic of a free circular jet, following Rajaratnam (1976) – flow development region with an undisturbed potential core and fully developed jet with a self-similar velocity profile
c_e: nozzle exit velocity; r_e: nozzle radius; $r_{0.5}$: jet half radius

described by a cosine function, and the length of the potential core is about $5d_e$ (Rajaratnam, 1976).

THE FULLY DEVELOPED FLOW REGION begins at the end of the potential core. From this point on, the centerline velocity decreases and the entire jet velocity profile becomes self-similar, as confirmed by various experiments (cf. Rajaratnam, 1976). The radial profile of the axial velocity $c(z, r)$ can be satisfactorily described by a Gauss-distribution based on the centerline velocity $c(z, 0)$ and the jet half radius $r_{0.5}$:

$$\frac{c(z, r)}{c(z, 0)} = \exp\left[-\ln 2 \left(\frac{r}{r_{0.5}}\right)^2 \right] \tag{5.5}$$

The jet half radius $r_{0.5}$ is the radial location where the axial velocity is one half of the centerline velocity.

Experiments have shown that both the centerline velocity and the jet half radius are proportional to the distance from the virtual origin of the jet. Due to the uncertainties in predicting this distance, Rajaratnam recommends to locate the virtual origin at the nozzle exit and suggests

$$\frac{c(z, 0)}{c_e} = 6.3 \left(\frac{z}{d_e}\right)^{-1} \quad , \tag{5.6}$$

$$r_{0.5} = 0.1 \cdot z \tag{5.7}$$

upon comparing various experimental results.

The velocity profile can be calculated with the well-known models by Tollmien (1926) and Görtler (1942). Both approaches assume a two dimensional flow field

with the axial velocity component being much larger than the radial one and no pressure gradient in the axial direction. Moreover, it is presumed that laminar shear stress can be neglected with respect to turbulent shear stress.

Tollmien obtained a non-linear second-order ordinary differential equation and solved it iteratively. The equation was derived using Prandtl's mixing length hypothesis (Prandtl, 1925) for the turbulent shear stress

$$\tau = \rho l_m^2 \left(\frac{\partial c}{\partial r} \right)^2 \quad , \tag{5.8}$$

where the *mixing length* l_m [m] was assumed to be proportional to the jet half radius ($l_m \propto r_{0.5}$).

Görtler obtained a non-linear first-order ordinary differential equation with an analytical solution. Here, the turbulent shear stress was calculated based on Prandtl's eddy-viscosity concept (Prandtl, 1925)

$$\tau = \rho \varepsilon \frac{\partial c}{\partial r} \tag{5.9}$$

and the *coefficient of kinematic eddy viscosity* ε [m²/s] was modeled as $\varepsilon \propto c(z,0) \, r_{0.5}$.

Both solutions agree well with experimental data; according to Rajaratnam, the Görtler-solution is slightly superior near the axis of the jet, while the Tollmien-solution offers a better prediction in the outer jet regions.

Experiments by Dahikar et al. (2010), Y.-S. Kim and Youn (2008), and Wu et al. (2010b) show that the turbulent jet induced by direct contact condensation of a submerged steam jet is in good agreement with the incompressible turbulent jet theory. Its dimensionless velocity profile is representable by a Gauss curve (Wu et al., 2010b) and can be modeled based on the Tollmien-model (Y.-S. Kim and Youn, 2008; Song et al., 2012).

Entrainment hypothesis

The mixing of a turbulent jet with the surrounding fluid can be described by the turbulent entrainment assumption, initially derived for hot gases rising in air (Morton et al., 1956; Taylor, 1945). The model considers the change of the jet mass flow rate $\dot{M}$ along the jet axis due to the radial inflow of fluid with an *entrainment velocity* c_{en}. By introducing an appropriate outer jet boundary R where the axial flow velocity is close to zero, this can be expressed as

$$\frac{\mathrm{d}\dot{M}}{\mathrm{d}z} = \rho \frac{\mathrm{d}}{\mathrm{d}z} \int_0^\infty 2\pi c r \, \mathrm{d}r = 2\pi R \rho c_{en} \quad . \tag{5.10}$$

Dimensional considerations suggest

$$c_{en} \propto c(z,0) \quad \Leftrightarrow \quad c_{en} = E_0 \cdot c(z,0) \quad , \tag{5.11}$$

where E_0 is known as the *entrainment coefficient*.

For jets with constant density, Rajaratnam proposes $E_0 = 0.026$ in the fully developed region. Based on experimental data by Hill (1965), he shows that the entrainment coefficient in the developing region is initially smaller than 0.026 and increases to the fully developed value at $z/d_e \approx 4$.

5.2.2 Confined jets

The previous section treated the expansion of a jet into an unbounded, stagnant fluid. This section highlights some important aspects when a jet inside a duct of constant diameter ($d_2 = 2r_2$) is considered (fig. 5.6). In this situation, the flow behavior differs from free jets because the flow field is radially bounded and the surrounding fluid is also in motion. The jet is generally referred to as *primary stream* and the surrounding fluid as *secondary stream* (indices 1 and 2, resp.).

If the inlet velocity of the primary stream is considerably greater than the one of the secondary stream ($c_1 \gg c_2$), four flow regions can be distinguished:

Region 1 until the end of the potential core;

Region 2 where the jet continues to expand outwards, retarding the secondary stream until it is completely consumed;

Region 3 where a stable recirculation eddy may be formed under certain flow conditions; and

Region 4 where the flow degenerates to fully developed pipe flow.

According to Rajaratnam, the velocity distribution is self-similar in all four regions.

In general, confined jets can be treated with similar methods as free jets. However, Rajaratnam points out that the assumption of a virtual point source for the jet becomes invalid for small values of d_2/d_1. This implies that the influence of the diameter ratio has to be taken into account if the nozzle is large with respect to the duct.
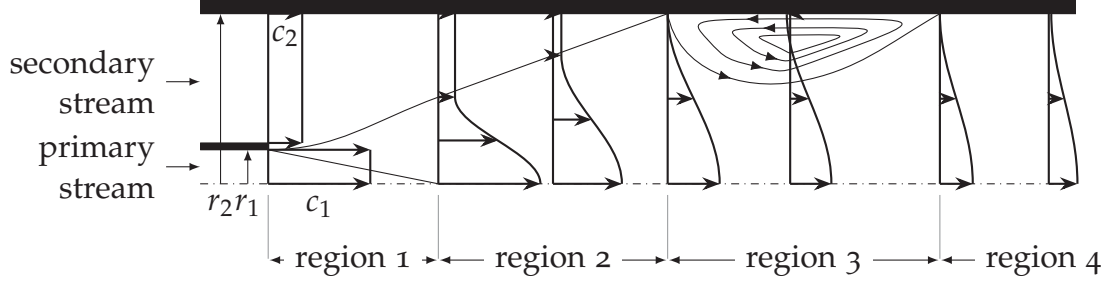
Figure 5.6: Schematic of a confined circular jet, following Rajaratnam (1976) – region 1: developing jet with potential core; region 2: expanding jet; region 3: recirculation vortex; region 4: degeneration into pipe flow

c_1, c_2: primary and secondary stream velocity; r_1, r_2: jet and pipe radius

For sufficiently large diameter ratios, the *Craya-Courtet number Ct* can be used to describe the flow behavior. This dimensionless parameter was introduced by H. A. Becker et al. (1963) as

$$Ct = \frac{c_{km}}{\left(c_{dm}^2 - \frac{1}{2}c_{km}^2 \right)^{1/2}} \tag{5.12}$$

based on the *kinematic mean velocity* and *dynamic mean velocity*:

$$c_{km} = (c_1 - c_2) \left(r_1/r_2 \right)^2 + c_2 \tag{5.13}$$

$$c_{dm}^2 = \left(c_1^2 - c_2^2 \right) \left(r_1/r_2 \right)^2 + \frac{1}{2}c_2^2 \tag{5.14}$$

According to H. A. Becker et al., recirculation occurs for $Ct < Ct^* = 0.75$. In addition, Rajaratnam (1976) points out that for decreasing values of Ct

- the recirculation zone grows larger,
- the pressure rise in the recirculation zone increases, and
- the variation of c_2 along the axis increases.

For large values of Ct, the jet boundary $r_1(z)$ varies linearly with z – similar to free jets –, whereas the relation becomes non-linear for smaller values ($Ct \lesssim 0.6$). The axial variation of the inverse relative centerline velocity $\left(c(z,0) - c_2(z) \right)^{-1}$ is linear only in a limited range of $Ct \approx 0.6$ and non-linear for both larger and smaller values.

5.3 TWO-PHASE JETS

Experimental studies of round gas jets submerged in water show that such jets exhibit qualitative similarities to incompressible single-phase jets. For instance, Loth and Faeth (1989) reported dynamic pressure profiles which are comparable to single-phase jets. Their measurements show a constant dynamic pressure at the jet centerline for $z/d_e \lesssim 4$, indicating the presence of an undisturbed potential core of similar length as in incompressible jets. Furthermore, the authors report that the entrainment coefficient remains nearly constant when buoyancy can be neglected.

In contrast to incompressible single-phase jets, the influence of the fluid density has to be taken into account when treating two-phase jets. For submerged gas jets, the liquid density is normally much larger than the gas density and the entrained fluid will quickly decelerate the jet due to its high inertia. Moreover, the surface tension has to be considered for immiscible fluids, where entrainment occurs due to the atomization of interfacial waves.

5.3.1 Extension of the entrainment hypothesis

The entrainment assumption (eq. (5.11)) has been extended to miscible gases with high density differences by Ricou and Spalding (1961), resulting in

$$c_{en} = E_0 \sqrt{\rho_m/\rho_\infty}\, c_m \quad .$$

(5.15)

Here, ρ_∞ is the density of the entrained fluid and ρ_m is the local mean density of the jet flowing with the velocity c_m. The entrainment coefficient has been experimentally determined in the range of 0.06 to 0.12 with a recommended value of 0.08.

Equation (5.15) has been successfully applied to sonic and supersonic gas and vapor jets in subcooled liquids (Fauske and Grolmes, 1992; Weimer et al., 1973). This extension from miscible to immiscible fluids can be corroborated using the Kelvin-Helmholtz instability theory (Epstein and Fauske, 2001), which describes the formation of waves and vorticities due to velocity shear between two fluids. Linear stability analysis yields the most amplified wave length at a gas-liquid interface

$$\tilde{\lambda}_{KH} = \frac{2\pi\sigma(\rho_l + \rho_g)}{\rho_l\rho_g \left(c_g - c_l\right)^2}$$

(5.16)

and the corresponding amplification rate [1/s]

$$\omega_{KH} = \frac{2\pi}{\tilde{\lambda}_{KH}} \frac{\sqrt{\rho_g \rho_l}}{\rho_l + \rho_g} \left(c_g - c_l \right) \quad . \tag{5.17}$$

In eqs. (5.16) and (5.17), σ is the surface tension [kg/s^2], and the indices g and l indicate the gas and liquid phase (fast/slow fluid), respectively. Epstein and Fauske (2001) show that $c_{en} \sim \tilde{\lambda}_{KH} \omega_{KH}$, which yields the entrainment velocity based on eqs. (5.16) and (5.17) as

$$c_{en} = \frac{E_0}{2\pi} \tilde{\lambda}_{KH} \omega_{KH} = E_0 \frac{\sqrt{\rho_g \rho_l}}{\rho_l + \rho_g} \left(c_g - c_l \right) \quad . \tag{5.18}$$

By using $E_0/(2\pi)$ as proportionality constant, the right-hand side of eq. (5.18) reduces to the empirical eq. (5.15) for $\rho_\infty = \rho_l$, $\rho_g = \rho_m$, $c_m = c_g$ and $c_l = 0$ in the limiting case of $\rho_l \gg \rho_g$.

Equation (5.18) is well suitable for developed turbulent jets. However, in most practical applications the two fluid streams are initially separated by a rigid boundary, which introduces the boundary layer as an additional length scale (Villermaux, 1998). In this case, the Kelvin-Helmholtz wavelength is initially proportional to the vorticity layer thickness in the gas stream δ_g (Raynal, 1997):

$$\tilde{\lambda}_{KH} \sim \delta_g \sqrt{\rho_l / \rho_g} \tag{5.19}$$

Moreover, studies on submerged gas jets (Weiland and Vlachos, 2013) and on liquid jets surrounded by an annular high-speed gas stream (Varga et al., 2003) have shown that the Rayleigh-Taylor instability mechanism is of similar significance as the Kelvin-Helmholtz instability in the developing jet region, i.e. near the nozzle exit.

The Rayleigh-Taylor instability amplifies interfacial disturbances if a dense fluid l is being accelerated into a lighter fluid g. Here, the most amplified wavelength and amplification rate are obtained based on the acceleration a [m/s^2] and the wave number $k = 2\pi/\tilde{\lambda}$ as

$$\tilde{\lambda}_{RT} = 2\pi \sqrt{\frac{3\sigma}{\left(\rho_l - \rho_g \right) a}} \quad , \tag{5.20}$$

$$\omega_{RT}^2 = \frac{k \left[\left(\rho_l - \rho_g \right) a - k^2 \sigma \right]}{\rho_l + \rho_g} \quad . \tag{5.21}$$
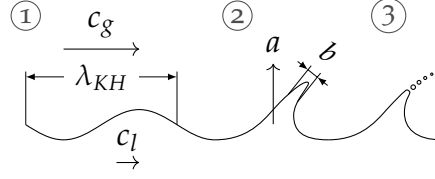
Figure 5.7: Entrainment and atomization at a gas-liquid interface according to Varga et al. (2003). (1) Primary instability due to velocity shear, (2) secondary instability due to acceleration of wave crests, (3) primary atomization
c_g, c_l: gas and liquid phase velocity; $\tilde{\lambda}_{KH}$: Kelvin-Helmholtz wavelength; a: wave acceleration; b: wave crest thickness

Varga et al. (2003) propose that the Rayleigh-Taylor instability acts as a secondary destabilization mechanism of the liquid wave crests resulting from the primary Kelvin-Helmholtz instability of the jet surface (fig. 5.7). This allows to determine the wave acceleration as

$$a = \frac{1}{b}\frac{\rho_g}{\rho_l}\left[c_g\left(1 - \frac{\sqrt{\rho_g}}{\sqrt{\rho_l} + \sqrt{\rho_g}}\right) - c_l\frac{\sqrt{\rho_l}}{\sqrt{\rho_l} + \sqrt{\rho_g}}\right]^2 \quad , \tag{5.22}$$

where b is the wave crest thickness, which has been experimentally determined as $b \approx \tilde{\lambda}_{KH}/10$. Assuming that the vorticity thickness δ_g is proportional to the boundary-layer thickness and scales as $\sqrt{\nu_g/c_g}$, eq. (5.19) yields the primary instability wavelength as

$$\tilde{\lambda}_{KH} = \gamma\sqrt{\nu_g/c_g}\sqrt{\rho_l/\rho_g} \quad . \tag{5.23}$$

Here, ν_g is the kinematic viscosity of the gas phase [m^2/s] and $\gamma \approx 0.055\,\mathrm{m}^{1/2}$ is an experimentally determined proportionality factor for the vorticity layer.

Non-isothermal Craya-Curtet number

For fluids with different densities, Steward and Guruz (1977) extended the definition of the Craya-Courtet number (eq. (5.12)) by introducing a mean density

$$\rho_m = \frac{r_1^2 c_1 \rho_1 + \left(r_2^2 - r_1^2\right)c_2\rho_2}{r_1^2 c_1 + \left(r_2^2 - r_1^2\right)c_2} \tag{5.24}$$

and non-isothermal versions of the kinematic and dynamic mean velocity:

$$c_{km,ni} = \frac{(c_1\rho_1 - c_2\rho_2)\left(r_1/r_2\right)^2 + c_2\rho_2}{\rho_m} \tag{5.25}$$

$$c_{dm,ni}^2 = \frac{\left(c_1^2\rho_1 - c_2^2\rho_2\right)\left(r_1/r_2\right)^2 + \frac{1}{2}c_2^2\rho_2}{\rho_m} \tag{5.26}$$

Then, the *non-isothermal Craya-Curtet number* Ct_{ni} can be obtained as

$$Ct_{ni} = \frac{c_{km,ni}}{\left(c_{dm,ni}^2 - \frac{1}{2}c_{km,ni}^2\right)^{1/2}} \quad . \tag{5.27}$$

5.3.2   Atomization at sheared gas–liquid interfaces

If the velocity difference at a gas-liquid interface is sufficiently high, *atomization* occurs: The surface waves break up and form liquid droplets which are entrained into the gas flow. In steam injectors, Deberne et al. (2000) estimated a mean droplet diameter of $5\,\mu m$ based on an atomization correlation by Monote (1994). For the sonic injection of nitrogen in water, Epstein et al. (2005) measured entrained droplets with a Sauter mean diameter in the range of $10\,\mu m$ to $100\,\mu m$ close to the nozzle exit ($z/d_e = 1$). They observed larger droplet sizes when increasing the nozzle diameter. For gas velocities in the range of $300\,m/s$, Someya et al. (2011) reports initial velocities of the entrained droplets in the range of $4\,m/s$ to $10\,m/s$. This suggests that the droplets are entrained almost perpendicularly to the flow axis and are then accelerated to the gas phase velocity. Due to the small droplet size and the correspondingly small inertia, the droplets should quickly reach an equilibrium state with the gas flow.

Liquid atomization due to entrainment is generally divided into two steps (Guildenbecher et al., 2009). During *primary atomization*, the bulk liquid disintegrates and droplets with an initial Sauter mean diameter $d_{32,1}$ are formed. *Secondary atomization* then describes the deformation and fragmentation of these droplets due to aerodynamic forces, yielding a final droplet diameter $d_{32,2}$.

Varga et al. (2003) found that the initial droplet diameter is proportional to the Rayleigh-Taylor wavelength and suggested

$$d_{32,1} \approx 0.2 \cdot \tilde{\lambda}_{RT} \quad . \tag{5.28}$$

The final fragment size distribution can then be determined based on the droplet Weber number *We* and the dimensionless initiation and total breakup time ($\hat{t}_{ini}$, $\hat{t}_{tot}$) (Hsiang and Faeth, 1992; Wert, 1995):

$$We_{d32,2} = 0.32 \left[We_{d32,1} \left(\hat{t}_{tot} - \hat{t}_{ini} \right) \right]^{2/3} \tag{5.29}$$

$$\hat{t}_{ini} = 1.6 \left(1 - Oh/7 \right)^{-1} \tag{5.30}$$

$$\hat{t}_{tot} = 5 \left(1 - Oh/7 \right)^{-1} \tag{5.31}$$

In eqs. (5.29) to (5.31), the Weber and Ohnesorge numbers are defined as

$$We = \rho_g \left(c_g - c_l \right)^2 d/\sigma \quad , \tag{5.32}$$

$$Oh = \mu_l \left/ \sqrt{\rho_l d_{32,1}\sigma} \right. \quad , \tag{5.33}$$

where μ is the dynamic viscosity [kg/(m s)].

5.4 TURBULENT TRANSFER ACROSS A SHEARED INTERFACE

There is little experimental data for the heat transfer at the interface of condensing jets. At first glance, experiments for annular condensing flow seem to be a viable alternative. However, while the geometrical configuration is indeed similar – a steam core surrounded by an annular liquid layer –, the underlying physical mechanism is different: In most experiments, the liquid annulus is formed due to steam condensation at the wall and is often dominated by gravitational effects. For this reason, it seems more appropriate to refer to experiments and models for stratified condensing flow. The geometric layout is somewhat different, but in most experiments the two phases are initially separated and thus independent of each other. While gravity may be of importance, it will be shown that interfacial transfer is mainly governed by the velocity difference between the two phases and the resulting shear stress.

5.4.1 Model approaches

Heat and mass transfer at fluid-fluid and fluid-solid boundaries is an important aspect of numerous technical applications and has therefore been the subject

of intensive research over many decades. Both heat and mass transfer can be treated analogously, the equivalent variables are given in table 5.1.

A widely used approach in modeling interfacial transfer mechanisms is by considering the fluid motion near the interface. This section provides a brief review of such concepts, following the comprehensive synopses by Banerjee (1990) and Gulawani et al. (2009).

Surface Renewal Model

In one of the earliest works that examined the local flow field to model interfacial mass transfer, Lewis and Whitman (1924) assumed a film of laminar fluid at the boundary. This assumption suggested a direct proportionality between the mass transfer coefficient β [m/s] and the mass diffusivity D [m²/s], i.e. $\beta \propto D$. However, experimental data indicated $\beta \propto D^{2/3}$ at fluid-solid boundaries and $\beta \propto D^{1/2}$ at fluid-fluid boundaries. This dependency could be better described by Higbie (1935), who assumed that turbulent eddies from the bulk flow replenish the laminar boundary layer in fixed intervals, yielding $\beta \propto D^{1/2}$. Danckwerts (1951) refined Higbie's model by introducing a random distribution of surface ages with a mean time between surface renewals t_{SR}, resulting in

$$\beta = \sqrt{D/t_{SR}} \quad . \tag{5.34}$$

Subsequently, two models were proposed to determine the surface renewal time: The *large eddy model* (Fortescue and Pearson, 1967) on the one hand, which assumed a renewal rate proportional to the turbulence characteristics of large eddies, and the *small eddy model* (Banerjee et al., 1968; Lamont and Scott, 1970) on the other hand, where the renewal rate was considered to be proportional to the turbulent energy dissipation rate. Theofanous et al. (1976) consolidated both concepts by showing that transfer is controlled by small eddies at high turbulence levels and by large eddies at low levels.

MASS TRANSFER		HEAT TRANSFER	
mass transfer coefficient	β	heat transfer coefficient	$\alpha/\rho c_p$
mass diffusivity	D	thermal diffusivity	$\kappa = \lambda/\rho c_p$
Schmidt number	$Sc = \nu/D$	Prandtl number	$Pr = \nu/\kappa$

Table 5.1: Equivalent quantities for heat and mass transfer

A criterion for the transition between the large and the small eddy model can be given by the turbulent Reynolds number based on appropriate turbulent velocity and length scales (c_t, l_t) and the kinematic viscosity v:

$$Re_t = \frac{c_t l_t}{v} \tag{5.35}$$

According to Banerjee (1990), large eddies are dominant for $Re_t = O(100)$ and small eddies for $Re_t = O(1000)$. Bankoff (1980) recommended $Re_t = 500$ as transition criterion, while Lakehal and Labois (2011) proposed a transition region for $3000 < Re_t < 15\,000$. There is, however, no consistent definition for the turbulent Reynolds number. In CFD approaches, c_t and l_t are generally assumed proportional to the scales in the turbulence model, e.g. the turbulent kinetic energy and its rate of dissipation (Lakehal and Labois, 2011). If this information is not available, the *shear velocity*

$$c_\tau = \sqrt{\tau_{if}/\rho_l} \tag{5.36}$$

is commonly used as turbulent velocity scale. For the length scale, macroscopic parameters are often used, e.g. the height of the liquid layer for smooth surfaces or the wave height for rough surfaces (Kirchner and Bankoff, 1985).

Gulawani et al. (2009) incorporated both the small and large eddy model into a CFD code and compared the simulation results with experimental data for steam jet DCC. Their results indicate that the small eddy model is best suited to model the interfacial heat transfer coefficient of steam jets.

Banerjee (1990) correlated the surface renewal time with the turbulence structure at wave-free gas-liquid and liquid-wall boundaries. His experiments showed that the turbulence structure at an interface changes with increasing shear stress:

- For low shear stress, "patches" are created at the interface as remnants of bulk turbulence. The patch area and residence time scale with wall shear velocity and mean flow velocity, thus both bulk and local properties are necessary to describe the turbulence structure.

- At high levels of shear stress, "streaks" form at the interface and break down into "bursts" (fig. 5.8). These patterns are similar for both fluid-fluid and fluid-solid boundaries, and the burst period scales with the viscosity v_l and the shear velocity c_τ. Accordingly, the turbulence structure is only dependent on local flow properties.

In the high shear regime, Banerjee determined the dimensionless mean time between bursts from experimental data as

$$\hat{t}_b = \frac{t_b c_\tau^2}{v_l} \cong 40 \text{ to } 85 \quad . \tag{5.37}$$

gas-liquid interface

wall
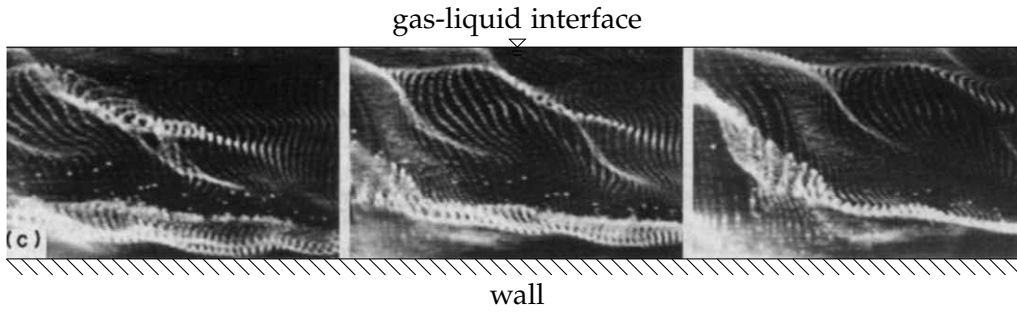
Figure 5.8: Generation of turbulent bursts near a cocurrently sheared gas-liquid interface, as observed by Rashidi et al. (1991) (bubble tracer visualization)
© 1991 Elsevier Ltd., reprinted with permission

By assuming $t_b = t_{SR}$, the transfer coefficient was then obtained from eq. (5.34):

$$\frac{\beta}{c_\tau} = \frac{1}{\sqrt{\hat{t}_b}} Sc^{-0.5} \tag{5.38}$$

Eddy Diffusivity Model

In parallel to the developments of the surface renewal model, Levich (1962) proposed the eddy diffusivity model that incorporated effects of both molecular and turbulent diffusivity. According to Henstock and Hanratty (1979), both models have similar implications if the parameters and assumptions are used consistently.

Surface Divergence Model

The velocity component normal to a rigid wall must always be zero to satisfy continuity. In contrast, the velocity field at free surfaces, e.g. between a gas and a liquid phase, can have a normal component. Banerjee pointed out that the most important component of the normal velocity near the free surface is related to the surface divergence, which in turn is caused by turbulent motion (Banerjee, 1990; Banerjee et al., 2004). Assuming homogeneous, isotropic turbulence, this leads to an equation for the transfer coefficient at a shear-free interface based on the turbulent Reynolds number:

$$\frac{\beta \, Sc^{0.5}}{c_t} = C \, Re_t^{-1/2} f(Re_t) \tag{5.39}$$

$$f(Re_t) = \left[0.3 \left(2.83 \, Re_t^{3/4} - 2.14 \, Re_t^{2/3} \right) \right]^{1/4} \tag{5.40}$$

Although derived for shear-free interfaces, this model could also predict DNS "experiments" for the mass transfer at a sheared air-water interface (Banerjee et al., 2004) and for direct contact condensation in a steam-water countercurrent stratified flow (Lakehal et al., 2008a,b). In general, these DNS results also confirm the assumptions underlying the surface renewal model (Banerjee et al., 2004; Lakehal et al., 2008a,b; Lakehal and Labois, 2011).

5.4.2 Turbulent heat transfer

The surface renewal model can be applied to heat transfer problems by using eq. (5.38) with the equivalent parameters for heat transfer, resulting in

$$\frac{\alpha_{if,l}}{\rho_l c_{p,l} c_\tau} = \frac{1}{\sqrt{\hat{t}_b}} Pr^{-0.5} \quad . \tag{5.41}$$

Here, $\alpha_{if,l}$ is the liquid-side heat transfer coefficient $[\mathrm{W}/(\mathrm{m}^2\,\mathrm{K})]$, $Pr = c_p \mu / \lambda$ is the Prandtl number and λ is the thermal conductivity $[\mathrm{W}/(\mathrm{m}\,\mathrm{K})]$. By introducing an appropriate turbulent length scale l_t, eq. (5.41) can be non-dimensionalized as

$$\underbrace{\frac{\alpha_{if,l} l_t}{\lambda}}_{=Nu_t} = \frac{1}{\sqrt{\hat{t}_b}} \cdot \underbrace{\frac{c_\tau l_t}{\nu}}_{Re_t} \underbrace{\left(\frac{c_p \mu}{\lambda}\right)^{0.5}}_{=Pr} \quad , \tag{5.42}$$

where Nu_t is the turbulent Nusselt number. Various authors have proposed correlations for the heat transfer in stratified steam-water flow which follow the functional form of eq. (5.42):

- Jensen (1982) derived an empirical model based on experiments in the horizontal cocurrent flow regime which distinguished between high and low liquid Reynolds numbers:

$$Nu_t = \begin{cases} 0.14 Re_t Pr_t^{0.5} & \text{(high liquid Reynolds numbers)} \\ 0.1 Re_t Pr_t^{0.5} & \text{(low liquid Reynolds numbers)} \end{cases} \tag{5.43}$$

- H. J. Kim et al. (1985) used a similar approach for nearly horizontal and nearly vertical countercurrent flow that included the impact of the channel inclination ϑ:

$$\begin{aligned} Nu_t &= C_1 Re_t^{C_2} Pr_t^{0.5} \\ C_1 &= 0.141 - 0.111 \left(\sin \vartheta\right)^{0.93} \\ C_2 &= 0.96 + 0.425 \left(\sin \vartheta\right)^{2.2} \end{aligned} \tag{5.44}$$

- Hughes and Duffey (1991) modeled the characteristics of homogeneous isotropic turbulence according to Prandtl's mixing length model, considering the influences of both interfacial and wall shear stress. This analytical approach resulted in

$$\alpha_{if,l} = \underbrace{\frac{2}{\sqrt{2\pi}}}_{\approx 0.8} \sqrt{\frac{\lambda_l c_{p,l}}{\nu_l}\left(\tau_w + \tau_{if}\right)} \quad . \tag{5.45}$$

- H. J. Kim and Bankoff (1983) pointed out that that the influence of surface waves is negligible in the smooth interface region (two-dimensional ripples, capillary waves), but becomes dominant in the rough interface region (three-dimensional waves, roll waves). This was taken into account by Murata et al. (1992), who included the surface renewal time due to Kelvin-Helmholtz waves $t_{\tilde{\lambda}}$ in addition to the time between interfacial and wall bursts ($t_{b,if}$, $t_{b,wall}$), which were modeled according to Banerjee (1990) (eq. (5.37) with $\hat{t}_b = 85$):

$$\alpha_{if,l} = \sqrt{\lambda_l \rho_l c_{p,l}\left(\frac{1}{t_{b,if}} + \frac{1}{t_{b,wall}} + \frac{1}{t_{\tilde{\lambda}}}\right)} \tag{5.46}$$

Their model required the wave height, which was estimated using a correlation by Bontozoglou and Hanratty (1989).

- Lakehal and Labois (2011) applied the surface divergence model (eq. (5.39)) to condensing flows:

$$\frac{\alpha}{\rho c_p c_\tau} = C_1 \cdot Pr^{0.5} Re_t^{C_2} \cdot f(Re_t) \tag{5.47}$$

$$C_1 = \begin{cases} 0.35 & Pr = 1 \\ 0.45 & Pr \gg 1 \end{cases} \quad C_2 = \begin{cases} -0.5 & Re_t \leq 3000 \text{ (large eddy regime)} \\ -0.25 & Re_t \geq 15\,000 \text{ (small eddy regime)} \end{cases}$$

The surface divergence function $f(Re_t)$ was determined according to eq. (5.40), and C_2 was linearly interpolated for $3000 < Re_t < 15\,000$.

The aforementioned approaches and some additional models are compared in table 5.2 and fig. 5.9.

For stratified flow with condensation, further correlations have been proposed based on global flow properties, e. g. by Bankoff (1980), H. J. Kim and Bankoff (1983), and H. J. Kim et al. (1985). These correlations, however, are based on globally averaged parameters of stratified flow, such as the Reynolds, Froude and Prandtl number and can therefore not be applied to other flow types such as condensing jets.

	FLOW REGIME[a]	$Nu_t\,Pr^{-0.5} = C_1\,Re_t^{C_2}\,f(Re_t)$			REMARKS[b]
		C_1	C_2	$f(Re_t)$	
Lakehal et al. (2008a)	INC, CC	0.079	1		$Pr \approx 1$
Jensen (1982)	H, C	0.10	1		low Re_l
		0.14	1		high Re_l
Murata et al. (1992)	H, C	0.11	1		$\tau_{if} \gg \tau_{wall}$, no waves
Hughes and Duffey (1991)	H, C	0.80	1		$\tau_{if} \gg \tau_{wall}$
H. J. Kim and Bankoff (1983)	INC, C	0.061	1.12		
H. J. Kim et al. (1985)	H, CC	0.14	0.96		
	V, C	0.25	0.535		
Lakehal and Labois (2011)	H, C	0.35	0.75	eq. (5.40)	$Pr \approx 1$, SE
			0.5		$Pr \approx 1$, LE

[a] H = horizontal, V = vertical, INC = inclined; C = cocurrent, CC = countercurrent
[b] SE/LE = small/large eddy regime

Table 5.2: Correlations for the turbulent Nusselt number $Nu_t = \alpha_{if} l_t / \lambda$ in stratified condensing steam-water flow based on the turbulent Reynolds number Re_t
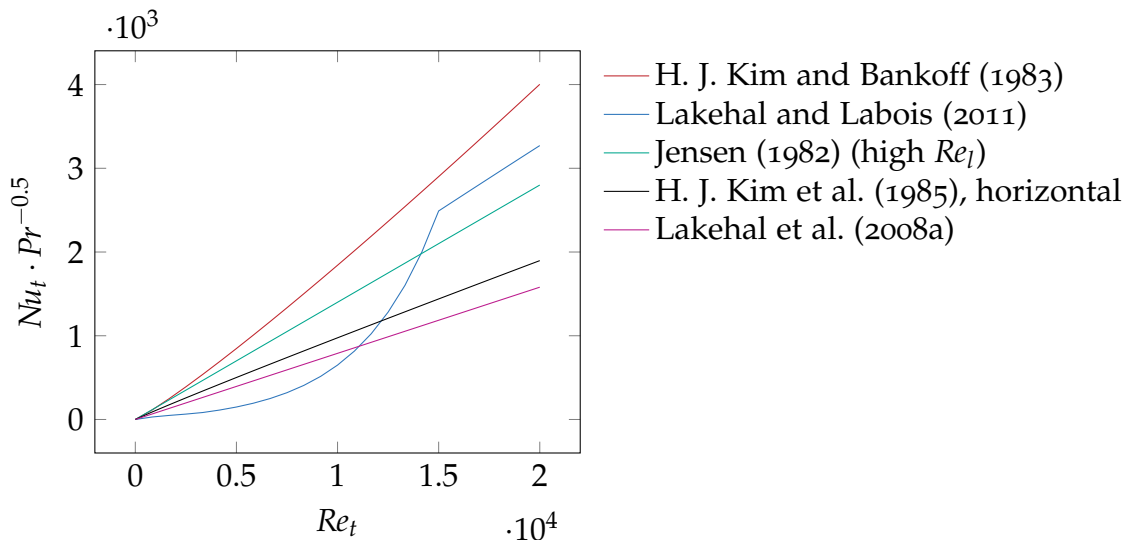
Figure 5.9: Turbulent Nusselt number Nu_t in stratified condensing flow as a function of the turbulent Reynolds number Re_t (cf. table 5.2)

5.4.3   Shear stress and interfacial friction factor

The shear stress due to the velocity difference at a gas-liquid interface can be
determined as

$$\tau_{if} = \tfrac{1}{4} f_{if} \cdot \tfrac{1}{2} \rho_g \left(c_g - c_l \right) \left| c_g - c_l \right| \tag{5.48}$$

Experiments have shown a linear relation between the interfacial friction factor
f_{if} in stratified flow and the Reynolds number of the liquid phase Re_l based on
the water layer thickness δ_l:

$$\tfrac{1}{4} f_{if} = C_1 \cdot Re_l + C_2 \tag{5.49}$$

$$Re_l = \rho_l c_l \delta_l / \mu_l \quad . \tag{5.50}$$

Values for the empirical constants C_1 and C_2 for different flow regimes are given
in table 5.3 and compared in fig. 5.10.

$\tfrac{1}{4} f_{if} = C_1 \cdot Re_l + C_2$	$C_1/10^{-6}$	C_2	FLOW REGIME
Paras et al. (1994)	3.7	0.022	air-water, cocurrent, horizontal, with atomization
H. J. Kim et al. (1985)	1.4	0.021	steam-water, countercurrent, nearly horizontal
H. J. Kim et al. (1985)	1.6	0.025	steam-water, countercurrent, nearly vertical
Linehan et al. (1969)	2.3	0.0131	air-water, cocurrent, horizontal

Table 5.3: Correlations for the interfacial friction factor f_{if} in stratified flow based on the water
Reynolds number Re_l
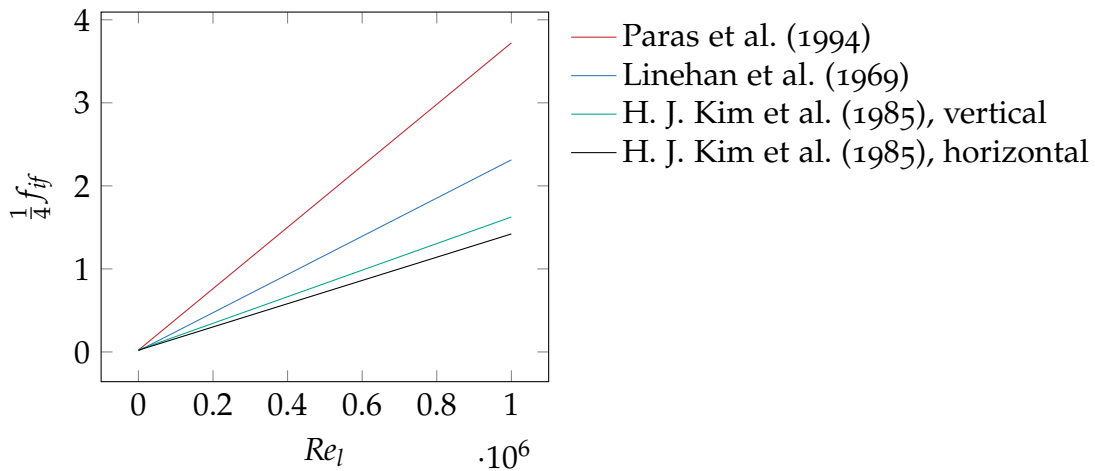
Figure 5.10: Interfacial friction factor f_{if} as a function of the water Reynolds number Re_l

5.5 THEORETICAL MODEL

Immediately after steam injection, the jet consists of a conical vapor core surrounded by the pool or channel water, similar to annular two-phase flow. However, the flow is by no means fully developed: Initially, there is a sharp radial velocity gradient at the boundary between the vapor core and the surrounding stagnant water. Waves are formed at this boundary and liquid ligaments are entrained into the gas core, rapidly breaking up into small droplets. These droplets will cause a quick deceleration of the gas phase due to their high inertia. At the same time, steam condenses upon the entrained droplets and at the two-phase jet boundary and the volume fraction ϵ_g decreases, finally resulting in a dispersed bubbly flow with negligible slip.

There exists little experimental data regarding the local flow structure of a turbulent condensing two-phase jet. Therefore, some simplifying assumptions have been made in the model development where necessary, in particular regarding the jet profile and the changes in the flow regime. In contrast, appropriate physical model accuracy has been sought regarding the dominant processes of water entrainment and steam condensation.

As shown in fig. 5.11, the proposed model divides the jet region into two areas: The two-phase jet with radius R_{2ph}, consisting of a gas phase g and a liquid phase l, and the surrounding annular water layer w (outer radius R_w), which may be initially stagnant (pool DCC) or in motion (channel DCC). The volume fraction of fluid i is thus defined as

$$\epsilon_i = \frac{A_i}{A} = \frac{A_i}{\pi R_w^2} \tag{5.51}$$

and consequently $\epsilon_w + \epsilon_l + \epsilon_g = 1$. Here, A is the total flow cross section and A_i the cross-section occupied by fluid i.

The two-phase jet flow is at first considered as a dispersed droplet flow, which turns into a dispersed bubbly flow at lower void fractions. The transition from droplet to bubbly flow is assumed at $\tilde{\epsilon}_g = 0.5$, with the *relative volume fraction* defined as

$$\tilde{\epsilon}_g = \frac{\epsilon_g}{\epsilon_l + \epsilon_g} \quad ; \quad \tilde{\epsilon}_l = 1 - \tilde{\epsilon}_g \quad . \tag{5.52}$$

Entrainment is modeled based on the Kelvin-Helmholtz and Rayleigh-Taylor instabilities, and is assumed to be perpendicular to the flow axis. Accordingly, the entrained mass is added to the two-phase jet without momentum in the axial direction. In the droplet flow regime, the diameter of entrained droplets

is obtained by taking into account both primary and secondary atomization and the surface renewal model is used for the heat and mass transfer at the two-phase jet boundary.
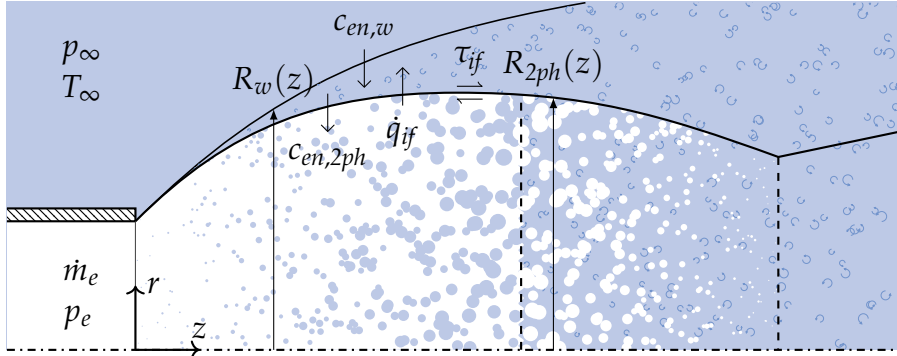
(a) Pool DCC: Stagnant, unconfined environment

R_w: jet radius, i.e. boundary between moving and stagnant water; $c_{en,w}$: water entrainment velocity based on the turbulent entrainment assumption; p_∞, T_∞: ambient pool pressure and temperature
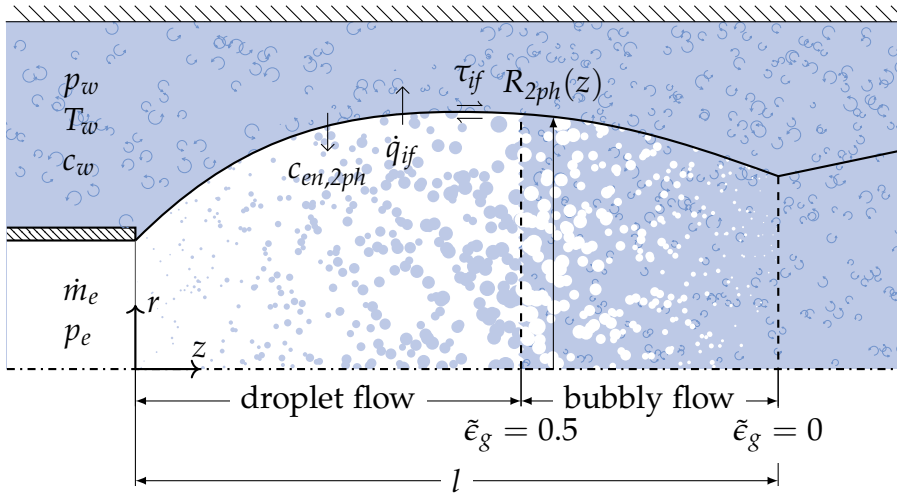
(b) Channel DCC: Moving, confined environment

p_w, T_w, c_w: pressure, temperature and velocity of surrounding water

Figure 5.11: The one-dimensional, two-phase DCC model is based on three fluids: The gas phase g and the liquid phase l in the two-phase flow region $2ph$, surrounded by an annular water layer w, which is initially either stagnant (pool DCC) or flowing (channel DCC).
l: two-phase jet length; R_{2ph}: two-phase jet radius; $\dot{m}_e$, p_e: steam nozzle exit mass flux and pressure; $\tilde{\epsilon}_g$: relative void fraction with respect to the two-phase region; $c_{en,2ph}$: entrainment velocity of droplets based on the Kelvin-Helmholtz and Rayleigh-Taylor instabilities; τ_{if}: shear stress at the two-phase jet interface; $\dot{q}_{if}$: interfacial heat flux according to the surface renewal theory

For channel DCC, the outer boundary of the surrounding water is given by the channel diameter ($2R_w = d_{channel}$). In pool DCC, the outer jet boundary grows due to turbulent entrainment of pool water into the jet. This boundary between the moving water layer and the stagnant pool is determined according to the entrainment assumption for two-phase jets.

5.5.1 Conservation equations

Traditionally, one-dimensional two-phase flow simulations are based on a *two-fluid model*, where each phase is represented by a separate fluid. In this study, the two-fluid model is augmented by introducing additional fluid groups. This *multi-fluid model* allows for the distinction of flow properties within a single phase, for instance between the moving water layer and the liquid droplets. The conservation equations for the mass, momentum and total enthalpy of these k fluids are derived from their general form (cf. Guelfi et al., 2007; Ishii and Hibiki, 2011; Oertel, 2012) based on the assumptions made in section 2.4.

Then, the mass conservation equation for fluid i has the form

$$\frac{\mathrm{d}}{\mathrm{d}z}\left(\epsilon_i \rho_i c_i A\right) = A \sum_{j=1}^{k} \Gamma_{j \to i} \quad , \tag{5.53}$$

where ρ and c are the density and velocity of the fluid i, respectively, and $\Gamma_{j \to i}$ is the *volumetric mass source term* [kg/(m^3 s)] due to exchange processes from fluid j to fluid i.

Introducing the local static pressure p, the momentum equation can be written as

$$\frac{\mathrm{d}}{\mathrm{d}z}\left(\epsilon_i \rho_i c_i^2 A\right) + \epsilon_i A \frac{\mathrm{d}p}{\mathrm{d}z} = A \sum_{j=1}^{k} \left(c_{if,ij}\Gamma_{j \to i} + M_{j \to i}\right) \quad , \tag{5.54}$$

Here, $M_{j \to i}$ is the *volume-specific total interfacial shear force* [kg/(m^2 s^2)] and accounts for the effects of particle drag and interfacial shear. The velocity at the interface between phase i and j $c_{if,ij}$ is determined by a donor formulation:

$$
\begin{aligned}
c_{if,ij} &= c_i ; \quad \Gamma_{j \to i} < 0 \\
c_{if,ij} &= c_j ; \quad \Gamma_{j \to i} > 0
\end{aligned}
\tag{5.55}
$$

This treatment is common practice in the numerical scheme development of one-dimensional system codes (e. g. RELAP5/MOD3) because it offers the most realistic treatment of the momentum exchange process (Carlson et al., 1995).

The energy conservation equation based on the total enthalpy is

$$
\frac{\mathrm{d}}{\mathrm{d}z} \left[\epsilon_i \rho_i c_i \left(h_i + 0.5 c_i^2 \right) A \right]
$$
$$
= A \sum_{j=1}^{k} \left[\Gamma_{j \to i} \left(h_{i,j} + c_{if,ij} c_i - 0.5 c_i^2 \right) + a_{if,ij} \dot{q}_{j \to i} + M_{j \to i} c_{if,ij} \right] \quad , \tag{5.56}
$$

where h is the specific enthalpy, $a_{if,ij}$ is the interfacial area density [m^2/m^3] of the interface between phase i and j, and $h_{i,j}$ and $\dot{q}_{j \to i}$ represent the specific enthalpy and the sensible heat flux [W/m^2] at the i-side of the phase interface between i and j, respectively.

The interfacial transfer conditions are given by

$$
\Gamma_{j \to i} + \Gamma_{i \to j} = 0 \quad , \tag{5.57}
$$
$$
M_{j \to i} + M_{i \to j} = 0 \quad , \tag{5.58}
$$
$$
\Gamma_{j \to i} h_{i,j} + a_{if,ij} \dot{q}_{j \to i} + \Gamma_{i \to j} h_{j,i} + a_{if,ij} \dot{q}_{i \to j} = 0 \quad . \tag{5.59}
$$

For pool DCC, the pressure is constant and equal to the ambient pressure p_∞, while the flow cross section $A(z) = \pi R_w^2$ is a function of the axial distance z. Conversely, the flow cross section is given for channel DCC, and the pressure $p(z)$ is an independent variable.

5.5.2 Interfacial area transport

In addition to the conservation equations, an interfacial area transport equation (Ishii and S. Kim, 2004) for the dispersed phase d is used to track the change of the interfacial area density a_{if} due to droplet entrainment, droplet growth and bubble condensation:

$$
\frac{1}{A} \frac{\mathrm{d}}{\mathrm{d}z} \left(a_{if,d} c_d A \right) = \Phi_d + \left(\frac{2}{3} \frac{a_{if,d}}{\rho_d} \left(\frac{\sum_{j=1}^{k} \Gamma_{j \to d}}{\epsilon_d} - c_d \frac{\mathrm{d}\rho_d}{\mathrm{d}z} \right) \right) \tag{5.60}
$$

Here, Φ_d is the *interfacial area source term* $[1/(\mathrm{m\,s})]$, which is equal to zero for bubbly flow. For droplet flow, the interfacial area source term due to droplet entrainment $\Phi_d = \Phi_{en}$ is calculated as

$$\Phi_{en} = \dot{n}_{en}\pi d_{20,en}^2 \cdot \frac{2\pi R_{2ph}}{A} \quad , \tag{5.61}$$

with the particle flux $[1/(\mathrm{m^2\,s})]$ of entrained droplets across the two-phase jet boundary

$$\dot{n}_{en} = \frac{c_{en,2ph}}{\frac{\pi}{6}d_{30,en}^3} \quad . \tag{5.62}$$

In eqs. (5.61) and (5.62), d_{20} and d_{30} are the surface and volume mean diameters, respectively. Using $d_{32} = d_{30}^3/d_{20}^2$, eqs. (5.61) and (5.62) can be combined as

$$\Phi_{en} = \frac{12\pi R_{2ph}}{A}\frac{c_{en}}{d_{32,en}} \quad . \tag{5.63}$$

In eq. (5.63), the Sauter mean diameter of entrained droplets $d_{32,en}$ is the diameter after secondary atomization $d_{32,2}$ according to eqs. (5.29) and (5.32).

5.5.3 Turbulent entrainment

In the droplet flow regime, i. e. close to the nozzle exit, it is postulated that the entrainment model by Varga et al. (2003) (section 5.3.1) is applicable. This implies that the flow structure at the interface of a gas jet in a liquid pool is comparable to a liquid jet surrounded by high-speed gas stream and that the primary instability is proportional to the vorticity layer thickness in the gas stream. Entrainment is thus governed by the secondary Rayleigh-Taylor instability between the ambient water and the continuous gas phase of the jet, and it is assumed that the entrainment velocity can be determined in analogy to the Kelvin-Helmholtz instability as

$$c_{en,RT} = \frac{E_{0,RT}}{2\pi} \cdot \tilde{\lambda}_{RT}\omega_{RT} \quad . \tag{5.64}$$

The value of the entrainment coefficient $E_{0,RT}$ is obtained based on a parametric study (cf. section 5.7.1).

In the bubbly flow regime and in the single-phase turbulent jet region, entrainment is determined according to the extension of the "classical" turbulent entrainment assumption by Ricou and Spalding (1961), eq. (5.15):

$$c_{en} = E_0\sqrt{\rho_m/\rho_\infty}\,c_m \quad . \tag{5.15 revisited}$$

The mean density ρ_m and velocity c_m are calculated as

$$\rho_m = \frac{\epsilon_g \rho_g + \epsilon_l \rho_l}{\epsilon_l + \epsilon_g} \quad , \tag{5.65}$$

$$c_m^2 = \frac{\epsilon_g \rho_g c_g^2 + \epsilon_l \rho_l c_l^2}{\epsilon_l \rho_l + \epsilon_g \rho_g} \quad . \tag{5.66}$$

The rationale for this approach is as follows: The entrainment velocity in eq. (5.15) scales as $\sqrt{\rho_m c_m^2}$, i. e. the square root of the jet momentum flux. By defining c_m according to eq. (5.66), the common definition of the mean density eq. (5.65) can be used while maintaining $c_{en} \propto \sqrt{\rho_m c_m^2}$.

In their model development for submerged gas jets, Vivaldi et al. (2013) assumed droplet flow inside the jet for a relative void fraction larger than $\tilde{\epsilon}_{g,drp} = 0.8$ and bubbly flow below $\tilde{\epsilon}_{g,bbl} = 0.5$. In the transition region $\tilde{\epsilon}_{g,drp} > \tilde{\epsilon}_g > \tilde{\epsilon}_{g,bbl}$, a weighted logarithmic average was used. This approach is adopted in the present model, and the entrainment velocity for the two-phase jet is thus obtained as

$$c_{en,2ph} = \exp\left[\frac{\tilde{\epsilon}_g^* - \tilde{\epsilon}_{g,bbl}}{\tilde{\epsilon}_{g,drp} - \tilde{\epsilon}_{g,bbl}} \ln\left(c_{en,RT}\right) + \frac{\tilde{\epsilon}_{g,drp} - \tilde{\epsilon}_g^*}{\tilde{\epsilon}_{g,drp} - \tilde{\epsilon}_{g,bbl}} \ln\left(c_{en}\right) \right] \quad , \tag{5.67}$$

$$\tilde{\epsilon}_g^* = \max\left[\tilde{\epsilon}_{g,bbl} \, , \, \min\left(\tilde{\epsilon}_g, \tilde{\epsilon}_{g,drp}\right) \right] \quad . \tag{5.68}$$

For pool DCC, the "global" entrainment, i. e. the entrainment velocity of stagnant fluid into the jet $c_{en,w}$ is given by eq. (5.15) with

$$\rho_m = \sum_{i=g,l,w} \epsilon_i \rho_i \quad , \tag{5.69}$$

$$c_m^2 = \frac{\sum_{i=g,l,w} \epsilon_i \rho_i c_i^2}{\sum_{i=g,l,w} \epsilon_i \rho_i} \quad . \tag{5.70}$$

Using eqs. (5.15) and (5.67) with appropriate entrainment coefficients allows to calculate the volumetric mass source terms due to entrainment:

$$\Gamma_{en,w \to l} = \rho_w c_{en,2ph} \, 2\pi R_{2ph} \big/ A \tag{5.71}$$

$$\Gamma_{en,\infty \to w} = \rho_\infty c_{en,w} \, 2\pi R_w \big/ A \tag{5.72}$$

5.5.4 Interfacial shear force

Interfacial drag

The interfacial drag between a continuous phase c and a dispersed phase d is given as (Ishii and Mishima, 1984)

$$M_{c \to d} = -\frac{3}{8} \frac{C_D}{r_D} \epsilon_d \rho_c |c_d - c_c| (c_d - c_c) \quad , \tag{5.73}$$

where the drag coefficient C_D is determined based on the drag Reynolds number Re_D using the mixture dynamic viscosity μ_m:

$$C_D = 24 \left(1 + 0.1 \, Re_D^{0.75}\right) \Big/ Re_D \tag{5.74}$$

$$Re_D = 2 \, r_D \rho_c |c_d - c_c| / \mu_m \tag{5.75}$$

$$\mu_m = \begin{cases} \mu_c \left(1 - \tilde{\epsilon}_d\right)^{-1} & \text{(bubbly flow)} \\ \mu_c \left(1 - \tilde{\epsilon}_d\right)^{-2.5} & \text{(droplet flow)} \end{cases} \tag{5.76}$$

Assuming spherical particles, the drag radius can be calculated as $r_D = d_{32}/2$.

Interfacial shear

In the droplet flow regime, the interfacial shear between the gas phase g and the surrounding water w is calculated as (Ishii and Mishima, 1984)

$$M_{g \to w} = -\tau_{if} \cdot 2\pi R_{2ph} \Big/ A \quad , \tag{5.77}$$

$$\tau_{if} = \tfrac{1}{4} f_{if} \cdot \tfrac{1}{2} \rho_g \left(c_g - c_w\right) \left|c_g - c_w\right| \quad . \tag{5.78}$$

According to Hanratty (1991), accounting for the presence of droplets in the gas phase by using a mean density in eq. (5.78) produces unrealistic results. He suggests that the increase in interfacial shear stress due to droplet deposition is counterbalanced by the dampening effect of droplets on turbulence. For this reason, the gas phase density and velocity are used in eq. (5.78).

In stratified flow, the interfacial friction factor f_{if} is a function of the liquid-side Reynolds number based on the thickness of the liquid layer, as explained in section 5.4.3:

$$f_{if} = C_1 \cdot Re_w + C_2 \tag{5.49 revisited}$$

$$Re_w = \delta_w \cdot \rho_w c_w / \mu_w \tag{5.50 revisited}$$

In order to apply this relation to channel DCC, a length scale equivalent to the water layer thickness is required. For the stratified flow of a gas phase g and a liquid phase w (liquid layer thickness δ_w) in a rectangular channel (width W), the liquid-phase hydraulic diameter based on the wetted perimeter between liquid and gas is defined as:

$$d_{H,if,w} = \frac{4A_w}{W} = \frac{4W\delta_w}{W} = 4\delta_w$$

The equivalent scale for DCC in a circular pipe with radius R_w is:

$$d_{H,if,w} = \frac{4\pi\left(R_w^2 - R_{2ph}^2\right)}{2\pi R_{2ph}} = \frac{2\left(R_w^2 - R_{2ph}^2\right)}{R_{2ph}} \tag{5.79}$$

Accordingly, it is suggested to define the Reynolds number for interfacial shear in channel DCC as

$$Re_w = \tfrac{1}{4}d_{H,if,w} \cdot \rho_w c_w / \mu_w \quad , \tag{5.80}$$

using the water-gas hydraulic diameter $d_{H,if,w}$ according to eq. (5.79). The interfacial friction factor is then determined using the correlation by Paras et al. (1994) for stratified-atomization flow:

$$\tfrac{1}{4}f_{if} = 3.77 \times 10^{-6} \cdot Re_w + 0.022 \tag{5.81}$$

For pool DCC, i.e. for the absence of liquid-side turbulence, the interfacial friction factor at the jet boundary is calculated in analogy to the wall friction in two-phase flow. Y. Xu et al. (2012) performed a comprehensive evaluation of existing correlations and recommended the correlation by Fang et al. (2011):

$$f_{if} = 0.25 \left[\log\left(150.39\, Re_{gw}^{-0.98865} - 152.66\, Re_{gw}^{-1}\right)\right]^{-2} \quad ; \quad 3000 \leq Re \leq 10^8 \tag{5.82}$$

This correlation is a more accurate representation of the Nikuradse/Moody diagram (Moody, 1944; Nikuradse, 1933) than the widely used Blasius equation, particularly for high Reynolds numbers. The relative Reynolds number between the gas phase and the surrounding water is defined as

$$Re_{gw} = \rho_g \left|c_g - c_w\right| d_{H,if,g} \Big/ \mu_g \tag{5.83}$$

based on the hydraulic diameter of the gas phase:

$$d_{H,if,g} = \frac{4\pi R_{2ph}^2 \tilde{\epsilon}_g}{2\pi R_{2ph}} = 2R_{2ph}\tilde{\epsilon}_g \tag{5.84}$$

Wall shear

For channel DCC, the wall shear is calculated as

$$M_{w \to wall} = -\tau_{wall} \cdot 2\pi R_w / A \quad , \tag{5.85}$$

$$\tau_{wall} = \tfrac{1}{4} f_{wall} \cdot \tfrac{1}{2} \rho_w (c_w)|c_w| \quad , \tag{5.86}$$

and the wall friction factor f_{wall} is given by eq. (5.82) using

$$Re_w = \rho_w |c_w| d_{H,wall,w} / \mu_w \quad , \tag{5.87}$$

$$d_{H,wall,w} = 2R_w \epsilon_w \quad . \tag{5.88}$$

5.5.5   Interfacial heat and mass transfer

Interfacial heat and mass transfer is modeled with the two-resistance model for the phase change in pure substances. This approach considers the heat transfer processes on each side of the phase interface, where the total heat flux $\dot{q}_{tot}$ can be written as

$$\dot{q}_{tot,g \to l} = \dot{q}_{g \to l} + \dot{m}_{g \to l} h_{l,if} = \alpha_l (T_{sat} - T_l) + \dot{m}_{g \to l} h_{l,if} \quad , \tag{5.89}$$

$$\dot{q}_{tot,l \to g} = \dot{q}_{l \to g} - \dot{m}_{g \to l} h_{g,if} = \alpha_g \left(T_{sat} - T_g \right) - \dot{m}_{g \to l} h_{g,if} \quad . \tag{5.90}$$

T_{sat}, T_l and T_g are the saturation temperature and the temperature of the liquid and gas phase, respectively, and $\dot{m}_{g \to l}$ is the mass flux [kg/(m^2 s)] from the gas to the liquid phase.

Then, the mass flux can be determined from the total heat flux balance ($\dot{q}_{tot,l \to g} + \dot{q}_{tot,g \to l} = 0$) as

$$\dot{m}_{g \to l} = \frac{\alpha_l (T_{sat} - T_l) + \alpha_g \left(T_{sat} - T_g \right)}{h_{g,if} - h_{l,if}} \quad , \tag{5.91}$$

provided that the heat transfer coefficients α_l and α_g are known (see below).

Finally, the volumetric mass source term is obtained as

$$\Gamma_l = a_{if} \cdot \dot{m}_{g \to l} \quad . \tag{5.92}$$

The equivalent equations for the mass flux at the jet interface $\dot{m}_{g \to w}$ are obtained by replacing the index l with w in eqs. (5.89) to (5.91), the volumetric mass source term is determined by

$$\Gamma_w = \frac{2\pi R_{2ph}}{A} \cdot \dot{m}_{g \to w} \quad . \tag{5.93}$$

Heat transfer coefficients at the dispersed interface

The heat transfer coefficient in the continuous phase α_c (α_g in the droplet flow regime, α_l in the bubbly flow regime) is given by the Nusselt number Nu:

$$\alpha_c = \lambda_c \, Nu_c \, / d_d \tag{5.94}$$

The Nusselt number for $0 \leq Pr_c \leq 250$ is calculated according to Hughmark (1967):

$$Nu_c = \begin{cases} 2 + 0.6 \, Re_{dc}^{0.5} \, Pr_c^{0.33} & ; \quad 0 \leq Re_{dc} < 776.06 \\ 2 + 0.27 \, Re_{dc}^{0.62} \, Pr_c^{0.33} & ; \quad 776.06 \leq Re_{dc} \end{cases} \tag{5.95}$$

In eq. (5.95), the relative Reynolds number between the dispersed and the continuous phase is defined as

$$Re_{dc} = \rho_c |c_d - c_c| \, d_d / \mu_c \quad . \tag{5.96}$$

Direct contact condensation of saturated steam in subcooled water is liquid-side limited, i. e. the prevailing heat transfer resistance is in the liquid phase. This implies that the continuous phase is dominant for bubbly flow, but condensation is initially governed by the heat conduction inside the droplet (dispersed phase), which in turn depends on the instationary temperature field $T(r, t)$ inside the droplet:

$$\frac{\partial T}{\partial t} = \kappa \left(\frac{\partial^2 T}{\partial r^2} + \frac{2}{r} \frac{\partial T}{\partial r} \right)$$

The solution of this partial differential equation is common practice for atomizing devices, where droplets are created with a fairly uniform size at a single location and the droplet age is a function of the distance from the injector (Celata et al., 1991). In condensing steam jets, however, droplets with varying sizes are constantly entrained into the jet and there is no common time scale. For this reason, a spatially uniform temperature is assumed inside the entrained droplets and heat transfer is determined based on an average heat transfer coefficient.

Weinberg (1952) measured the heat transfer coefficient during DCC of steam on droplets produced by a spray nozzle. He found that the value varied between $10^4 \, \text{W}/(\text{m}^2 \, \text{K})$ and $1.8 \times 10^4 \, \text{W}/(\text{m}^2 \, \text{K})$, but could not identify any statistical trends and thus recommends a mean value of $\alpha_l = 1.4 \times 10^4 \, \text{W}/(\text{m}^2 \, \text{K})$. As will be shown in section 5.7.1, a parametric study indicated that a value of $\alpha_l = 10^4 \, \text{W}/(\text{m}^2 \, \text{K})$ showed best agreement with experimental data.

Brucker and Sparrow (1977) experimentally determined the heat transfer coefficient in condensing vapor bubbles. They concluded that the value varies little

with pressure level and temperature difference and recommend a constant mean value of $\alpha_g = 10^4\,\mathrm{W/(m^2\,K)}$. Thus, the dispersed-side heat transfer coefficient for both droplet and bubbly flow is taken as

$$\alpha_d = 10^4\,\frac{\mathrm{W}}{\mathrm{m^2\,K}} \quad . \tag{5.97}$$

Heat transfer coefficients at the jet interface

The heat transfer coefficient at the liquid side of the jet interface is modeled in analogy to stratified flow (cf. table 5.2), where most researchers assumed a functional form

$$Nu_t \cdot Pr^{-0.5} = C_1 \cdot Re_t^{C_2} \quad . \tag{5.98}$$

The exponent for the turbulent Reynolds number in eq. (5.98) is in the order of unity, assuming $C_2 = 1$ eliminates the dependency on the turbulent length scale, thus

$$\frac{\alpha_{if,w}}{\rho_l c_{p,w} c_\tau} = \underbrace{\frac{1}{\sqrt{\hat{t}_b}}}_{=C_1}\, Pr^{-0.5} \quad . \tag{5.41 revisited}$$

Due to the high steam velocity, interfacial shear stress in channel DCC is much larger than wall shear stress ($\tau_{if} \gg \tau_{wall}$). Nevertheless, both are taken into account, giving

$$\alpha_{if,w} = \frac{1}{\sqrt{\hat{t}_b}}\sqrt{\frac{\lambda_w c_{p,w}}{\nu_w}\left(\tau_{wall} + \tau_{if}\right)} \quad . \tag{5.99}$$

Suggested values for C_1 range between 0.079 and 0.8 (cf. table 5.2), equivalent to dimensionless renewal rates $\hat{t}_b$ between 160 and 1.6. In the present work, $\hat{t}_b = 10$ was chosen based on a parametric study (cf. section 5.7.2).

The influence of the gas side heat transfer coefficient is largely negligible, as the steam temperature is close to saturation during steam jet DCC. An upper limit is given by molecular gas dynamics (Aya and Nariai, 1991):

$$\alpha_{if,g} = \frac{2C_{co}}{(2 - 0.798C_{co})}\frac{h_{lg}^2}{\sqrt{2\pi R_s T_g}}\frac{\rho_g}{T_g} \tag{5.100}$$

A condensation coefficient of $C_{co} = 1$ is used according to Aya and Nariai. For atmospheric steam, this gives $\alpha_{if,g} \approx 13.1 \times 10^6\,\mathrm{W/(m^2\,K)}$.

5.5.6 Qualitative implications of the chosen model approach

In the proposed model approach, condensation (and thus steam jet length) is based on two mechanisms: Entrainment and subsequent droplet condensation on the one hand, and condensation at the jet interface on the other hand. These two condensation mechanisms require specification of three parameters that are unknown a priori: The entrainment coefficient for droplet flow $E_{0,RT}$, the droplet heat transfer coefficient α_l and the dimensionless surface renewal time $\hat{t}_b$. In specifying these parameters, a superposition of the two condensation mechanisms is achieved. For high values of $E_{0,RT}$, entrainment becomes dominant and the dependency of the jet length on the mass flux is reproduced well, while the influence of condensation at the jet interface decreases, thus diminishing the dependency of the jet length on the water Reynolds number. A high value for $\hat{t}_b$ has the opposite effect. Consequently, a balance between both mechanism has to be found in order to account for both the influence of the steam mass flux and the water Reynolds number.

The value of $\hat{t}_b$ has little effect on the plume length in pool DCC. Therefore, the three parameters are determined by two subsequent parametric studies: First, $E_{0,RT}$ and α_l are varied to assess their impact on pool DCC (section 5.7.1). Based on these results, $\hat{t}_b$ is varied and the results are compared to experimental data for channel DCC (section 5.7.2).

5.6 SIMULATION MODEL

For a setup consisting of k different fluids, the conservation equations (eqs. (5.53), (5.54) and (5.56)) constitute a system of $3k$ ODEs. This system can be solved numerically, for instance using a Runge-Kutta algorithm, if sufficient closure relations are provided.

The interfacial closure relations (i. e. volumetric mass source term Γ, volume-specific total interfacial shear force M and sensible heat flux $\dot{q}$) have been derived in the previous section. If these are known, the system contains $4k + 2$ unknown variables (ϵ_k, ρ_k, h_k, c_k, p, A), thus $k + 2$ additional relations are required:

1. The thermodynamic state of each fluid i is determined by the two independent state variables p and h. Then, the density ρ can be expressed as a function of p and h and its axial derivative is given as

$$\frac{\mathrm{d}\rho_i}{\mathrm{d}z} = \left.\frac{\partial\rho_i}{\partial p}\right|_{h_i} \frac{\mathrm{d}p}{\mathrm{d}z} + \left.\frac{\partial\rho_i}{\partial h_i}\right|_{p} \frac{\mathrm{d}h_i}{\mathrm{d}z} \quad . \tag{5.101}$$

2. The definition of the volume fraction $\epsilon_i = A_i/A$ requires

$$\sum_{i=1}^{k} \epsilon_i = 1 \quad \Leftrightarrow \quad \sum_{i=1}^{k} \frac{\mathrm{d}\epsilon_i}{\mathrm{d}z} = 0 \quad . \tag{5.102}$$

3. a) In a confined environment, the flow cross-section $A(z)$ is given while the local pressure $p(z)$ is unknown.

   b) Conversely, in a free environment, $A(z)$ is unknown, but a constant static pressure $p(z) = p$ can be assumed.

Using above closure relations, the ODE system is solved numerically using the explicit fourth-order Runge-Kutta-Fehlberg algorithm (Fehlberg, 1969), as implemented in the GSL (Gough, 2009). The routine solves the n-dimensional first-order system

$$\frac{\mathrm{d}y_i(z)}{\mathrm{d}z} = f_i\big(z, y_1(z), \ldots y_n(z)\big)$$

marching in z-direction, where y_i are the n independent variables $c_{1\ldots k}$, $h_{1\ldots k}$, $\epsilon_{1\ldots k-1}$, and either A or p. The functions f_i for determining the derivatives are obtained from eqs. (5.53), (5.54) and (5.56)[2]. The algorithm uses an adaptive step size control based on a fifth-order error estimator which will keep the local error on each step within a predefined absolute and relative error with respect to the solution $y_i(z)$.

The interfacial area transport equation (eq. (5.60)) can be solved in the same manner[3] to determine the interfacial area density for the dispersed phase.

---

2 see appendix B.3.1, eqs. (B.12) to (B.15) for pool DCC and eqs. (B.21) to (B.24) for channel DCC

3 see appendix B.3.1, eq. (B.19) for pool DCC and eq. (B.28) for channel DCC

5.6.1 Boundary conditions

The ambient conditions (p_∞, h_∞) for pool DCC and the water inlet conditions (p_w, h_w, c_w, ϵ_w) for channel DCC are set according to the values in the particular experiment to be simulated. For pool DCC, the initial enthalpy of the annular water layer is given as $h_w(z{=}0) = h_\infty$. The physically correct approach for the initial velocity and volume fraction would be $c_w(z{=}0) = 0$ and $\epsilon_w(z{=}0) = 0$, i.e. assuming an infinitesimally small, stagnant water layer. Instead, $c_w(z{=}0) = 10^{-3} \cdot c_g(z{=}0)$ and $\epsilon_w(z{=}0) = 10^{-3}$ is used in order to improve numerical robustness. This alters the mass and momentum balance by 0.1 % and 0.0001 %, respectively, which is deemed to be acceptable.

At the steam nozzle exit, gas dynamic phenomena due to over- and underexpansion are neglected and the effective-adapted-jet approximation is applied as boundary condition. This approach is widely used in treating two-phase jets with and without condensation (Loth and Faeth, 1989) and assumes isentropic adaptation from the nozzle exit pressure p_e to the ambient pressure p_∞ (pool DCC) or p_w (channel DCC). The nozzle exit diameter is then replaced by an equivalent diameter based on the adapted flow conditions. Details on this procedure are given in appendix B.4.

The adapted exit velocity, density and the equivalent exit diameter are used as initial values $R_{2ph}(z{=}0)$, $c_g(z{=}0)$, $c_l(z{=}0)$, $\epsilon_g(z{=}0)$, $h_g(z{=}0)$, $h_l(z{=}0)$. A maximum void fraction of $\tilde{\epsilon}_g(z{=}0) = 1 - 10^{-8}$ and a minimum slip of $c_g/c_l = 1.001$ are enforced to avoid numerical errors due to division by zero. For the same reason, the initial temperatures of the liquid and gas phase are restricted to be slightly below ($T_l \leq T_{sat} - 10^{-8}$ K) or above ($T_g \geq T_{sat} + 10^{-8}$ K) the saturation temperature.

As discussed in chapter 3, the flow at the steam nozzle exit normally consists of a continuous gas phase and dispersed droplets with diameters in the order of one hundred nanometers. These droplets are in equilibrium with the gas phase and therefore do not contribute to the condensation process of the steam jet. However, their mass fraction has to be properly accounted for.

It can be safely assumed that the nanodroplets created by spontaneous condensation will be at least one order of magnitude smaller than the subcooled droplets which are subsequently entrained into the steam jet and have diameters in the range of few micrometers. Consequently, it is postulated that the nanodroplets will quickly coalesce with the entrained droplets and the initial value for the interfacial area density is obtained based on the initial liquid volume fraction and

the initial diameter of entrained droplets according to step 3 in the following paragraph:

$$a_{if}(z=0) = \frac{6\epsilon_l}{d_{32,en}}\bigg|_{z=0} \tag{5.103}$$

5.6.2 Solution procedure

Once the boundary conditions have been set, each solver step consists of the following major sub-steps:

1. Thermodynamic properties are determined using the IAPWS-IF97 equation of state (Wagner et al., 2000) as a function of the pressure $p(z)$ and the gas and liquid phase enthalpies h_g, h_l and h_w.

2. The entrainment velocity into the two-phase jet $c_{en,2ph}$ is calculated using eq. (5.67) with an entrainment coefficient of $E_{0,RT} = 0.16$ (droplet flow) and $E_0 = 0.08$ (bubbly flow), and the volumetric mass source term $\Gamma_{en,w\to l}$ is calculated according to eq. (5.71). For pool DCC, the entrainment of stagnant water ($c_{en,w}$, $\Gamma_{en,\infty\to w}$) is additionally obtained according to eqs. (5.15) and (5.72).

3. For droplet flow, eqs. (5.28) to (5.31) are solved to obtain the mean diameter of entrained droplets $d_{32,en}$ based on eq. (5.32), which is then used to calculate the interfacial area source term due to droplet entrainment Φ_{en} according to eq. (5.63).

4. Dispersed interfacial heat and mass transfer ($\dot{q}_{g\to l}$, $\dot{q}_{l\to g}$, $\dot{m}_{g\to l}$, Γ_l) is solved using eqs. (5.89) to (5.92) with interfacial heat transfer coefficients α_l, α_g according to eqs. (5.94) to (5.96).

5. Interfacial droplet/bubble drag ($M_{c\to d}$) is determined with eqs. (5.73) to (5.76), shear stress at the jet interface (τ_{if}, $M_{g\to w}$) with eqs. (5.77) and (5.78) based on the interfacial friction factor f_{if} according to eq. (5.82) (pool DCC) or eq. (5.81) (channel DCC).

6. For channel DCC, the wall shear (τ_{wall}, $M_{w\to wall}$) is calculated using eqs. (5.85) to (5.88). For pool DCC, $\tau_{wall} = 0$.

7. Heat and mass transfer at the jet interface ($\dot{q}_{g\to w}$, $\dot{q}_{w\to g}$, $\dot{m}_{g\to w}$, Γ_w) is given by eqs. (5.89) to (5.91) and (5.93) with interfacial heat transfer coefficients $\alpha_{if,w}$, $\alpha_{if,g}$ according to eqs. (5.99) and (5.100).

8. The Runge-Kutta-Fehlberg algorithm is invoked to determine the values of the independent variables $y_i(z + \Delta z)$ for the next step. If necessary, the step size Δz is decreased until both absolute and relative error are below the specified value of 10^{-8}.

Initially, the solver is invoked for dispersed droplet flow (liquid phase l = dispersed phase d). The solver proceeds until $\tilde{\varepsilon}_g = 0.5$ is reached, where the solver is re-initialized for dispersed bubbly flow (gas phase g = dispersed phase d) and continues until a minimum relative void fraction of $\tilde{\varepsilon}_g = 10^{-6}$ is reached. The axial distance at this point corresponds to the predicted penetration length: $z(\tilde{\varepsilon}_g = 10^{-6}) = l$.

5.7 VALIDATION

5.7.1 Pool DCC

The simulation model has been compared to various experiments taken from the literature (H. Y. Kim et al., 2001; Y.-S. Kim and Youn, 2008; Wu et al., 2009a, 2010a,b, 2007), which cover a wide range of parameters (nozzle exit diameter, mass flux and pressure, pool water temperature). Details on the selected experiments are given in table 5.4. For the simulation, initially saturated steam was assumed for all experiments ($x_{g,0} = 1$).

The stagnation state has been determined using the stagnation pressure p_0 provided in the literature while assuming a saturated steam state. Non-equilibrium effects during expansion (cf. chapter 3) have been neglected, as not all literature sources provided sufficient information about the nozzle geometry. Accordingly, the nozzle exit state has been determined assuming isentropic equilibrium expansion (cf. appendix B.2). The simulated exit conditions obtained in this way are given in table 5.5 and are in good agreement with the experimental data.

Parametric study: Determination of $E_{0,RT}$ and α_l

Due to the uncertainty concerning the value of the entrainment coefficient for droplet flow $E_{0,RT}$ and the droplet heat transfer coefficient α_l, a parametric study has been performed to assess their impact. For this purpose, the root

mean square deviation Δ_{RMS} of the predicted penetration length L_{calc} from the experimental value L_{exp} was used:

$$\Delta(L) = \left| \frac{L_{calc} - L_{exp}}{L_{exp}} \right| \tag{5.104}$$

$$\Delta_{RMS}(L) = \sqrt{\frac{1}{n} \sum_{i=1}^{n} \Delta(L_i)^2} \quad . \tag{5.105}$$

The results based on $n = 154$ experimental data sets are listed in table 5.6 and indicate that best agreement with experimental data ($\Delta_{RMS}(L) = 24\,\%$) is achieved with $E_{0,RT} = 0.16$ and $\alpha_l = 10^4\,\mathrm{W}/(\mathrm{m}^2\,\mathrm{K})$.

	STAGNATION STATE		
	pressure p_0/bar	temperature $T_0/°\mathrm{C}$	quality $x_{g,0}$
H. Y. Kim et al. (2001)	$1.90 - 7.20$		> 0.99
Wu et al. (2007), nozzle A	$2 - 5$		≈ 1
Wu et al. (2007), nozzle B	$2 - 5$		≈ 1
Wu et al. (2009a)	$2 - 6$		
Wu et al. (2010a)	$3 - 5$		
Wu et al. (2010b)	$4 - 6$		1
Y.-S. Kim and Youn (2008)		166	1

(a) Stagnation state (as stated in the literature)

	NOZZLE EXIT STATE			
	Mach no. Ma_e	mass flux $\dot{m}_e/\mathrm{kg}/(\mathrm{m}^2\,\mathrm{s})$	pressure p_e/bar	quality $x_{g,e}$
H. Y. Kim et al. (2001)	1	$284 - 1036$	$0.96 - 3.65$	$0.956 - 0.963$
Wu et al. (2007), nozzle A	1.35	$247 - 601$	$0.60 - 1.50$	$0.931 - 0.937$
Wu et al. (2007), nozzle B	1.89	$133 - 323$	$0.22 - 0.55$	$0.885 - 0.893$
Wu et al. (2009a)	1	$299 - 868$	$1.01 - 3.04$	$0.957 - 0.962$
Wu et al. (2010a)	1.79	$226 - 371$	$0.40 - 0.67$	$0.893 - 0.898$
Wu et al. (2010b)	1	$585 - 868$	$2.03 - 3.04$	$0.957 - 0.959$
Y.-S. Kim and Youn (2008)	1	1033	3.64	0.956

(b) Nozzle exit state (calculated)

Table 5.4: Parameters of selected DCC experiments taken from the literature. All experiments have been performed at ambient pool conditions ($p_\infty \approx 1\,\mathrm{bar}$).

	STAGNATION	NOZZLE EXIT STATE		
	PRESSURE	Mach no.	mass flux	pressure
	p_0/bar	Ma_e	$\dot{m}_e$/kg/(m^2 s)	p_e/bar
Wu et al. (2007), nozzle A	2	1.4	246.8 (0.2 %)	0.6
	4	1.4	483.6 (0.4 %)	1.2
Wu et al. (2007), nozzle B	2	1.9	132.7 (0.2 %)	0.2
	4	1.9	260.1 (0.4 %)	0.4
Wu et al. (2010a)	3	1.8	225.8 (0.4 %)	0.4
	5	1.8	370.8 (0.2 %)	0.7

Table 5.5: Selected simulation results for the flow conditions at the nozzle exit. Values in parentheses indicate the deviation from the literature data.

α_l/10^4 W/(m^2 K)	0.6	1.0	1.4	0.6	1.0	1.4
$E_{0,RT}$		$\Delta_{RMS}(L)$			max $\Delta(L)$	
0.12	44.3 %	28.0 %	24.7 %	137.4 %	94.8 %	71.6 %
0.16	29.5 %	23.6 %	27.5 %	102.6 %	65.2 %	53.4 %
0.20	23.6 %	27.1 %	33.6 %	80.0 %	55.0 %	59.6 %

Table 5.6: Root mean square deviation of the penetration length $\Delta_{RMS}(L)$ and maximum deviation max $\Delta(L)$ for different entrainment coefficients $E_{0,RT}$ and droplet heat transfer coefficients α_l

Jet penetration length

In figs. 5.12a and 5.12b, the simulated dimensionless jet penetration length L for different nozzle exit conditons and pool temperatures is compared with the experimental measurements from Wu et al. (2010a) and Wu et al. (2007), respectively. The predicted value of L shows satisfactory agreement with the experimental data for the second experiment, while simulation of the first experimental data set is less accurate. However, the qualitative dependency of the penetration length on both the pool temperature and the mass flux/stagnation pressure is predicted in both cases.

The two experiments shown in figs. 5.12a and 5.12b represent the weakest and strongest agreement with experimental data, respectively. The remaining simulation results are given in appendix D.2. In general, the simulation model predicts the qualitative trends of the dimensionless penetration length and provides a closer quantitative agreement with experimental data than the correlations provided in the literature, as can been seen in fig. 5.13.

(a) Experimental data from Wu et al. (2010a)

(b) from Wu et al. (2007)
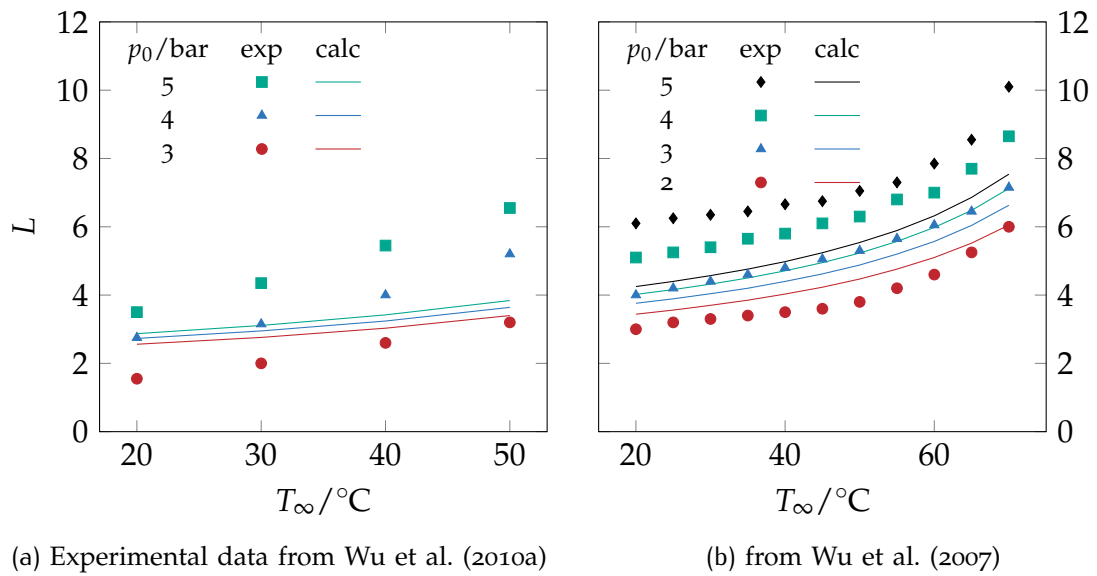
Figure 5.12: Dimensionless penetration length L for different pool temperatures T_∞ and steam stagnation pressures p_0: Comparison between experimental and calculated values

		$\Delta_{RMS}(L)$	$\max \Delta(L)$
●	present work	23.6 %	65 %
	CORRELATIONS		
∗	Chun et al. (1996)	49.9 %	69 %
×	Kerney et al. (1972)	50.5 %	70 %
○	Wu et al. (2007)	51.0 %	342 %
⋆	H. Y. Kim et al. (2001)	51.2 %	68 %
+	Weimer et al. (1973)	69.4 %	180 %
△	Wu et al. (2009a)	105.8 %	894 %
◇	Wu et al. (2010a)	221.1 %	2436 %
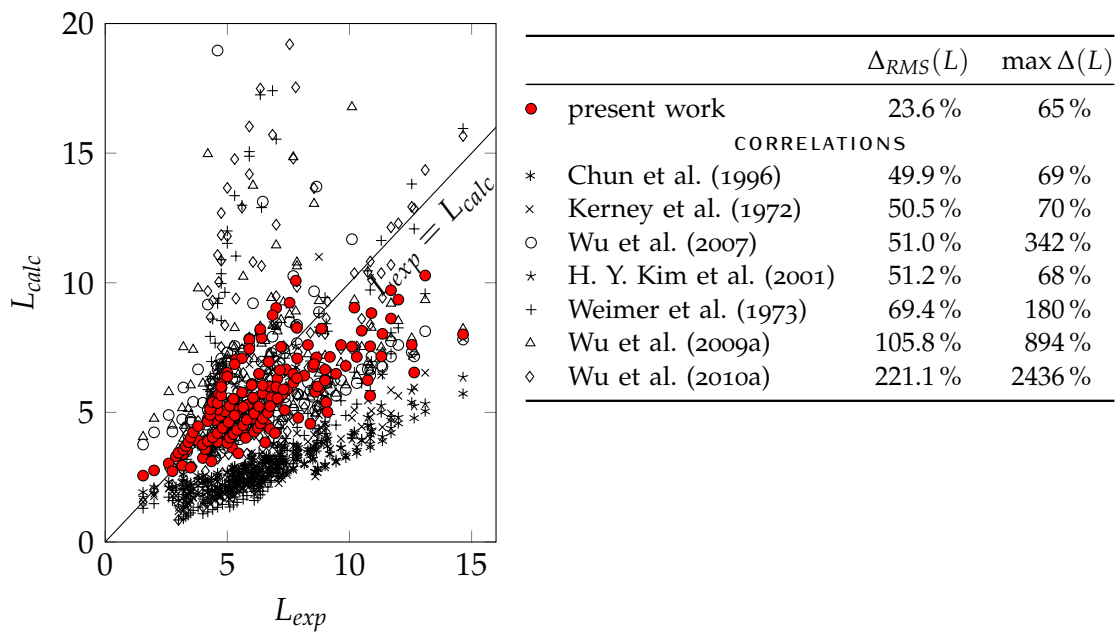
Figure 5.13: Comparison of empirical correlations and of the present simulations results for the dimensionless penetration length L_{calc} to experimental values L_{exp}. Experimental data from H. Y. Kim et al. (2001) and Wu et al. (2009a, 2010a, 2007).
$\Delta_{RMS}(L)$: root-mean square deviation of L; $\max \Delta(L)$: maximum deviation of L
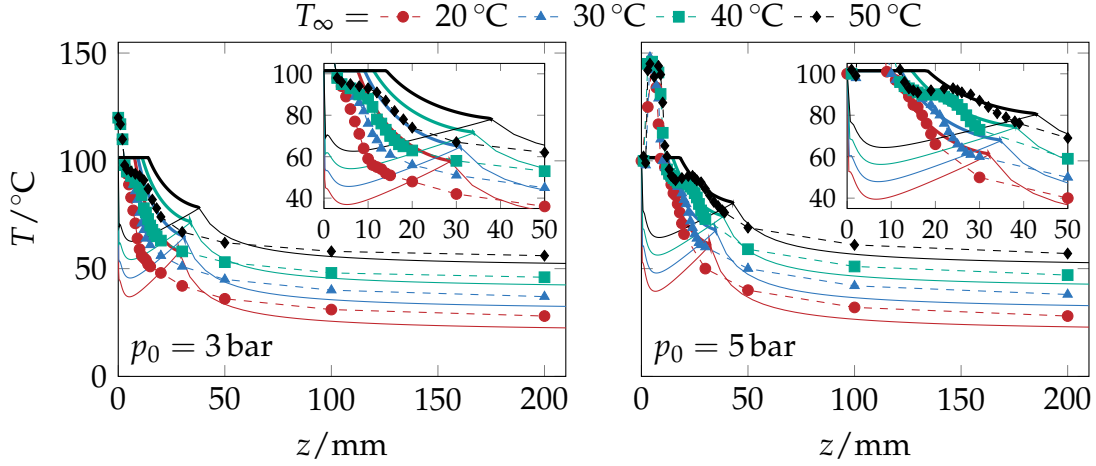
Figure 5.14: Axial temperature profile: Experimental values (Wu et al., 2010a) for different pool temperatures T_∞ (- ● - 20 °C; - ▲ - 30 °C; - ■ - 40 °C; - ◆ - 50 °C) and respective simulation results for the mean temperature T_m in the two-phase region (——; ——; ——; ——) and the liquid temperature T_l (——; ——; ——; ——). The gas temperature T_g in the two-phase region is equal to the constant saturation temperature at pool pressure and is not shown.

Axial temperature profile

In addition to the jet penetration length, the axial temperature profile of the two-phase jet has been measured by H. Y. Kim et al. (2001) and Wu et al. (2010a). Since the simulation model provides two different temperatures T_l and T_g in the two-phase region, an attempt was made to correlate the measurements using a mean temperature

$$T_m = f\left(h_m, p_\infty\right) \tag{5.106}$$

based on the density-averaged mean enthalpy

$$h_m = \frac{\epsilon_g \rho_g h_g + \epsilon_l \rho_l h_l}{\epsilon_g \rho_g + \epsilon_l \rho_l} \quad . \tag{5.107}$$

Moreover, the simulation was continued from the end of the two-phase flow region by setting $\tilde{\epsilon}_l = 1$ and $\Gamma_l = \dot{q}_{l,if} = 0$, which converts eqs. (5.53), (5.54) and (5.56) into the conservation equations for a single-phase, two-fluid jet with turbulent entrainment (fluid l for $r \leq R_{2ph}$, fluid w for $R_{2ph} < r \leq R_w$). This allowed for a direct comparison between experiment and simulation in the condensation-induced single-phase jet region ($z > l$).

Selected results obtained in this manner are shown in fig. 5.14, the remaining results can be found in appendix D.2. The temperature is overestimated initially
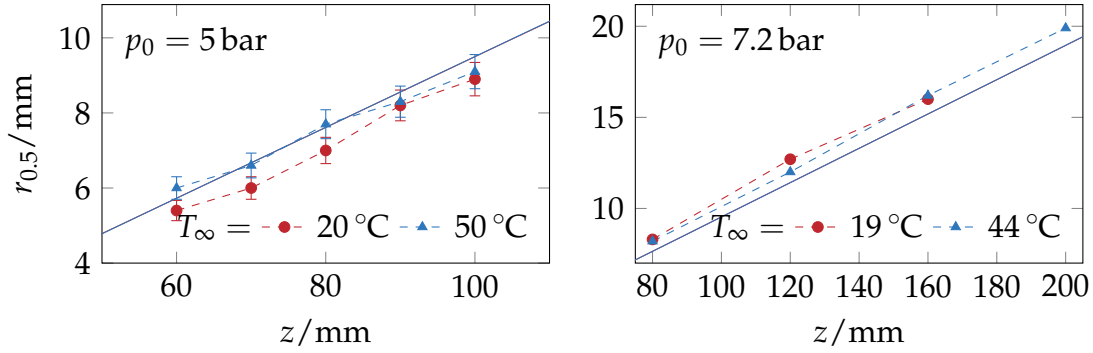
(a) Experimental data from Wu et al. (2010b) (b) from Y.-S. Kim and Youn (2008)

Figure 5.15: Jet half radius $r_{0.5}$ along the jet axis z for the condensation-induced liquid jet: Experimental values at different stagnation pressures p_0 and pool temperatures T_∞ (●; ▲) and respective simulation results (——; ——)

in the two-phase region, but accurately predicted further downstream. The temperature peaks in the experimental data are due to periodic oblique shocks and expansion waves which are neglected in the simulation model.

Jet half-radius

As pointed out in section 5.2.1, experiments have shown that a condensation-induced turbulent liquid jet is in good agreement with the turbulent jet theory and that its radial profile of the axial velocity can therefore be described by a Gauss-distribution:

$$\frac{c(z,r)}{c(z,0)} = \exp\left[-\ln 2 \left(\frac{r}{r_{0.5}}\right)^2\right] \tag{5.5 revisited}$$

This allows to obtain a relationship[4] between the one-dimensional jet model (where $c = c_l$ for $r \leq R_{2ph}$ and $c = c_w$ for $R_{2ph} < r \leq R_w$) and the jet half radius $r_{0.5}$:

$$r_{0.5} = \sqrt{\frac{\ln 2}{2} \frac{c_l R_{2ph}^2 + c_w \left(R_w^2 - R_{2ph}^2\right)}{\sqrt{c_l^2 R_{2ph}^2 + c_w^2 \left(R_w^2 - R_{2ph}^2\right)}}} \tag{5.108}$$

Using eq. (5.108), the calculated jet radius can be compared with experimental data for the half radius of the liquid jet. The simulation results match closely with experimental data by Y.-S. Kim and Youn (2008) and Wu et al. (2010b), as shown in fig. 5.15 and appendix D.2.

---

4 derivation in appendix C

5.7.2   Channel DCC

In contrast to the extensive literature on pool DCC, there is little data on channel DCC. To the author's knowledge, the only experimental studies are by Q. Xu et al. (2013) and Zong et al. (2015). In the experiments by Zong et al., steam was injected in the lower half of a rectangular, horizontal channel. The data obtained by these authors is therefore not directly applicable to the present work. Q. Xu et al. performed experiments in a circular, vertical pipe with a diameter of 80 mm, where initially saturated steam ($x_{g,0} = 1$) was injected coaxially through a 8 mm nozzle. Water inlet temperature T_w, Reynolds number Re_w and steam mass flux $\dot{m}_e$ were varied and the plume length and radial temperature distribution were measured. The measurements of the plume length will be used for validation of the present model.

The authors report stable steam jets with mass fluxes at the nozzle exit between 150 kg/(m² s) and 500 kg/(m² s) for steam stagnation pressures between 2 bar and 7 bar. According to the authors, the steam flow rate was controlled by adjusting manual control valves, but no further information is given concerning the detailed steam injection conditions. Therefore, the following assumptions are made to reproduce the experimental setup:

- The static water inlet pressure p_w is assumed to be atmospheric (1 bar).

- Steam stagnation pressures are taken as $2, 3, \ldots, 7$ bar.

- The experiments include steam mass fluxes below the critical (sonic) flux at atmospheric pressure (279 kg/(m² s)). For stable injection, the steam exit velocity must therefore be supersonic.

- The critical (smallest) diameter d_{crit} is presumed to be the manual control valve. This value was varied in order to obtain the reported steam mass fluxes.

The injection conditions calculated in this manner are listed in table 5.7.

Parametric study: Determination of $\hat{t}_b$

A qualitative comparison of the simulation results for different values of the surface renewal rate $\hat{t}_b$ indicates the best agreement with experimental data for $\hat{t}_b = 10$ (fig. 5.16). At higher values (i. e. lower heat transfer coefficients at the jet interface), the decrease in plume length with increasing Reynolds number is not observed. At lower values, the increase in plume length with increasing steam mass flux is not reproduced properly.

| STAGNATION PRESSURE p_0/bar | DIAMETER RATIO d_e/d_{crit} | NOZZLE EXIT STATE | | | |
		Mach no. Ma_e	mass flux $\dot{m}_e$/kg/(m²s)	pressure p_e/bar	quality $x_{g,e}$
2	1.341	1.73	166 (0.04 %)	0.31	0.907
3	1.415	1.81	221 (0.03 %)	0.39	0.897
4	1.456	1.85	276 (0.02 %)	0.48	0.891
5	1.48	1.88	332 (−0.05 %)	0.57	0.886
6	1.497	1.90	387 (0.05 %)	0.66	0.883
7	1.51	1.91	442 (0.03 %)	0.75	0.880
7	1.424	1.82	497 (0.03 %)	0.89	0.887

Table 5.7: Simulation results for the flow conditions at the nozzle exit. The ratio between nozzle exit and critical diameter is not provided by Q. Xu et al. (2013), it has been set to obtain the experimental mass flux $\dot{m}_e$. Values in parentheses indicate the deviation from the literature data.
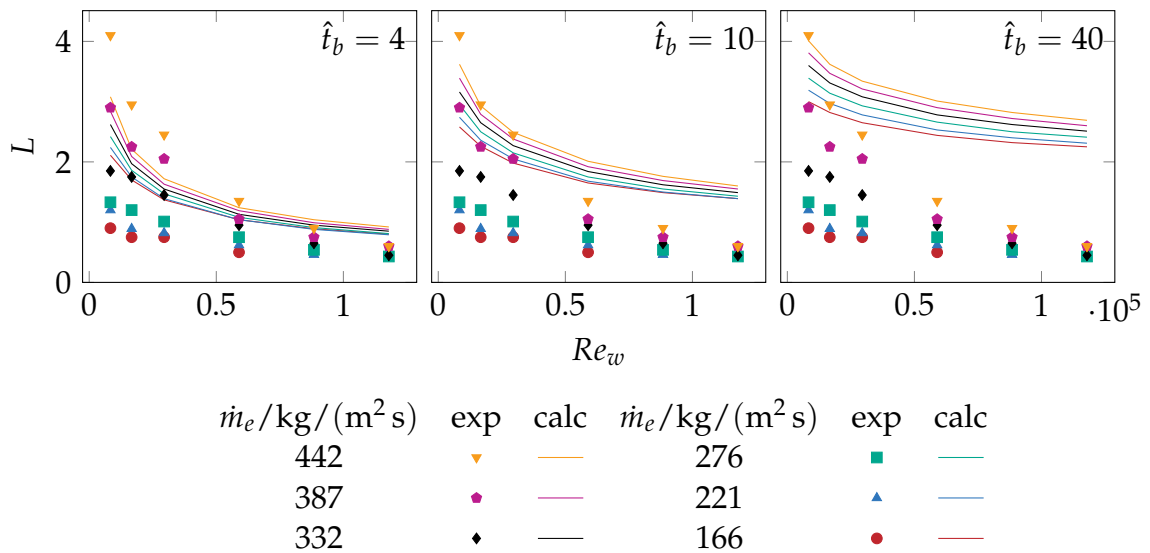
Figure 5.16: Dimensionless penetration length L vs. water Reynolds number Re_w for different surface renewal rates $\hat{t}_b$ (experimental data by Q. Xu et al. (2013), water temperature $T_w = 40\,°C$)

Jet penetration length

The simulated dimensionless jet penetration length L for different steam flow rates, water flow rates and water temperatures is compared with the experimental measurements from Q. Xu et al. (2013) in fig. 5.17. All trends are observed qualitatively, however, satisfactory absolute agreement is only achieved for high steam mass fluxes $\dot{m}_e$ and low Reynolds number Re_w (fig. 5.17c). The decrease of L for decreasing steam mass fluxes at low Reynolds numbers is underpredicted (fig. 5.17b), and the virtual independence of the water temperature at high Reynolds number is not observed (fig. 5.17c).

5.7.3 Interpretation of results

In pool DCC, the dimensionless jet penetration length is mainly dependent on the water temperature and the steam mass flux. Both dependencies are predicted by the developed model, and good quantitative agreement could be obtained for most experimental data sets. In addition, the axial profiles of the centerline temperature and the jet half radius match closely with experimental data for the condensation-induced single-phase jet. These results support the validity of the developed model and the employed entrainment correlations.

The entrainment model for the droplet region assumes a thin laminar boundary layer at the steam nozzle exit and cannot account for specific characteristics of the nozzle geometry under consideration. Therefore, two-dimensional flow phenomena in the steam nozzle are a possible explanation for the discrepancy between the simulation model and some experiments. Furthermore, a more detailed treatment of the heat transfer within entrained droplets may be necessary to improve the prediction of the axial temperature profile in the two-phase region. Here, additional research is required to develop a computationally efficient method.

The superposition of two condensation mechanisms – condensation on droplets and at the jet interface – allows to qualitatively predict the trends observed in channel DCC as well, where condensation is strongly dependent on the flow Reynolds number in addition to the water temperature and the steam mass flux. This supports the hypothesis that exchange mechanisms at a condensing jet interface can be treated with similar methods as stratified condensing flows.

Additional experiments are required to confirm the general validity for channel DCC. In order to augment the simulation accuracy, detailed local measurements

are necessary to identify possible differences between stratified condensation and jet condensation that should be accounted for. Moreover, a potential inter-dependency between condensation and entrainment at the jet interface might offer further room for improvements and should thus be investigated.

The model relies on three parameters ($E_{0,RT} = 0.16$, $\alpha_l = 10^4 \, \text{W}/(\text{m}^2\,\text{K})$ and $\hat{t}_b = 10$) that were chosen by parametric study. The employed values are reasonably close to recommended values in similar fields. It should be emphasized that these parameters were kept fixed for all simulations and not adjusted to the individual experiments.

In summary, the developed model is capable of reproducing all major trends observed in DCC of submerged steam jets in open and confined environments. This suggests that the underlying physical mechanisms have been properly identified and reproduced.
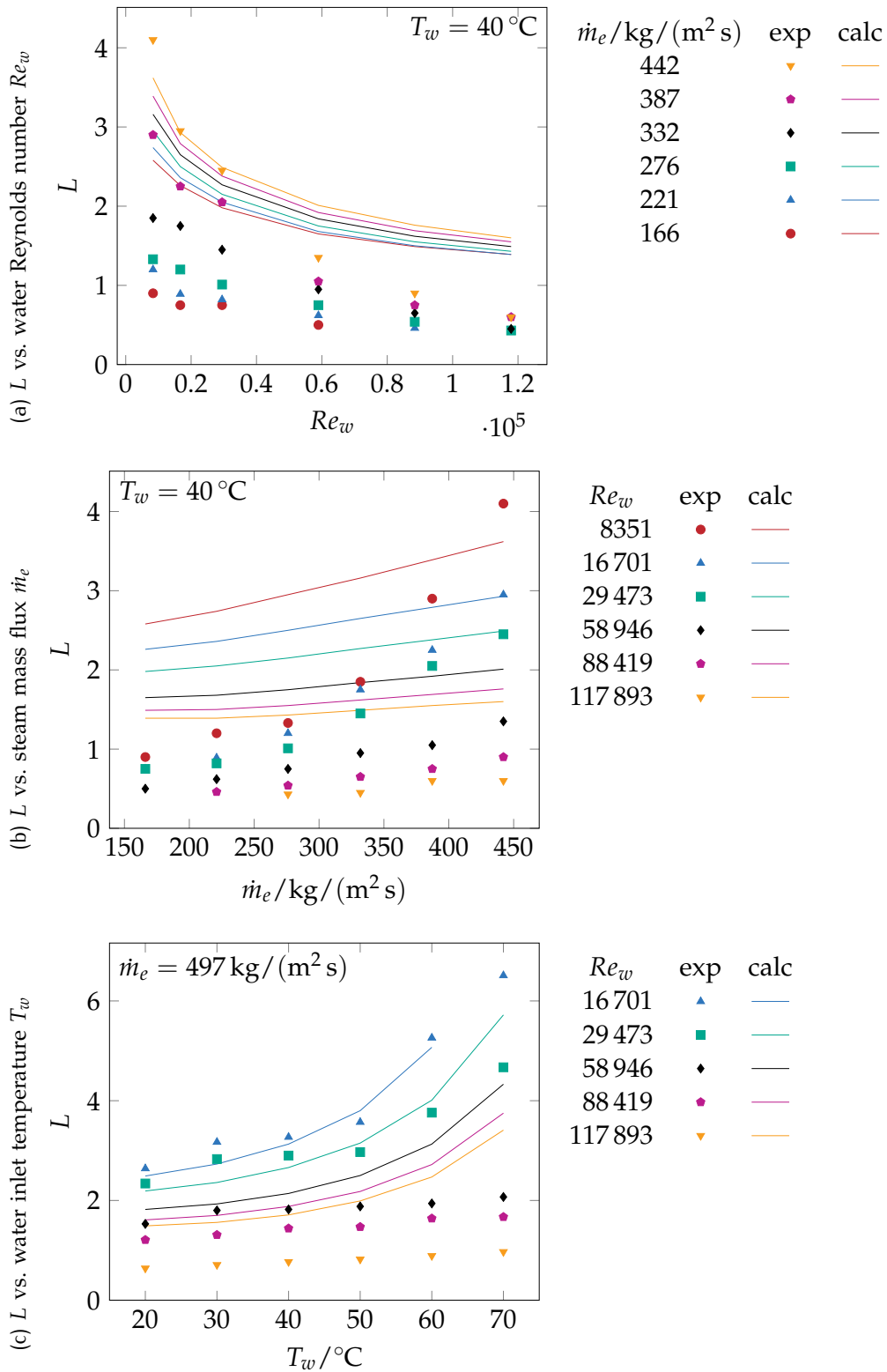
Figure 5.17: Dimensionless penetration length L for channel DCC: Comparison between experimental data by Q. Xu et al. (2013) and calculated values

Dampfstrahlpumpen, *Injektoren* (injectors; injecteurs; iniettori), *Kesselspeisevorrichtungen, bei denen die durch Kondensieren eines Dampfstrahls erzeugte lebendige Kraft dem Wasser eine derartige Beschleunigung erteilt, daß dieses den entgegenstehenden Kesseldruck überwindet und in den Kessel eintritt.*

— Victor von Röll, *Enzyklopädie des Eisenbahnwesens*, 1912

6 | CONSOLIDATED STEAM INJECTOR MODEL

6.1 SIMULATION MODEL

In order to simulate the flow in a steam injector mixing chamber, the model for channel DCC developed in the previous chapter was applied. However, the numerical solver scheme did not converge when using injector geometries with a tapered instead of a constant flow cross-section. The following adjustments had to be made to resolve these numerical instabilities:

- The droplet entrainment coefficient was reduced from $E_{0,RT} = 0.16$ to 0.01.

- To counterbalance the resulting decrease of interfacial area density due to the reduced droplet entrainment, the droplet heat transfer coefficient was increased from $\alpha_l = 10^4 \, \text{W}/(\text{m}^2 \, \text{K})$ to $16 \times 10^4 \, \text{W}/(\text{m}^2 \, \text{K})$.

- The wall friction was neglected ($\tau_{wall} = 0$).

These changes have no physical relevance and were merely included to obtain a converging solution. The (physically unlikely) implications are as follows:

- The relative void fraction in the two-phase jet region $\tilde{\epsilon}_g$ decreases more slowly due to the decreased entrainment coefficient.

- Thermal equilibrium between droplets and steam is reached almost instantaneously owing to the increased droplet heat transfer coefficient.

- Pressure losses by wall friction cannot be considered.

As a result, thermal equilibrium in the two-phase jet region and mechanical equilibrium ($c_g = c_w$) between the jet and the surrounding water was reached during simulation. This situation is beyond the scope of the model: Heat transfer at the jet interface is modeled as a function of the interfacial shear stress, thus becoming zero for $c_g = c_w$. In consequence, no further fluid exchange can be considered.

As a remedial measure, a homogeneous mixture model was applied at this point. The transition from the three-fluid model to the homogeneous mixture model (index m) is assumed to occur instantaneously based on the conservation equations:

$$\sum_i \epsilon_i \rho_i c_i = \rho_m c_m \tag{6.1}$$

$$p + \sum_i \epsilon_i \rho_i c_i^2 = p_m + \rho_m c_m^2 \tag{6.2}$$

$$\sum_i \epsilon_i \rho_i c_i \left(h_i + 0.5 c_i^2 \right) = \rho_m c_m \left(h_m + 0.5 c_m^2 \right) \tag{6.3}$$

The mixture density can be calculated from the equation of state based on the mixture pressure and enthalpy, leaving three unknown variables p_m, h_m and c_m. These are obtained as follows:

1. The mixture pressure p_m is estimated.

2. Continuity and momentum conservation (eqs. (6.1) and (6.2)) are used to calculate the mixture velocity:

$$c_m = \frac{p - p_m + \sum_i \epsilon_i \rho_i c_i^2}{\sum_i \epsilon_i \rho_i c_i} \tag{6.4}$$

3. The mixture enthalpy is obtained from continuity and energy conservation (eqs. (6.1) and (6.3)):

$$h_m = \frac{\sum_i \epsilon_i \rho_i c_i \left(h_i + 0.5 c_i^2 \right)}{\sum_i \epsilon_i \rho_i c_i} - \frac{c_m^2}{2} \tag{6.5}$$

4. The equation of state is used to determine the mixture density: $\rho_m = f(p_m, h_m)$

5. Steps 2–4 are iterated[1] until momentum conservation (eq. (6.2)) is fulfilled.

update p_m

6.2 PRELIMINARY RESULTS

Yan et al. (2005) measured the axial static pressure profile $p(z)$ in a steam injector mixing chamber using pressure taps at the chamber wall. The experiments were performed with a constant water inlet temperature $T_w = 291\,\text{K}$, the steam stagnation pressure p_0 was varied between 2 bar and 6 bar.

---

1 multidimensional root finding algorithm for $n = 1$ variables according to appendix B.5
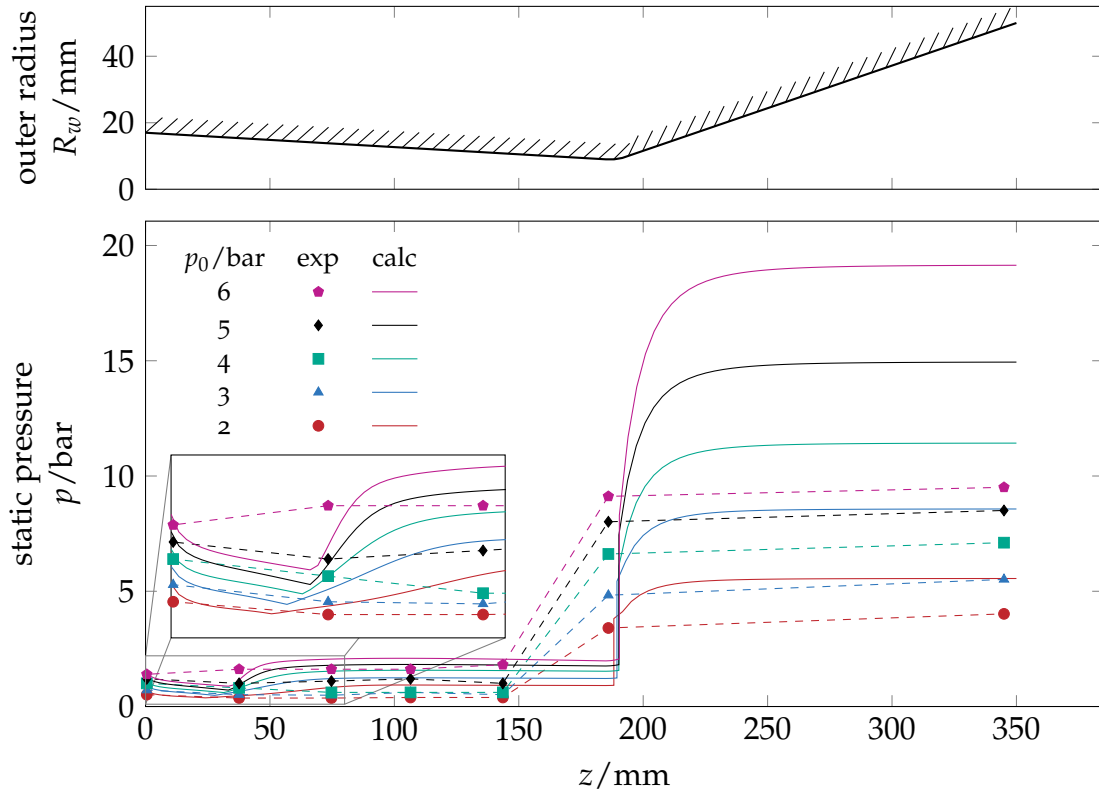
Figure 6.1: Preliminary results for the static pressure $p(z)$ in the mixing chamber: Experimental values (Yan et al., 2005) for different steam stagnation pressures p_0 (● 2 bar; ▲ 3 bar; ■ 4 bar; ♦ 5 bar; ⬠ 6 bar) and respective simulation results (——; ——; ——; ——; ——)

For $p_0 < 6$ bar, the measured pressure decreases slightly between the first two pressure taps, while it increases slightly for $p_0 = 6$ bar (fig. 6.1). Afterwards, the pressure remains fairly constant up to the mixing chamber throat, where the pressure increases by a factor of approximately 5 to 10.

The preliminary simulation model was applied to this experimental setup, using inlet conditions according to the experimental data provided by the authors. The pressure profile obtained in this way is shown in fig. 6.1. The model is capable of reproducing the general experimental trends, but overestimates the pressure rise at the mixing chamber throat, in particular for high steam stagnation pressures. Moreover, the simulated pressure shows a slight decrease from the mixing chamber inlet up to $z \approx 40$ mm and a subsequent increase for all stagnation pressures. This pressure rise is steeper for higher stagnation pressures.

6.3 DISCUSSION

The simulations results shown in the previous section demonstrate the general feasibility of the DCC model for steam injectors. However, additional work is required to improve numerical stability and simulation accuracy. In particular, the following issues should be addressed:

- *Revision of the two-phase jet entrainment hypothesis.* While the entrainment model could be successfully applied to channel DCC, it did not yield stable results for tapered ducts. Therefore, the entrainment hypothesis proposed in section 5.5.3 ($c_{en,RT} \propto \tilde{\lambda}_{RT}\omega_{RT}$) should be revisited and validated in-depth. As discussed in section 5.2.2, the turbulent jet theory assumes a virtual point source, which may be invalid for confined jets. This point should also be considered, as well as the influence of background turbulence on entrainment. This topic is subject of ongoing research (e.g. Khorsandi et al., 2013).

- *Consideration of two-dimensional effects.* In the experiments of Yan et al. (2005), the pressure was measured at the wall, while the simulation model provides an area-averaged value. It is possible that two-dimensional effects due to the converging geometry and the two-phase flow result in pressure variations over the flow cross-section. Additional experimental data is necessary to assess this issue. The non-isothermal Craya-Courtet number might offer further insights, however, the square root of eq. (5.27) becomes imaginary for the inlet conditions of Yan et al. (2005) and Ct is thus undefined.

- *Improvement of numerical stability.* The present model does not take into account the influence of viscous and turbulent stress on the momentum conservation (cf. e.g. Ishii and Mishima, 1984). Inclusion of this term is known to improve numerical stability.

At first acquaintance, the operation looks as if it had a strong likeness to perpetual motion, but closer investigation will show that the steam which raises and forces the water by passing through an injector performs mechanical work as truly as the steam that pushes a piston which moves a pump-plunger.

— Angus Sinclair, *Locomotive engine running and management*, 1887

7 | SUMMARY AND CONCLUSION

The steam injector is an electricity-independent pumping device which fulfills the criteria of a passive component according to *International Atomic Energy Agency* (IAEA) category D. As such, it could be used as part of a passive emergency core cooling system. Motivated by the need for generally valid, computationally efficient steam injector simulation models suitable for system studies, the two-phase condensing flow in steam injectors has been investigated and physically-based models have been developed in the present work.

Homogeneous nucleation and droplet growth during expansion in the steam nozzle was modeled based on the classical nucleation theory and a droplet growth model by Peters and Meyer (1995) which takes into account molecular exchange processes in the vicinity of nanodroplets. This model is capable of accurately predicting the axial position of the condensation-induced pressure rise, but overestimates the pressure rise itself. It is believed that revision of the droplet growth model may remedy this issue.

In order to simulate the two-dimensional gas dynamic phenomena of *oblique shocks and expansion waves* at the steam nozzle exit, models for two-dimensional single-phase gas dynamics have been combined with methods for one-dimensional normal shocks in steam-droplet flows. The geometric shape of under- and overexpanded submerged steam jets can be predicted accurately by the developed model. However, validation was limited to visual comparison, and more detailed quantitative experimental data is desirable.

Direct contact condensation (DCC) of the steam jet in the mixing chamber is believed to be the dominant mechanism occurring in the steam injector. Therefore, the main part of the present work has been devoted to the detailed examination of the DCC phenomenon, in particular because previous work in this area seldom considered the underlying physical processes in-depth. For this purpose, experimental findings on DCC in pools and channels were examined.

Experiments on pool DCC suggest that the condensation is primarily influenced by the pool water temperature and the steam mass flux at the nozzle exit. These dependencies could be predicted by extending the entrainment hypothesis for turbulent jets, which is based on the Kelvin-Helmholtz theory, to additionally take into account the influence of the Rayleigh-Taylor instability and of the vorticity layer of the gas stream. This was done by adapting a model for liquid jets in high-speed gas streams developed by Varga et al. (2003). In doing so,

the initial size of entrained droplets could be determined as well, and the final droplet size after aerodynamic atomization was then calculated according to models developed by Hsiang and Faeth (1992) and Wert (1995).

Recent experiments on channel DCC illustrate the strong influence of the Reynolds number of the water flow on the condensation efficiency. The present work postulates that exchange processes at the interface of a condensing steam jet can be treated with the methodology of the surface renewal theory originally developed for stratified two-phase flows. This concept correlates the interfacial heat transfer coefficient with the interfacial shear stress. In stratified flows, several independent experiments have shown the influence of the water flow Reynolds number on the interfacial friction factor. By adapting these correlations to a condensing steam jet in flowing water, the dependency of the steam jet length on the Reynolds number of the water flow could be reproduced.

The two mechanisms of steam condensation on entrained droplets on the one hand and at the jet interface on the other hand were combined to yield a model applicable for both pool and channel DCC. Superposition of both processes is achieved by using appropriate values for the entrainment coefficient and the proportionality factor required for the heat transfer coefficient at the jet interface. These factors have been determined by parametric studies and are reasonably close to values used in the context of the original theories.

The developed DCC model is in good qualitative and acceptable quantitative agreement with various experimental data sets for both pool and channel DCC. The model parameters were kept constant for all simulations, and no adaptation to the specific experiments was necessary to model the observed trends.

Preliminary results for DCC in a mixing chamber demonstrate the feasibility of the model approach for steam injector simulations. However, additional work is required to remedy numerical instabilities, in particular concerning the assumptions underlying the jet entrainment model.

A | THERMODYNAMIC SUPPLEMENT

A.1 THERMODYNAMIC PROPERTY CALCULATION

All thermodynamic properties are calculated based on the IAPWS *Industrial Formulation 1997 for the Thermodynamic Properties of Water and Steam* (IAPWS-IF97) (Wagner et al., 2000). The validity range is specified as follows:

$$273.15\,\text{K} \leq T \leq 1073.15\,\text{K} \qquad p \leq 100\,\text{MPa}$$
$$1073.15\,\text{K} < T \leq 2273.15\,\text{K} \qquad p \leq 50\,\text{MPa}$$

The IAPWS-IF97 divides the *p-T*-diagram into five regions. For the conditions expected in steam injectors, regions 1 (liquid water) and 2 (water vapor) are of particular interest. Thermodynamic properties in these regions are expressed as functions of pressure and temperature. However, the formulation features an additional "backward equation" to determine the temperature based on pressure and enthalpy, which is used in the simulation model.

The IAPWS-IF97 provides a supplementary equation for metastable vapor, which is valid from the saturated vapor line to the 5 % equilibrium moisture line (determined from the equilibrium enthalpy values of saturated liquid and water) at pressures from the triple-point pressure up to 10 MPa. No backward equation is provided for metastable vapor. Therefore, $h(p, T) - h = 0$ is solved iteratively for a given pressure p and enthalpy h, using the saturation temperature $T_{sat}(p)$ as first estimate. The numerical root finding scheme uses a modified Newton method (`gsl_multiroot_fdfsolver_gnewton`) as implemented in the GNU Scientific Library (Gough, 2009).

The surface tension $\sigma(T)$ is determined according to Cooper (1994), the heat conductivity $\lambda(T, \rho)$ according to Huber et al. (2012). Both formulations are assumed to hold for metastable vapor as well. Partial derivatives are determined based on Wagner and Kretzschmar (2008).

The computer implementation uses the "Freesteam" library (Pye, 2010), which has been augmented to allow for metastable vapor.

A.2 THERMODYNAMICS OF NANODROPLETS

At curved liquid-vapor phase boundaries, the surface tension σ results in a normal force. This force changes the conditions for mechanical and thermodynamic equilibrium and leads to changes in both the internal droplet pressure p_l and the saturation vapor pressure in comparison to a flat phase boundary.

A.2.1 Young–Laplace equation

Assume a surface element of a droplet with radius r and infinitesimally small cutting angles $d\theta$ and $d\phi$, as depicted in fig. A.1. The surface tension σ causes forces $F_\sigma = \sigma \cdot r \, d\theta$ and $F_\sigma = \sigma \cdot r \, d\phi$ acting on the edges of the element. Using the small angle approximation, the normal components of these forces sum up to yield

$$F_\perp = 2\sigma r \cdot \left(d\phi \sin \frac{d\theta}{2} + d\theta \sin \frac{d\phi}{2} \right) = 2\sigma r \, d\theta \, d\phi \, . \tag{A.1}$$

For mechanical equilibrium, this force must be balanced by a pressure difference between the liquid and the vapor phase:

$$\left(p_l - p_g \right) \cdot r^2 \, d\theta \, d\phi = F_\perp \tag{A.2}$$

Combination of eqs. (A.1) and (A.2) results in the Young-Laplace equation for the internal pressure of small droplets:

$$p_l = p_g + \frac{2\sigma}{r} \tag{A.3}$$
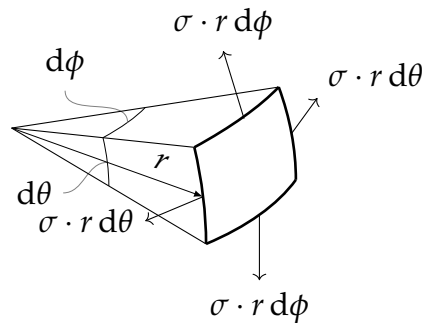
Figure A.1: Surface element of a droplet with radius r. The surface tension σ causes forces $F_\sigma = \sigma \cdot r \, d\theta$ and $F_\sigma = \sigma \cdot r \, d\phi$ acting on the edges of the element.

A.2.2 Kelvin's equation

For thermodynamic equilibrium, the Gibbs free energy has to be constant. At a vapor-liquid phase boundary, this condition can be expressed as

$$-s_g\, dT + v_g\, dp = -s_l\, dT + v_l\, dp\, .\tag{A.4}$$

Introducing the Young-Laplace-pressure, A.3, neglecting the specific liquid volume with respect the specific vapor volume ($v_g - v_l \approx v_g$), and assuming constant temperature ($dT = 0$) results in

$$dp_g = \frac{v_l}{v_g}\, d\left(\frac{2\sigma}{r}\right)\, ,\tag{A.5}$$

or for ideal gases

$$\frac{dp_g}{p_g} = \frac{v_l}{R_s T}\, d\left(\frac{2\sigma}{r}\right)\, .\tag{A.6}$$

For a plain surface ($r \to \infty$), the vapor pressure at thermodynamic equilibrium is equal to the saturation pressure ($p_g = p_{sat}$). Integration with $r \to \infty$ as lower limit while assuming an incompressible liquid yields Kelvin's equation for the saturation vapor pressure of small droplets:

$$p_{sat,r}(T,r) = p_{sat}(T) \cdot \exp\left(\frac{2\sigma v_l}{r R_s T}\right)\tag{A.7}$$

B | NUMERICAL DETAILS

B.1 STEAM NOZZLE EQUATION SYSTEM

Using eqs. (3.16), (3.17) and (3.19) to (3.21) in combination with eqs. (3.27) and (3.28), the ODE system for steam nozzle two-phase flow can be cast into the following explicit form:

$$\frac{\mathrm{d}c}{\mathrm{d}z} = -C_2 \tag{B.1}$$

$$\frac{\mathrm{d}p_g}{\mathrm{d}z} = c\rho_m \cdot C_2 \tag{B.2}$$

$$\frac{\mathrm{d}h_g}{\mathrm{d}z} = \frac{\sum_{i=1}^{k}\left(m_{drp,i}J_i\Delta h_{lg,i} - n_i\dot{Q}_i\right)}{c\left(1 - x_l\right)} + c\frac{\rho_m}{\rho_g}\cdot C_2 \tag{B.3}$$

$$\frac{\mathrm{d}x_i}{\mathrm{d}z} = \frac{1}{c}\left(n_i\dot{M}_i + m_{drp,i}J_i\right) \tag{B.4}$$

$$\frac{\mathrm{d}n_i}{\mathrm{d}z} = \frac{J_i}{c} \tag{B.5}$$

$$C_2 = \frac{\frac{c}{A}\frac{\mathrm{d}A}{\mathrm{d}z} - \rho_m\sum_{i=1}^{k}\left[\left(v_g - v_i\right)\left(n_i\dot{M}_i + m_{drp,i}J_i\right) + \left.\frac{\partial v_g}{\partial h_g}\right|_{p_g}\left(m_{drp,i}J_i\Delta h_{lg,i} - n_i\dot{Q}_i\right)\right]}{1 + c^2\rho_m\left(1 - x_l\right)\left(\left.\frac{\partial v_g}{\partial p_g}\right|_{h_g} + v_g\left.\frac{\partial v_g}{\partial h_g}\right|_{p_g}\right)} \tag{B.6}$$

B.2 ISENTROPIC EXPANSION OF STEAM

In situations where non-equilibrium effects during expansion (cf. chapter 3) cannot be considered (e. g. due to insufficient information about the nozzle geometry), the nozzle exit state is determined based on the homogeneous equilibrium model assuming isentropic and isenthalpic equilibrium expansion.

The choked flow state at the nozzle throat is then determined as follows:

1. The critical pressure and enthalpy p_{crit}, h_{crit} are estimated using the ideal gas solution.

2. The critical entropy s_{crit} and the homogeneous equilibrium speed of sound $w_{h,crit}$ are calculated based on the equation of state and eq. (4.34).

3. Step 2 is iterated[1] until the conditions for isentropic and isenthalpic flow are fulfilled:

$$s_{crit} = s_0 \tag{B.7}$$
$$h_{crit} = h_0 - 0.5w_{h,crit}^2 \tag{B.8}$$

Now, the nozzle exit state can be calculated:

1. The exit pressure p_e and velocity c_e are estimated using the ideal gas solution.

2. The exit enthalpy is determined from the total enthalpy conservation:

$$h_e = h_0 - 0.5c_e^2 \tag{B.9}$$

3. The exit density ρ_e is obtained from the equation of state.

4. Steps 2–3 are iterated[2] until the conditions for isentropic flow and continuity are fulfilled:

$$s_e = s_0 \tag{B.10}$$
$$\rho_e c_e A_e = \rho_{crit} c_{crit} A_{crit} \tag{B.11}$$

(margin note: update p_{crit} and h_{crit})

(margin note: update p_e and c_e)

---

1 multidimensional root finding algorithm for $n = 2$ variables according to appendix B.5
2 multidimensional root finding algorithm for $n = 2$ variables according to appendix B.5

B.3 DCC EQUATION SYSTEM

B.3.1 Pool DCC

Using eqs. (5.53), (5.54) and (5.56) in conjunction with eq. (5.101), assuming a constant pressure ($\frac{dp}{dz} = 0$) and expressing the flow cross-section as $A = \pi R_w^2$, the ODE system for pool DCC two-phase flow can be cast into the following explicit form:

$$\frac{dR_w}{dz} = \frac{R_w}{2} \sum_i \epsilon_i \left[C_{i1} - C_{i2} + \rho_i h_i \left. \frac{\partial v_i}{\partial h_i} \right|_p \left(C_{i3} - \frac{c_i^2}{h_i} C_{i2} \right) \right] \tag{B.12}$$

$$\frac{d\epsilon_i}{dz} = \epsilon_i \left[C_{i1} - C_{i2} + \rho_i h_i \left. \frac{\partial v_i}{\partial h_i} \right|_p \left(C_{i3} - \frac{c_i^2}{h_i} C_{i2} \right) \right] - \epsilon_i \frac{2}{R_w} \frac{dR_w}{dz} \tag{B.13}$$

$$\frac{dh_i}{dz} = h_i C_{i3} - c_i^2 C_{i2} \tag{B.14}$$

$$\frac{dc_i}{dz} = c_i C_{i2} \tag{B.15}$$

$$C_{i1} = \frac{\sum_j \Gamma_{j \to i}}{\epsilon_i \rho_i c_i} \tag{B.16}$$

$$C_{i2} = \frac{\sum_j \left[\left(c_{if,ij} - c_i \right) \Gamma_{j \to i} + M_{j \to i} \right]}{\epsilon_i \rho_i c_i^2} \tag{B.17}$$

$$C_{i3} = \frac{\sum_j \left[\Gamma_{j \to i} \left(h_{i,j} - h_i + c_{if,ij} c_i - c_i^2 \right) + a_{if,ij} \dot{q}_{j \to i} + M_{j \to i} c_{if,ij} \right]}{\epsilon_i \rho_i c_i h_i} \tag{B.18}$$

The change in interfacial area density of the dispersed phase is given based on eq. (5.60) as

$$\frac{da_{if,d}}{dz} = a_{if,d} \left[C_{d4} - C_{d2} + \frac{2}{3} \rho_d h_d \left. \frac{\partial v_d}{\partial h_d} \right|_p \left(C_{d3} - \frac{c_d^2}{h_d} C_{d2} \right) - \frac{2}{R_w} \frac{dR_w}{dz} \right] \quad , \tag{B.19}$$

$$C_{d4} = \frac{2}{3} \frac{\Gamma_{c \to d}}{\epsilon_d \rho_d c_d} + \frac{\Phi_d}{a_{if,d} c_d} \quad . \tag{B.20}$$

B.3.2   Channel DCC

Using eqs. (5.53), (5.54) and (5.56) in conjunction with eq. (5.101) and assuming a given flow cross-section $A(z)$, the ODE system for channel DCC two-phase flow can be cast into the following explicit form:

$$
\frac{\mathrm{d}p}{\mathrm{d}z} = \frac{\sum_i \epsilon_i \left[C_{i1} - \left(1 + \rho_i c_i^2 \left. \frac{\partial v_i}{\partial h_i} \right|_p \right) C_{i2} + \rho_i h_i \left. \frac{\partial v_i}{\partial h_i} \right|_p C_{i3} \right]}{- \sum_i \epsilon_i \left[\rho_i \left. \frac{\partial v_i}{\partial p} \right|_{h_i} + \left. \frac{\partial v_i}{\partial h_i} \right|_p + \frac{1}{\rho_i c_i^2} \right]}
\tag{B.21}
$$

$$
\begin{aligned}
\frac{\mathrm{d}\epsilon_i}{\mathrm{d}z} &= \epsilon_i \left[C_{i1} - \left(1 + \rho_i c_i^2 \left. \frac{\partial v_i}{\partial h_i} \right|_p \right) C_{i2} + \rho_i h_i \left. \frac{\partial v_i}{\partial h_i} \right|_p C_{i3} \right] \\
&\quad + \epsilon_i \left[\rho_i \left. \frac{\partial v_i}{\partial p} \right|_{h_i} + \left. \frac{\partial v_i}{\partial h_i} \right|_p + \frac{1}{\rho_i c_i^2} \right] \frac{\mathrm{d}p}{\mathrm{d}z}
\end{aligned}
\tag{B.22}
$$

$$
\frac{\mathrm{d}h_i}{\mathrm{d}z} = h_i C_{i3} - c_i^2 C_{i2} + \frac{1}{\rho_i} \frac{\mathrm{d}p}{\mathrm{d}z}
\tag{B.23}
$$

$$
\frac{\mathrm{d}c_i}{\mathrm{d}z} = c_i C_{i2} - \frac{1}{\rho_i c_i} \frac{\mathrm{d}p}{\mathrm{d}z}
\tag{B.24}
$$

$$
C_{i1} = \frac{\sum_j \Gamma_{j\to i}}{\epsilon_i \rho_i c_i} - \frac{1}{A} \frac{\mathrm{d}A}{\mathrm{d}z}
\tag{B.25}
$$

$$
C_{i2} = \frac{\sum_j \left[\left(c_{if,ij} - c_i \right) \Gamma_{j\to i} + M_{j\to i} \right]}{\epsilon_i \rho_i c_i^2}
\tag{B.26}
$$

$$
C_{i3} = \frac{\sum_j \left[\Gamma_{j\to i} \left(h_{i,j} - h_i + c_{if,ij} c_i - c_i^2 \right) + a_{if,ij} \dot{q}_{j\to i} + M_{j\to i} c_{if,ij} \right]}{\epsilon_i \rho_i c_i h_i}
\tag{B.27}
$$

The change in interfacial area density of the dispersed phase is given based on eq. (5.60) as

$$
\frac{\mathrm{d}a_{if,d}}{\mathrm{d}z} = a_{if,d} \left[C_{d4} + \frac{2}{3} \rho_d \left(\left. \frac{\partial v_d}{\partial p} \right|_{h_d} \frac{\mathrm{d}p}{\mathrm{d}z} + \left. \frac{\partial v_d}{\partial h_d} \right|_p \frac{\mathrm{d}h_d}{\mathrm{d}z} \right) - \frac{1}{c_i} \frac{\mathrm{d}c}{\mathrm{d}z} - \frac{1}{A} \frac{\mathrm{d}A}{\mathrm{d}z} \right] \quad,
\tag{B.28}
$$

$$
C_{d4} = \frac{2}{3} \frac{\Gamma_{c\to d}}{\epsilon_d \rho_d c_d} + \frac{\Phi_d}{a_{if,d} c_d} \quad.
\tag{B.29}
$$

B.4   EFFECTIVE–ADAPTED–JET APPROXIMATION

For a simplified treatment of the adaptation of the steam nozzle exit pressure p_e to the ambient pressure p_∞ (or p_w for channel DCC), the effective-adapted-jet approximation is used. Here, the nozzle exit diameter is replaced by an equivalent diameter which would be required for an adapted exit state, i.e. $p_e = p_\infty$.

The numerical procedure consists of the following steps:

1. The adapted thermodynamic state is obtained from the equation of state as a function of the exit entropy s_e and the adapted pressure p_∞.

2. The adapted velocity is determined from the total enthalpy conservation:

$$c_{adapted} = \sqrt{2 \left(h_e - h_{adapted} \right) + c_e^2}$$ (B.30)

3. The equivalent diameter is determined from the condition of mass continuity:

$$d_{equiv} = d_e \cdot \sqrt{\frac{\rho_e c_e}{\rho_{adapted} c_{adapted}}}$$ (B.31)

B.5 NUMERICAL ROOT FINDING

Functions that cannot be solved explicitly are approximated using numerical root finding algorithms[3] as implemented by the GNU Scientific Library (Gough, 2009).

For a single function $f(x) = 0$, x is determined based on the Brent-Dekker root bracketing algorithm (Brent, 1971; Bus and Dekker, 1975):

> *The root bracketing algorithms require an initial interval which is guaranteed to contain a root – if a and b are the endpoints of the interval then $f(a)$ must differ in sign from $f(b)$. [...] The Brent-Dekker method combines an interpolation strategy with the bisection algorithm. This produces a fast algorithm which is still robust.* (Gough, 2009)

For multiple functions $f_i(x_1, \ldots, x_n) = 0$, a multidimensional root finding algorithm based on a modified version of Powell's Hybrid method (Powell, 1970a,b) is used:

> *The problem of multidimensional root finding requires the simultaneous solution of n equations, f_i, in n variables, x_i,*
>
> $$f_i(x_1, \ldots, x_n) = 0 \quad \text{for } i = 1 \ldots n.$$
>
> *All algorithms proceed from an initial guess using a variant of the Newton iteration,*
> $$x \to x' = x - J^{-1} f(x)$$
> *where x, f are vector quantities and J is the Jacobian matrix $J_{ij} = \partial f_i / \partial x_j$. [...] They require an initial guess for the location of the root, [which] must be sufficiently close to the root. [...] The modified version of the Hybrid algorithm replaces calls to the Jacobian function by its finite difference approximation.* (Gough, 2009)

---

3 `gsl_root_fsolver_brent, gsl_multiroot_fsolver_hybrids`

C | JET HALF RADIUS IN ONE-DIMENSIONAL MODELS

For an axisymmetric, two-dimensional jet with a Gauss-shaped radial velocity profile

$$\frac{c(r)}{c(0)} = \frac{c(r)}{c_0} = \exp\left[-\ln 2 \left(\frac{r}{r_{0.5}}\right)^2\right] \tag{5.5 revisited}$$

and a radially constant density profile $\rho(r) = \rho_m$, the mass flow rate is given as

$$\int_0^\infty \rho c(r)\, r\, \mathrm{d}r = \rho_m c_0 \int_0^\infty \exp\left[-\ln 2 \left(\frac{r}{r_{0.5}}\right)^2\right] r\, \mathrm{d}r \quad . \tag{C.1}$$

Substitution of $x := \sqrt{\ln 2}\, \frac{r}{r_{0.5}}$ yields

$$\int_0^\infty \rho c(r)\, r\, \mathrm{d}r = \frac{\rho_m c_0 r_{0.5}^2}{\ln 2} \int_0^\infty x \exp\left(-x^2\right) \mathrm{d}x = \frac{\rho_m c_0 r_{0.5}^2}{2\ln 2} \quad . \tag{C.2}$$

In analogy, the momentum flow rate can be expressed as

$$\int_0^\infty \rho c(r)^2\, r\, \mathrm{d}r = \frac{\rho_m c_0^2 r_{0.5}^2}{4\ln 2} \quad . \tag{C.3}$$

In a one-dimensional model with an area-averaged velocity $c(r) = c_m$ and an outer jet radius R, the mass and momentum flow rates can be expressed as

$$\int_0^\infty \rho c(r)\, r\, \mathrm{d}r = \tfrac{1}{2}\rho_m c_m R^2 \quad , \tag{C.4}$$

$$\int_0^\infty \rho c(r)^2\, r\, \mathrm{d}r = \tfrac{1}{2}\rho_m c_m^2 R^2 \quad . \tag{C.5}$$

Combination of eq. (C.2) with eq. (C.4) and eq. (C.3) with eq. (C.5) allows to express the jet half radius as a function of the one-dimensional jet radius:

$$\left.\begin{array}{r} c_0 r_{0.5}^2 = \ln 2 \cdot c_m R^2 \\ c_0^2 r_{0.5}^2 = 2\ln 2 \cdot c_m^2 R^2 \end{array}\right\} \Rightarrow \quad r_{0.5} = \sqrt{\frac{\ln 2}{2}}\, R \tag{C.6}$$

In the DCC model developed in chapter 5, the condensation-induced liquid jet consists of two regions: The inner water jet (index l, $r \leq R_{2ph}$) and the surrounding annular water layer (index w, $R_{2ph} < r \leq R_w$). Neglecting density differences ($\rho_l = \rho_w = \rho_m$), the mass and momentum flow rates are then given as

$$\int_0^\infty \rho c(r)\, r\, \mathrm{d}r = \rho_m \left[\tfrac{1}{2} c_l R_{2ph}^2 + \tfrac{1}{2} c_w \left(R_w^2 - R_{2ph}^2 \right) \right] \quad , \tag{C.7}$$

$$\int_0^\infty \rho c(r)^2\, r\, \mathrm{d}r = \rho_m \left[\tfrac{1}{2} c_l^2 R_{2ph}^2 + \tfrac{1}{2} c_w^2 \left(R_w^2 - R_{2ph}^2 \right) \right] \quad . \tag{C.8}$$

Combination of eq. (C.2) with eq. (C.7) and eq. (C.3) with eq. (C.8) allows to express the jet half radius as a function of the one-dimensional jet radius:

$$r_{0.5} = \sqrt{\frac{\ln 2}{2}} \frac{c_l R_{2ph}^2 + c_w \left(R_w^2 - R_{2ph}^2 \right)}{\sqrt{c_l^2 R_{2ph}^2 + c_w^2 \left(R_w^2 - R_{2ph}^2 \right)}} \tag{5.108 revisited}$$

D | SIMULATION RESULTS

D.1   STEAM NOZZLE EXPANSION

The complete simulation results for the steam expansion experiments by Gyarmathy (2005) are shown in fig. D.1.

D.2   DIRECT CONTACT CONDENSATION

The complete simulation results for pool DCC are given in fig. D.2 (jet penetration length), fig. D.3 (axial temperature profile) and fig. D.4 (jet half radius).

NOZZLE	TEST RUN DESIGNATION	STAGNATION STATE	
		PRESSURE p_0/bar	TEMPERATURE $T_0/^\circ\mathrm{C}$
2–M	36–A	106.92	389.22
	40–D	108.88	364.36
	40–E	108.88	346.08
4–B	18–B	100.7	365.53
	18–C	100.7	342.20
5–B	23–A	100.7	389.60
	23–B	100.7	368.74
	23–C	100.7	347.55
6–B	26–B	61.47	324.78
	26–C	61.47	300.93

Table D.1: Stagnation conditions of the experiments by Gyarmathy (2005)
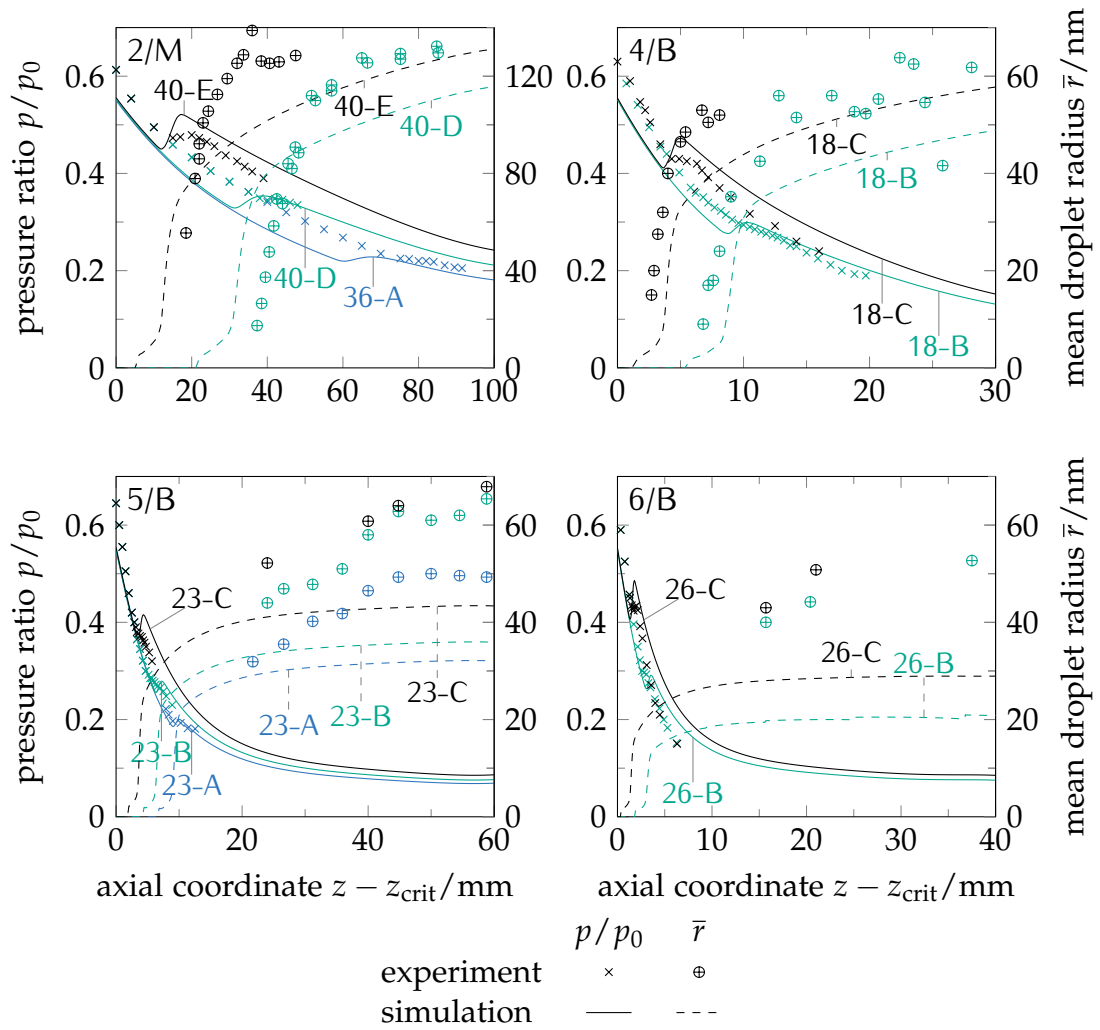
Figure D.1: Simulation of experiments by Gyarmathy (2005), showing pressure distribution p/p_0 and average droplet radius $\bar{r}$ in the divergent nozzle section. Stagnation conditions and test run designations according to table D.1.
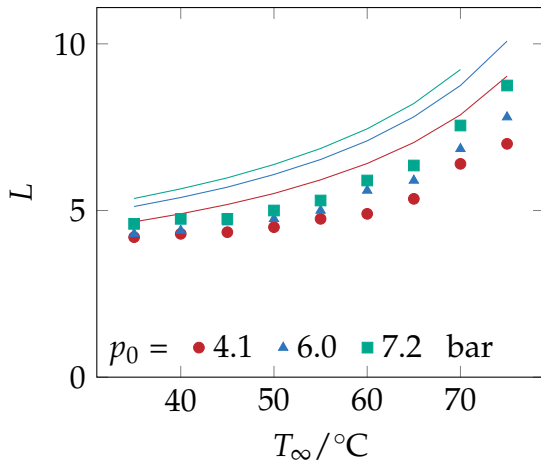
(a) H. Y. Kim et al. (2001)
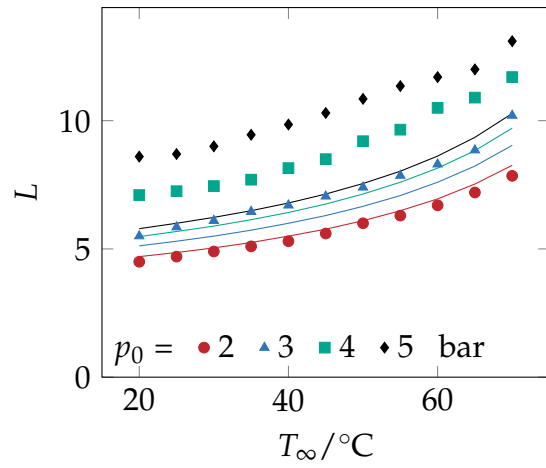
(b) Wu et al. (2007) (nozzle A)
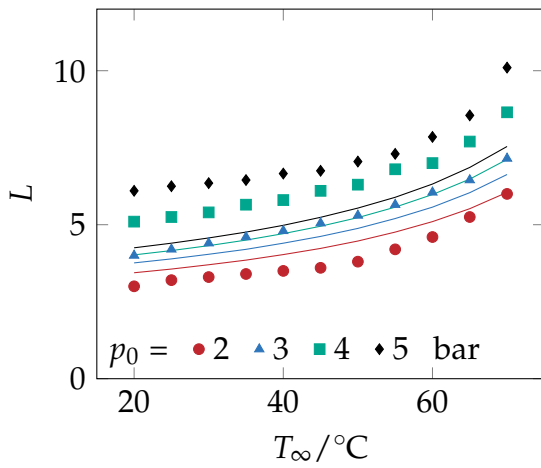
(c) Wu et al. (2007) (nozzle B)
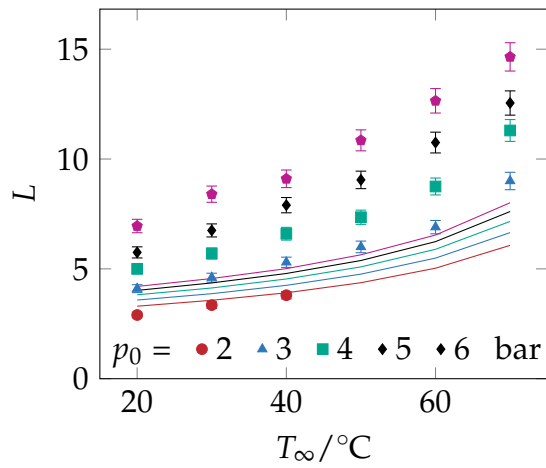
(d) Wu et al. (2009a)
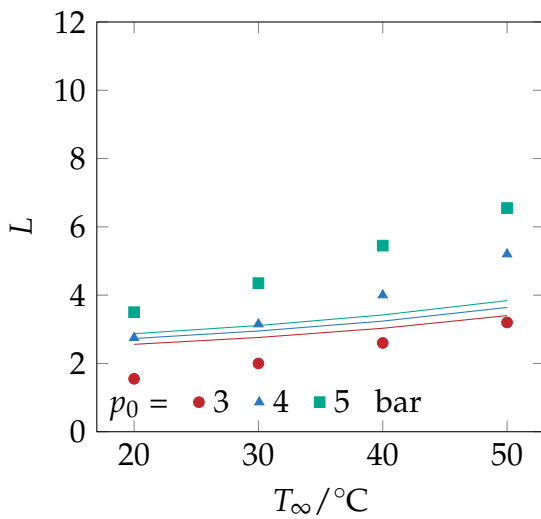
(e) Wu et al. (2010a)

Figure D.2

Dimensionless penetration length L for different pool temperatures T_∞ and steam stagnation pressures p_0: Comparison between experimental data (symbols) and calculated values (solid lines)
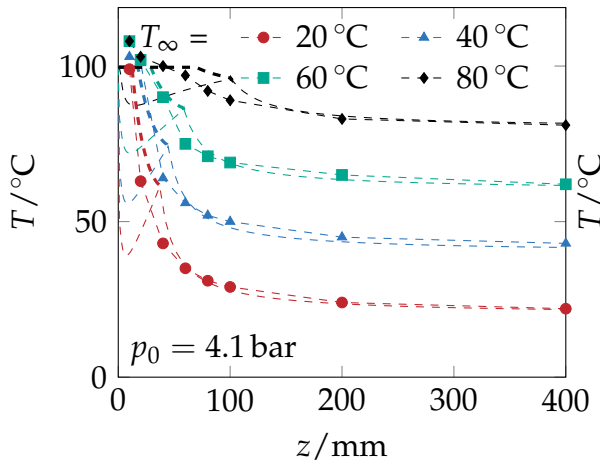
(a) H. Y. Kim et al. (2001) (10.15 mm nozzle)
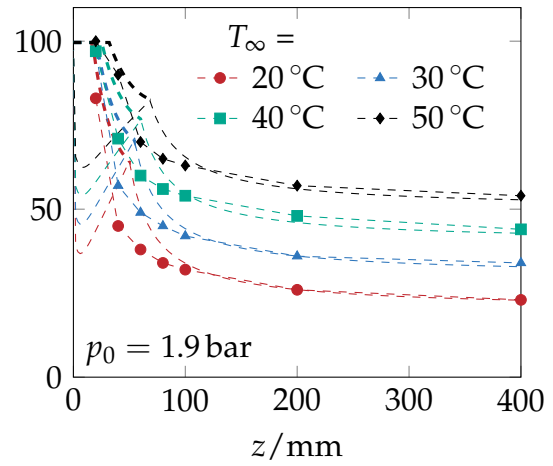
(b) H. Y. Kim et al. (2001) (20 mm nozzle)
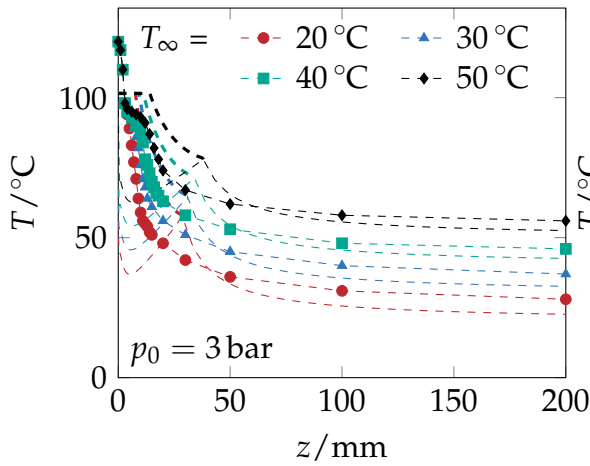
(c) Wu et al. (2010a) ($p_0 = 3$ bar)
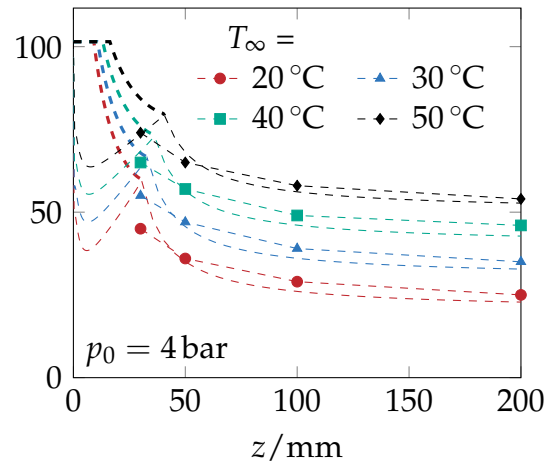
(d) Wu et al. (2010a) ($p_0 = 4$ bar)
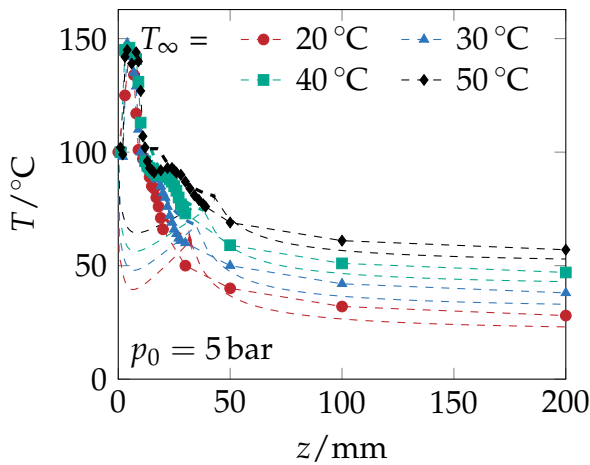
(e) Wu et al. (2010a) ($p_0 = 5$ bar)

Figure D.3

Axial temperature profile: Experimental values for different pool temperatures T_∞ (symbols and dotted lines) and respective simulation results for the mean temperature T_m in the two-phase region (thick solid lines) and the liquid temperature T_l (thin solid lines).
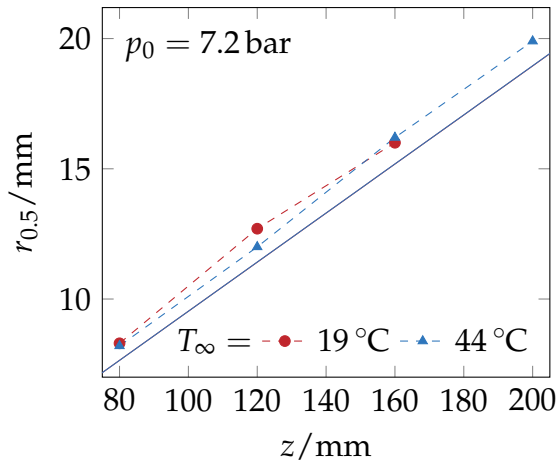
(a) Y.-S. Kim and Youn (2008)
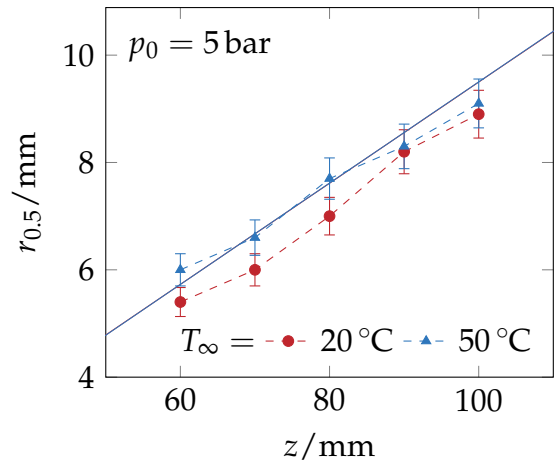
(b) Wu et al. (2010b)
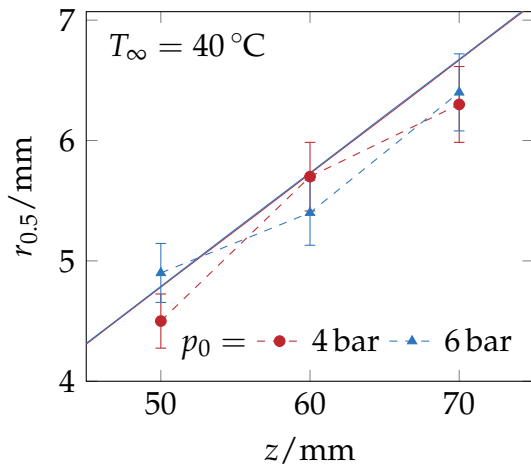
(c) Wu et al. (2010b)

Figure D.4

Jet half radius $r_{0.5}$ along the jet axis z for the condensation-induced liquid jet: Experimental values at different stagnation pressures p_0 and pool temperatures T_∞ (symbols and dashed lines) and respective simulation results (solid lines)

LIST OF FIGURES

LIST OF TABLES

REFERENCES

Abe, Y., Y. Kawamoto, C. Iwaki, T. Narabayashi, M. Mori, and S. Ohmori (2005). "Development of Technologies on Innovative-Simplified Nuclear Power Plant using High-Efficiency Steam Injectors (5) Operating Characteristics of Center Water Jet Type Supersonic Steam Injector". In: *Proceedings of the 13th International Conference on Nuclear Engineering (ICONE-13)*. Beijing.

– (2006). "Development of Technologies on Innovative-Simplified Nuclear Power Plant using High-Efficiency Steam Injectors (12) Evaluations of spatial distributions of flow and heat transfer in steam injector". In: *Proceedings of the 14th International Conference on Nuclear Engineering (ICONE-14)*. Miami.

Anand, G. (1993). "Phenomenological and mathematical modeling of a high pressure steam driven jet injector". PhD thesis. Columbus: Ohio State University.

Anglart, H. and O. Nylund (1996). "CFD application to prediction of void distribution in two-phase bubbly flows in rod bundles". In: *Nuclear Engineering and Design* 163.1–2, pp. 81–98.

Aya, I. and H. Nariai (1991). "Evaluation of heat-transfer coefficient at direct-contact condensation of cold water and steam". In: *Nuclear Engineering and Design* 131.1, pp. 17–24.

Bakhtar, F., J. B. Young, A. J. White, and D. A. Simpson (2005). "Classical Nucleation Theory and Its Application to Condensing Steam Flow Calculations". In: *Proceedings of the Institution of Mechanical Engineers, Part C: Journal of Mechanical Engineering Science* 219.12, pp. 1315–1333.

Band, S., S. Borghoff, U. Büttner, D. H. Eberhardt, J. Kaulard, Y. Kilian-Hülsmeyer, M. Maqua, O. Mildenberger, T. Schimpfke, M. Sonnenkalb, T. Stahl, S. Weiß, and N. Wetzel (2015). *Fukushima-Daiichi 11. März 2011 - Unfallablauf, Radiologische Folgen*. 4., überarbeitete Auflage. GRS-S-55. Gesellschaft für Anlagen- und Reaktorsicherheit (GRS).

Banerjee, S. (1990). "Turbulence structure and transport mechanisms at interfaces". In: *Proc. Ninth Int. Heat Transfer Conference*. Vol. 1. Jerusalem, Israel: Hemisphere Publ., pp. 395–418.

Banerjee, S., D. Lakehal, and M. Fulgosi (2004). "Surface divergence models for scalar exchange between turbulent streams". In: *International Journal of Multiphase Flow* 30.7–8, pp. 963–977.

Banerjee, S., D. S. Scott, and E. Rhodes (1968). "Mass Transfer to Falling Wavy Liquid Films in Turbulent Flow". In: *Industrial & Engineering Chemistry Fundamentals* 7.1, pp. 22–27.

Bankoff, S. G. (1980). "Some condensation studies pertinent to LWR safety". In: *International Journal of Multiphase Flow* 6.1–2, pp. 51–67.

Barschdorff, D. (1971). "Verlauf der Zustandsgrößen und gasdynamische Zusammenhänge bei der spontanen Kondensation reinen Wasserdampfes in Lavaldüsen". In: *Forschung im Ingenieurwesen* 37, pp. 146–157.

Becker, H. A., H. C. Hottel, and G. C. Williams (1963). "Mixing and flow in ducted turbulent jets". In: *Symposium (International) on Combustion* 9.1, pp. 7–20.

Becker, R. and W. Döring (1935). "Kinetische Behandlung der Keimbildung in übersättigten Dämpfen". In: *Annalen der Physik* 416.8, pp. 719–752.

Beithou, N. and H. S. Aybar (2001a). "High-Pressure Steam-Driven Jet Pump—Part I: Mathematical Modeling". In: *Journal of En-*

gineering for Gas Turbines and Power 123.3, pp. 693–700.

Beithou, N. and H. S. Aybar (2001b). "High-Pressure Steam-Driven Jet Pump—Part II: Parametric Analysis". In: *Journal of Engineering for Gas Turbines and Power* 123.3, pp. 701–706.

Bontozoglou, V. and T. J. Hanratty (1989). "Wave height estimation in stratified gas-liquid flows". In: *AIChE Journal* 35.8, pp. 1346–1350.

Brent, R. P. (1971). "An algorithm with guaranteed convergence for finding a zero of a function". In: *The Computer Journal* 14.4, pp. 422–425.

Brucker, G. G. and E. M. Sparrow (1977). "Direct contact condensation of steam bubbles in water at high pressure". In: *International Journal of Heat and Mass Transfer* 20.4, pp. 371–381.

Bus, J. C. P. and T. J. Dekker (1975). "Two efficient algorithms with guaranteed convergence for finding a zero of a function". In: *ACM Transactions on Mathematical Software (TOMS)* 1.4, pp. 330–345.

Carlson, K. E., R. A. Riemke, S. Z. Rouhani, R. W. Shumway, and W. L. Weaver (1995). *RELAP5/MOD3 Code Manual Volume I: Code Structure, System Models and Solution Methods*. Technical Report NUREG/CR-5535; INEL-95/0174. Washington, D.C.: U.S. Nuclear Regulatory Commission.

Cattadori, G., L. Galbiati, L. Mazzocchi, and P. Vanini (1995). "A single-stage high pressure steam injector for next generation reactors: Test results and analysis". In: *International Journal of Multiphase Flow* 21.4, pp. 591–606.

Celata, G. P., M. Cumo, F. D'Annibale, and G. E. Farello (1991). "Direct contact condensation of steam on droplets". In: *International Journal of Multiphase Flow* 17.2, pp. 191–211.

Chan, C. K. and C. K. B. Lee (1982). "A regime map for direct contact condensation". In: *International Journal of Multiphase Flow* 8.1, pp. 11–20.

Chan, S. H., Y. S. Wang, and C. C. Tan (1994). "The effect of mass transfer on Kelvin-Helmholtz instability at the gas-liquid interface of a sonic reacting and non-reacting gas jet submerged in a liquid". In: *International Journal of Heat and Mass Transfer* 37.7, pp. 1123–1132.

Chawla, T. C. (1975a). "Rate of liquid entrainment at the gas-liquid interface of a liquid submerged sonic gas jet". In: *Nuclear Science and Engineering* 56.1, pp. 1–6.

– (1975b). "The Kelvin-Helmholtz instability of the gas-liquid interface of a sonic gas jet submerged in a liquid". In: *Journal of Fluid Mechanics* 67.03, pp. 513–537.

Chen, L.-D. and G. M. Faeth (1982). "Condensation of Submerged Vapor Jets in Subcooled Liquids". In: *Journal of Heat Transfer* 104.4, pp. 774–780.

Chun, M.-H. and Y.-S. Kim (1996). "Direct Condensation of Steam Jets in Subcooled Water". In: *Transactions of the American Nuclear Society* 75.

Chun, M.-H., Y.-S. Kim, and J.-W. Park (1996). "An investigation of direct condensation of steam jet in subcooled water". In: *International Communications in Heat and Mass Transfer* 23.7, pp. 947–958.

Combes, C.-P.-M. (1859). "Sur l'injecteur automoteur de chaudières à vapeur imagine par M. Giffard". Trans. by Combes, 1860. In: *Annales des Mines* 15.5, pp. 169–184.

– (1860). "On giffard's automatic injector for steam boilers". In: *Journal of the Franklin Institute* 69.5, pp. 325–332. Translation of Combes, 1859.

Cooper, J. R., ed. (1994). *IAPWS Release on Surface Tension of Ordinary Water Substance*. URL: http://www.iapws.org/relguide/surf.pdf (visited on 11/07/2012).

Courtney, W. G. (1961). "Remarks on Homogeneous Nucleation". In: *The Journal of Chemical Physics* 35.6, pp. 2249–2250.

Dahikar, S. K., M. J. Sathe, and J. B. Joshi (2010). "Investigation of flow and temperature patterns in direct contact condensation using PIV, PLIF and CFD". In: *Chemical Engineering Science* 65.16, pp. 4606–4620.

Danckwerts, P. V. (1951). "Significance of Liquid-Film Coefficients in Gas Absorp-

tion". In: *Industrial & Engineering Chemistry* 43.6, pp. 1460–1467.

Deberne, N., J. F. Leone, A. Duque, and A. Lallemand (1999). "A model for calculation of steam injector performance". In: *International Journal of Multiphase Flow* 25.5, pp. 841–855.

Deberne, N., J.-F. Leone, and A. Lallemand (2000). "Local measurements in the flow of a steam injector and visualisation". In: *International Journal of Thermal Sciences* 39.9-11, pp. 1056–1065.

Del Tin, G., E. Lavagno, and M. Malandrone (1984). "Experimental study on steam jet condensation in subcooled water pool". In: *Multi-Phase Flow and Heat Transfer III. Part A: Fundamentals*, pp. 134–136.

Delale, C. F. and D. G. Crighton (1998). "Prandtl-Meyer flows with homogeneous condensation. Part 1. Subcritical flows". In: *Journal of Fluid Mechanics* 359, pp. 23–47.

Delale, C. F., G. H. Schnerr, and M. E. H. v. Dongen (2007). "Condensation Discontinuities and Condensation Induced Shock Waves". In: *Shock Wave Science and Technology Reference Library*. Ed. by M. E. H. v. Dongen. Berlin, Heidelberg: Springer, pp. 187–230.

Dibelius, G., K. Mertens, and R. Pitt (1983). "Untersuchungen über die Kondensation in Turbinen zur Trennung von Gasgemischen". In: *VDI-Berichte* 487, pp. 137–187.

Dumaz, P., G. Geffraye, V. Kalitvianski, E. Verloo, M. Valisi, P. Méloni, A. Achilli, R. Schilling, M. Malacka, and M. Trela (2005). "The DEEPSSI project, design, testing and modeling of steam injectors". In: *Nuclear Engineering and Design* 235.2-4, pp. 233–251.

Dumaz, P. and B. Duc (1997). "Status of Steam Injector Studies at CEA". In: *Proceedings of The 5th International Conference on Nuclear Engineering (ICONE-05)*. Nice.

– (2003). "High pressure steam water injector comprising an axial drain". U.S. pat. 6595163. Commissariat a l'Energie Atomique.

Ehrler, F. and K. Schaber (2006). "Spontane Kondensation und Aerosolbildung". In: *VDI-Wärmeatlas*. 10th ed. Berlin, Heidelberg: Springer-Verlag, Je1–Je31.

Epstein, M. and H. K. Fauske (2001). "Applications of the Turbulent Entrainment Assumption to Immiscible Gas-Liquid and Liquid-Liquid Systems". In: *Chemical Engineering Research and Design* 79.4, pp. 453–462.

Epstein, M., H. K. Fauske, and N. Yoshioka (2005). "Establishment of Analytical Model for Peak Temperature Within a Sodium-Water Reaction Jet, (II) Mean Droplet Size in a Submerged Gas Jet". In: *Journal of Nuclear Science and Technology* 42.11, pp. 961–969.

Fang, X., Y. Xu, and Z. Zhou (2011). "New correlations of single-phase friction factor for turbulent pipe flow and evaluation of existing single-phase friction factor correlations". In: *Nuclear Engineering and Design*. The International Conference on Structural Mechanics in Reactor Technology (SMiRT19) Special Section 241.3, pp. 897–902.

Fauske, H. K. and M. A. Grolmes (1992). "Mitigation of hazardous emergency release source terms via quench tanks". In: *Plant/Operations Progress* 11.2, pp. 121–125.

Feder, J., K. Russell, J. Lothe, and G. Pound (1966). "Homogeneous nucleation and growth of droplets in vapours". In: *Advances in Physics* 15.57, pp. 111–178.

Fehlberg, E. (1969). *Low-order classical Runge-Kutta formulas with stepsize control and their application to some heat transfer problems*. Technical Report TR R-315. Washington, D.C.: National Aeronautics and Space Administration.

Flügel, G. (1939). "Berechnung von Strahlapparaten". In: *Forschung auf dem Gebiete des Ingenieurwesens* 10.B.

Fortescue, G. E. and J. R. A. Pearson (1967). "On gas absorption into a turbulent liquid". In: *Chemical Engineering Science* 22.9, pp. 1163–1176.

Fujikawa, S., T. Yano, and M. Watanabe (2011). *Vapor-Liquid Interfaces, Bubbles and Droplets: Fundamentals and Applications*. Berlin, Heidelberg: Springer.

Fukuichi, A., Y. Abe, A. Fujiwara, Y. Kawamoto, C. Iwaki, T. Narabayashi, M.

Mori, and S. Ohmori (2009). "Study on Turbulent Behavior of Water Jet in Supersonic Steam Injector". In: *Journal of Power and Energy Systems* 3.1, pp. 289–300.

Gautier, G.-M. and P. Aujollet (1999). "Pressurized water supply device for a steam injector water source". U.S. pat. 5896435. Commissariat a l'Energie Atomique.

Gerber, A. and M. Kermani (2004). "A pressure based Eulerian–Eulerian multi-phase model for non-equilibrium condensation in transonic steam flow". In: *International Journal of Heat and Mass Transfer* 47.10-11, pp. 2217–2231.

Görtler, H. (1942). "Berechnung von Aufgaben der freien Turbulenz auf Grund eines neuen Näherungsansatzes". In: *ZAMM - Journal of Applied Mathematics and Mechanics / Zeitschrift für Angewandte Mathematik und Mechanik* 22.5, pp. 244–254.

Gough, B., ed. (2009). *GNU Scientific Library Reference Manual - Third Edition*. 3rd Revised edition. Bristol: Network Theory Ltd.

Guelfi, A., D. Bestion, M. Boucker, P. Boudier, P. Fillion, M. Grandotto, J.-M. Hérard, E. Hervieu, and P. Péturaud (2007). "NEPTUNE: A New Software Platform for Advanced Nuclear Thermal Hydraulics". In: *Nuclear Science and Engineering* 156.3, pp. 281–324.

Guha, A. (1992). "Jump conditions across normal shock waves in pure vapour-droplet flows". In: *Journal of Fluid Mechanics* 241, pp. 349–369.

Guha, A. (1994). "A unified theory of aerodynamic and condensation shock waves in vapor-droplet flows with or without a carrier gas". In: *Physics of Fluids* 6.5, pp. 1893–1913.

Guildenbecher, D. R., C. López-Rivera, and P. E. Sojka (2009). "Secondary atomization". In: *Experiments in Fluids* 46.3, pp. 371–402.

Gulawani, S. S., S. S. Deshpande, J. B. Joshi, M. S. Shah, C. S. R. Prasad, and D. S. Shukla (2007). "Submerged Gas Jet into a Liquid Bath: A Review". In: *Industrial & Engineering Chemistry Research* 46.10, pp. 3188–3218.

Gulawani, S. S., S. K. Dahikar, C. S. Mathpati, J. B. Joshi, M. S. Shah, C. S. RamaPrasad, and D. S. Shukla (2009). "Analysis of flow pattern and heat transfer in direct contact condensation". In: *Chemical Engineering Science* 64.8, pp. 1719–1738.

Gulawani, S. S., J. B. Joshi, M. S. Shah, C. S. RamaPrasad, and D. S. Shukla (2006). "CFD analysis of flow pattern and heat transfer in direct contact steam condensation". In: *Chemical Engineering Science* 61.16, pp. 5204–5220.

Gyarmathy, G. (2005). "Nucleation of Steam in High-Pressure Nozzle Experiments". In: *Proceedings of the Institution of Mechanical Engineers, Part A: Journal of Power and Energy* 219.6, pp. 511–521.

Hanratty, T. J. (1991). "Separated flow modelling and interfacial transport phenomena". In: *Applied Scientific Research* 48.3-4, pp. 353–390.

Hedbäck, A. J. W. (1982). "Theorie der spontanen Kondensation in Düsen und Turbinen". PhD thesis. Zürich: Eidgenössische Technische Hochschule Zürich.

Heims, S. P. (1958). *Prandtl-Meyer expansion of chemically reacting gases in local chemical and thermodynamic equilibrium*. NACA Technical Note 4230. Washington, D.C.: National Advisory Committee for Aeronautics.

Heinze, D., T. Schulenberg, and L. Behnke (2012). "Verwendung einer Dampfstrahlpumpe zur passiven Not- und Nachkühlung während eines Station Blackouts". In: *Tagungsband der Jahrestagung Kerntechnik 2012*. Stuttgart, Germany.

– (2013). "Modeling of steam expansion in a steam injector by means of the classical nucleation theory". In: *Proceedings of The 15th International Topical Meeting on Nuclear Reactor Thermal Hydraulics (NURETH-15)*. Pisa, Italy.

– (2014a). "Simulation of direct contact condensation of steam jets submerged in subcooled water by means of a one-dimensional two-fluid model". In: *Proceedings of the 10th International Conference on Heat Transfer, Fluid Mechanics and Thermodynamics (HEFAT2014)*. Orlando, USA.

– (2015). "A Physically Based, One-Dimensional Two-Fluid Model for Direct Contact Condensation of Steam Jets Submerged in Subcooled Water". In: *Journal of Nuclear Engineering and Radiation Science* 1.2, pp. 021002-1–021002-8.

Heinze, D., T. Schulenberg, A. Class, and L. Behnke (2014b). "Simulation of direct contact condensation of steam jets based on interfacial instability theories". In: *Bulletin of the American Physical Society*. Vol. 59. San Francisco, USA.

Henstock, W. H. and T. J. Hanratty (1976). "The interfacial drag and the height of the wall layer in annular flows". In: *AIChE Journal* 22.6, pp. 990–1000.

– (1979). "Gas absorption by a liquid layer flowing on the wall of a pipe". In: *AIChE Journal* 25.1, pp. 122–131.

Higbie, R. (1935). "The rate of absorption of pure gas into a still liquid during short periods of exposure". In: *Transactions of the American Institute of Chemical Engineers* 31, p. 365.

Hill, P. G. (1965). "Turbulent jets in ducted streams". In: *Journal of Fluid Mechanics* 22.1, pp. 161–186.

Howard, R. W. (1984). "Steam driven water injection". U.S. pat. 4440719. General Electric Company.

Hsiang, L.-P. and G. M. Faeth (1992). "Near-limit drop deformation and secondary breakup". In: *International Journal of Multiphase Flow* 18.5, pp. 635–652.

Huber, M. L., R. A. Perkins, D. G. Friend, J. V. Sengers, M. J. Assael, I. N. Metaxa, K. Miyagawa, R. Hellmann, and E. Vogel (2012). "New International Formulation for the Thermal Conductivity of H2O". In: *Journal of Physical and Chemical Reference Data* 41.3, pp. 033102–033125.

Hughes, E. and R. Duffey (1991). "Direct contact condensation and momentum transfer in turbulent separated flows". In: *International Journal of Multiphase Flow* 17.5, pp. 599–619.

Hughmark, G. A. (1967). "Mass and heat transfer from rigid spheres". In: *AIChE Journal* 13.6, pp. 1219–1221.

IAEA, ed. (2009). *Passive Safety Systems and Natural Circulation in Water Cooled Nuclear Power Plants*. IAEA TECDOC 1624. Vienna: International Atomic Energy Agency.

INPO, ed. (2011). *Special Report on the Nuclear Accident at the Fukushima Daiichi Nuclear Power Station*. INPO Special Report 11-005. Atlanta: Institute of Nuclear Power Operations.

Ishii, M. and S. Kim (2004). "Development of one-group and two-group interfacial area transport equation". In: *Nuclear Science and Engineering* 146.3, pp. 257–273. (Visited on 01/24/2014).

Ishii, M. and K. Mishima (1984). "Two-fluid model and hydrodynamic constitutive relations". In: *Nuclear Engineering and Design* 82.2-3, pp. 107–126.

Ishii, M. and T. Hibiki (2011). *Thermo-fluid dynamics of two-phase flow*. 2nd ed. New York: Springer.

Iwaki, C., S. Ohmori, T. Narabayashi, and M. Mori (2005). "Development of Technologies on Innovative-Simplified Nuclear Power Plant using High-Efficiency Steam Injectors (4) PCCS Pool Air-Purge Analysis After LOCA". In: *Proceedings of the 13th International Conference on Nuclear Engineering (ICONE-13)*. Beijing.

Jeje, A., B. Asante, and B. Ross (1990). "Steam bubbling regimes and direct contact condensation heat transfer in highly subcooled water". In: *Chemical Engineering Science* 45.3, pp. 639–650.

Jensen, R. J. (1982). "Interphase transport in horizontal stratified cocurrent flow". PhD thesis. Evanston: Northwestern University.

Kantrowitz, A. (1951). "Nucleation in Very Rapid Vapor Expansions". In: *The Journal of Chemical Physics* 19.9, pp. 1097–1100.

Kerney, P. J., G. M. Faeth, and D. R. Olson (1972). "Penetration characteristics of a submerged steam jet". In: *AIChE Journal* 18.3, pp. 548–553.

Khorsandi, B., S. Gaskin, and L. Mydlarski (2013). "Effect of background turbulence on

an axisymmetric turbulent jet". In: *Journal of Fluid Mechanics* 736, pp. 250–286.

Kim, H. J. and S. G. Bankoff (1983). "Local Heat Transfer Coefficients for Condensation in Stratified Countercurrent Steam-Water Flows". In: *Journal of Heat Transfer* 105.4, pp. 706–712.

Kim, H. J., S. C. Lee, and S. G. Bankoff (1985). "Heat transfer and interfacial drag in countercurrent steam-water stratified flow". In: *International Journal of Multiphase Flow* 11.5, pp. 593–606.

Kim, H. Y., Y. Y. Bae, C. H. Song, J. K. Park, and S. M. Choi (2001). "Experimental study on stable steam condensation in a quenching tank". In: *International Journal of Energy Research* 25.3, pp. 239–252.

Kim, Y.-S., J.-W. Park, and C.-H. Song (2004). "Investigation of the steam-water direct contact condensation heat transfer coefficients using interfacial transport models". In: *International Communications in Heat and Mass Transfer* 31.3, pp. 397–408.

Kim, Y.-S. and Y.-J. Youn (2008). "Experimental study of turbulent jet induced by steam jet condensation through a hole in a water tank". In: *International Communications in Heat and Mass Transfer* 35.1, pp. 21–29.

Kirchner, W. and S. G. Bankoff (1985). "Condensation Effects in Reactor Transients". In: *Nuclear Science and Engineering* 89.4, pp. 310–321.

Kneass, S. L. (1910). *Practice and theory of the injector*. Third Edition. Revised and Enlarged. New York: John Wiley & Sons.

Koizumi, Y., H. Ohtake, N. Yamashita, T. Miyashita, and M. Mori (2005). "Development of Technologies on Innovative-Simplified Nuclear Power Plant using High-Efficiency Steam Injectors (6) Direct Condensation Heat Transfer and Stability of Water Jet in Steam Injector". In: *Proceedings of the 13th International Conference on Nuclear Engineering (ICONE-13)*. Beijing.

Kouremenos, D. and K. Antonopoulos (1989). "Generalized and exact solutions for oblique shock waves of real gases with application to real air". In: *International Journal of Heat and Fluid Flow* 10.4, pp. 328–333.

Kronrod, A. S. (1965). *Nodes and weights of quadrature formulas: sixteen-place tables*. New York: Consultants Bureau.

Kudo, A., T. Egusa, and S. Toda (1974). *Basic study on vapor suppression*. Tech. rep. Babcock-Hitachi Co. Ltd., Kure-shi, Japan. (Visited on 02/19/2013).

Lakehal, D., M. Fulgosi, S. Banerjee, and G. Yadigaroglu (2008a). "Turbulence and heat exchange in condensing vapor-liquid flow". In: *Physics of Fluids* 20.6, p. 065101.

Lakehal, D., M. Fulgosi, and G. Yadigaroglu (2008b). "Direct Numerical Simulation of Condensing Stratified Flow". In: *Journal of Heat Transfer* 130.2, pp. 021501–021501.

Lakehal, D. and M. Labois (2011). "A new modelling strategy for phase-change heat transfer in turbulent interfacial two-phase flow". In: *International Journal of Multiphase Flow* 37.6, pp. 627–639. (Visited on 09/16/2014).

Lamont, J. C. and D. S. Scott (1970). "An eddy cell model of mass transfer into the surface of a turbulent liquid". In: *AIChE Journal* 16.4, pp. 513–519. (Visited on 02/28/2015).

Levich, V. (1962). *Physicochemical Hydrodynamics*. Englewood Cliffs, N.J.: Prentice Hall.

Lewis, W. K. and W. G. Whitman (1924). "Principles of Gas Absorption". In: *Industrial & Engineering Chemistry* 16.12, pp. 1215–1220.

Liang, K.-S. (1991). "Experimental and analytical study of direct contact condensation of steam in water". PhD thesis. Massachusetts Institute of Technology.

Liang, K.-S. and Peter-Griffith (1994). "Experimental and analytical study of direct contact condensation of steam in water". In: *Nuclear Engineering and Design* 147.3, pp. 425–435.

Linehan, J. H., M. Petrick, and M. M. El-Wakil (1969). "On the Interface Shear Stress in Annular Flow Condensation". In: *Journal of Heat Transfer* 91.3, pp. 450–452.

Loth, E. and G. M. Faeth (1989). "Structure of underexpanded round air jets submerged in water". In: *International Journal of Multiphase Flow* 15.4, pp. 589–603.

Ludwig, A. (1975). "Untersuchung zur spontanen Kondensation von Wasserdampf bei stationärer Überschallströmung: Unter Berücksichtigung des Realgasverhaltens". PhD thesis. Karlsruhe: Universität Fridericiana zu Karlsruhe.

Mazzocchi, L. and L. Galbiati (1994). "High pressure steam injector". European pat. EP 0612078 (A1). CISE, S.p.a and ENEL, S.p.a.

Mickley, H. S., R. Ross, A. Squyers, and W. E. Stewart (1954). *Heat, mass, and momentum transfer for flow over a flat plate with blowing or suction*. NACA Technical Note 3208. Washington, D.C.: Massachusetts Inst. of Tech.

Monote, G. (1994). "Atomisation d'un jet liquide par un jet de gaz coaxial: Analyse du mélange (Atomization of a liquid jet by a coaxial gas jet: mixing properties)". PhD thesis. Poitiers: Université de Poitiers.

Moody, L. F. (1944). "Friction factors for pipe flow". In: *Trans. Asme* 66.8, pp. 671–684.

Morton, B. R., G. Taylor, and J. S. Turner (1956). "Turbulent Gravitational Convection from Maintained and Instantaneous Sources". In: *Proceedings of the Royal Society of London. Series A. Mathematical and Physical Sciences* 234.1196, pp. 1–23.

Murata, A., E. Hihara, and T. Saito (1992). "Prediction of heat transfer by direct contact condensation at a steam-subcooled water interface". In: *International Journal of Heat and Mass Transfer* 35.1, pp. 101–109.

Narabayashi, T., H. Miyano, H. Nei, O. Ozaki, W. Mizumachi, and A. Shioiri (1992). "Feasibility study on steam injector driven jet pump for next-generation reactor". In: *Proc. Int. Conf. Design and Safety of Advanced Nuclear Power Plants (ANP'92)*. Vol. IV. Tokyo, Japan, pp. 36.2.1–36.2.7.

Narabayashi, T., H. Miyano, O. Ozaki, W. Mizumachi, A. Tanabe, A. Shioiri, H. Tonegawa, and T. Ishiyama (1993). "Steam injector system". U.S. pat. 5262091. Kabushiki Kaisha Toshiba.

Narabayashi, T., W. Mizumachi, and M. Mori (1997). "Study on two-phase flow dynamics in steam injectors". In: *Nuclear Engineering and Design* 175.1-2, pp. 147–156.

Narabayashi, T., M. Mori, M. Nakamaru, and S. Ohmori (2000). "Study on two-phase flow dynamics in steam injectors: II. High-pressure tests using scale-models". In: *Nuclear Engineering and Design* 200.1-2, pp. 261–271.

Narabayashi, T., Y. Shimadu, T. Murase, M. Nagai, M. Mori, and S. Ohmori (2006). "Development of Technologies on Innovative-Simplified Nuclear Power Plant Using High-Efficiency Steam Injectors (10) Application to A Small District-Heating Reactor". In: *Proceedings of the 14th International Conference on Nuclear Engineering (ICONE-14)*. Miami.

Nikuradse, J. (1933). "Strömungsgesetze in rauhen Rohren". In: *VDI-Forschungsheft 361*.

Oertel, H. J., ed. (2012). *Prandtl - Führer durch die Strömungslehre*. 13th ed. Wiesbaden: Springer Fachmedien.

Ohmori, S., M. Mori, S. Goto, T. Narabayashi, C. Iwaki, and Y. Asanuma (2006). "Development of Technologies on Innovative-Simplified Nuclear Power Plant using High-Efficiency Steam Injectors (9) System outline and Endurance test of Low-Pressure Steam Injectors". In: *Proceedings of the 14th International Conference on Nuclear Engineering (ICONE-14)*. Miami.

Ohmori, S., S. Goto, and M. Mori (2005). "Development of Technologies on Innovative-Simplified Nuclear Power Plant using High-Efficiency Steam Injectors (1) Demonstration test of SI Core Coolant Passive Injection System". In: *Proceedings of the 13th International Conference on Nuclear Engineering (ICONE-13)*. Beijing.

Otobe, Y., S. Matsuo, M. Tanaka, H. Kashimura, and T. Setoguchi (2006). "A Study on Characteristics of Under-Expanded Condensing Jet". In: *JSME International Journal Series B Fluids and Thermal Engineering* 49.4, pp. 1165–1172.

Paras, S. V., N. A. Vlachos, and A. J. Karabelas (1994). "Liquid layer characteristics in stratified—Atomization flow". In: *Interna-*

tional Journal of Multiphase Flow 20.5, pp. 939–956.

Peters, F. and K. Meyer (1995). "Measurement and interpretation of growth of monodispersed water droplets suspended in pure vapor". In: *International Journal of Heat and Mass Transfer* 38.17, pp. 3285–3293.

Petrovic, A. (2005). "Analytical Study of Flow Regimes for Direct Contact Condensation Based on Parametrical Investigation". In: *Journal of Pressure Vessel Technology* 127.1, pp. 20–25.

Petrovic-de With, A. (2006). "Characterisation and modelling of flow mechanisms for direct contact condensation of steam injected into water". PhD thesis. Hatfield: University of Hertfordshire.

Piessens, R., E. de Doncker-Kapenga, C. W. Überhuber, and D. K. Kahaner (1983). *Quadpack. A Subroutine Package for Automatic Integration.* Vol. 1. Springer Series in Computational Mathematics. Berlin, Heidelberg: Springer.

Powell, M. J. D. (1970a). "A FORTRAN subroutine for solving systems of nonlinear algebraic equations". In: *Numerical methods for nonlinear algebraic equations*. Ed. by P. Rabinowitz. London: Gordon & Breach, pp. 115–161.

– (1970b). "A hybrid method for nonlinear equations". In: *Numerical methods for nonlinear algebraic equations*. Ed. by P. Rabinowitz. London: Gordon & Breach, pp. 87–114.

Prandtl, L. (1925). "Bericht über Untersuchungen zur ausgebildeten Turbulenz". Trans. by Prandtl, 1949. In: ZAMM - *Journal of Applied Mathematics and Mechanics / Zeitschrift für Angewandte Mathematik und Mechanik* 5.2, pp. 136–139.

– (1949). *Report on investigation of developed turbulence*. NACA Technical Memorandum 1231. Washington, D.C.: National Advisory Committee for Aeronautics. Translation of Prandtl, 1925.

Pye, J. (2010). *Freesteam: Open source steam property routines in C*. Version 2.0. URL: http://freesteam.sourceforge.net/ (visited on 03/30/2015).

Rajaratnam, N. (1976). *Turbulent Jets*. Developments in Water Science 5. Amsterdam: Elsevier Scientific Publishing Company.

Rashidi, M., G. Hetsroni, and S. Banerjee (1991). "Mechanisms of heat and mass transport at gas-liquid interfaces". In: *International Journal of Heat and Mass Transfer* 34.7, pp. 1799–1810.

Raynal, L. (1997). "Instabilité et entrainement à l'interface d'une couche de mélange liquide-gaz – Instability and entrainment at the interface of a liquid-gas mixing layer". PhD thesis. Grenoble: Université de Grenoble.

Reinsch, A. W. (1995). "Passive decay heat removal and internal depressurization system for nuclear reactors". U.S. pat. 5398267.

Reinsch, A. W., T. G. Hook, K. I. Soplenkov, V. G. Selivanov, V. V. Bredikhin, I. I. Shmal, Y. Filimonov, and Y. N. Pavlenko (1995). "Risk Reduction Potential of Jet Condensers". In: *Progress in design, research and development and testing of safety systems for advanced water cooled reactors*. Vienna: International Atomic Energy Agency.

Richards, C. D. and W. M. Pitts (1993). "Global density effects on the self-preservation behaviour of turbulent free jets". In: *Journal of Fluid Mechanics* 254, pp. 417–435.

Ricou, F. P. and D. B. Spalding (1961). "Measurements of entrainment by axisymmetrical turbulent jets". In: *Journal of Fluid Mechanics* 11.1, pp. 21–32.

Röll, V. v., ed. (1912). *Enzyklopädie des Eisenbahnwesens. Dritter Band: Braunschweigische Eisenbahnen – Eilgut*. 2nd ed. Vol. 3. Berlin, Wien: Urban & Schwarzenberg.

Schmidlin, F. W. (1986). "Hydrokinetic amplifier with high momentum transfer coefficient". U.S. pat. 4580948. Helios Research Corp.

Shah, A. (2012). "Thermal Hydraulic Analysis of Steam Jet Pump". PhD thesis. Pakistan Institute of Engineering & Applied Sciences, Islamabad.

Shah, A., I. R. Chughtai, and M. H. Inayat (2010). "Numerical Simulation of Direct-contact Condensation from a Supersonic

Steam Jet in Subcooled Water". In: *Chinese Journal of Chemical Engineering* 18.4, pp. 577–587.

– (2011). "Experimental and numerical analysis of steam jet pump". In: *International Journal of Multiphase Flow* 37.10, pp. 1305–1314.

– (2014). "Experimental and numerical investigation of the effect of mixing section length on direct-contact condensation in steam jet pump". In: *International Journal of Heat and Mass Transfer* 72, pp. 430–439.

Shah, A., A. H. Khan, I. R. Chughtai, and M. H. Inayat (2013). "Numerical and experimental study of steam-water two-phase flow through steam jet pump". In: *Asia-Pacific Journal of Chemical Engineering* 8.6, pp. 895–905.

Sherif, S., W. Lear, J. Steadham, P. Hunt, and J. Holladay (2000). "Analysis and modeling of a two-phase jet pump of a thermal management system for aerospace applications". In: *International Journal of Mechanical Sciences* 42.2, pp. 185–198.

Sigg, R. (2010). "Numerische Untersuchung von Lastvariationen und Nässephänomenen an einer Niederdruck-Dampfturbine". PhD thesis. Stuttgart: Universität Stuttgart.

Simpson, M. E. and C. K. Chan (1982). "Hydrodynamics of a Subsonic Vapor Jet in Subcooled Liquid". In: *Journal of Heat Transfer* 104.2, pp. 271–278.

Sinclair, A. (1887). *Locomotive engine running and management*. 7th ed. New York: John Wiley & Sons, Inc.

Smolders, H. J. and M. E. H. v. Dongen (1992). "Shock wave structure in a mixture of gas, vapour and droplets". In: *Shock Waves* 2.4, pp. 255–267.

Someya, S., M. Uchida, Y. Li, H. Ohshima, and K. Okamoto (2011). "Entrained droplets in underexpanded gas jet in water". In: *Journal of Visualization* 14.3, pp. 225–236.

Song, C.-H., S. Cho, and H.-S. Kang (2012). "Steam Jet Condensation in a Pool: From Fundamental Understanding to Engineering Scale Analysis". In: *Journal of Heat Transfer* 134.3, pp. 031004-1–031004-15.

Song, C.-H. and Y.-S. Kim (2011). "Direct Contact Condensation of Steam Jet in a Pool". In: *Advances in Heat Transfer* 43, pp. 227–288.

Soplenkov, K. I., V. G. Selivanov, Y. N. Filimontsev, B. I. Nigmatulin, V. V. Bredikhin, E. I. Trubkin, E. Z. Emeljanenko, and A. W. Reinsch (1995). "Design and testing of passive heat removal system with ejector–condenser". In: *Progress in design, research and development and testing of safety systems for advanced water cooled reactors*. Vienna: International Atomic Energy Agency.

Starzmann, J., M. V. Casey, and J. F. Mayer (2012). "Unsteady Numerical Study of Wet Steam Flow in a Low Pressure Steam Turbine". In: *High Performance Computing in Science and Engineering '11*. Ed. by W. E. Nagel, D. B. Kröner, and M. M. Resch. Berlin, Heidelberg: Springer, pp. 437–450.

Steward, F. R. and A. G. Guruz (1977). "Aerodynamics of a Confined Jet with Variable Density". In: *Combustion Science and Technology* 16.1-2, pp. 29–45.

Sube, R. (2001). *Routledge-Langenscheidt German Dictionary of Physics / Wörterbuch Physik Englisch*. London: Routledge.

Surin, V. A., V. N. Evchenko, and V. M. Rubin (1983). "Propagation of a gas jet in a liquid". In: *Journal of engineering physics* 45.4, pp. 1091–1101.

Takahashi, Y., Y. Koizumi, H. Ohtake, T. Miyashita, and M. Mori (2006). "Development of Technologies on Innovative-Simplified Nuclear Power Plant using High-Efficiency Steam Injectors (13) Study on Heat Transfer of Direct Condensation of Steam on Subcooled Water Jet". In: *Proceedings of the 14th International Conference on Nuclear Engineering (ICONE-14)*. Miami.

Taylor, G. I. (1945). *Dynamics of a mass of hot gas rising in air*. LA Technical Report 236. Los Alamos National Laboratory.

Theofanous, T., R. Houze, and L. Brumfield (1976). "Turbulent mass transfer at free, gas-liquid interfaces, with applications to open-channel, bubble and jet flows". In: *International Journal of Heat and Mass Transfer* 19.6, pp. 613–624.

Thompson, M. J. (1950). "A Note on the Calculation of Oblique Shock-Wave Characteristics". In: *Journal of the Aeronautical Sciences (Institute of the Aeronautical Sciences)* 17.11, p. 774.

Tollmien, W. (1926). "Berechnung turbulenter Ausbreitungsvorgänge". Trans. by Tollmien, 1945. In: *ZAMM - Journal of Applied Mathematics and Mechanics / Zeitschrift für Angewandte Mathematik und Mechanik* 6.6, pp. 468–478.

– (1945). *Calculation of turbulent expansion processes*. NACA Technical Memorandum 1085. Washington, D.C.: National Advisory Committee for Aeronautics. Translation of Tollmien, 1926.

Treffinger, P. (1994). "Untersuchungen zur spontanen Kondensation in übersättigten Dämpfen". PhD thesis. Karlsruhe: Universität Fridericiana zu Karlsruhe.

Trela, M., R. Kwidzinski, D. Butrymowicz, and J. Karwacki (2010). "Exergy analysis of two-phase steam-water injector". In: *Applied Thermal Engineering* 30.4, pp. 340–346.

Varga, C. M., J. C. Lasheras, and E. J. Hopfinger (2003). "Initial breakup of a small-diameter liquid jet by a high-speed gas stream". In: *Journal of Fluid Mechanics* 497, pp. 405–434.

Villermaux, E. (1998). "Mixing and Spray Formation in Coaxial Jets". In: *Journal of Propulsion and Power* 14.5, pp. 807–817.

Vivaldi, D., F. Gruy, N. Simon, and C. Perrais (2013). "Modelling of a CO2-gas jet into liquid-sodium following a heat exchanger leakage scenario in Sodium Fast Reactors". In: *Chemical Engineering Research and Design*. Nuclear Process Engineering 91.4, pp. 640–648.

Volmer, M. and A. Weber (1926). "Keimbildung in übersättigten Gebilden". In: *Z. phys. Chem* 119, pp. 277–301.

Wagner, W., J. R. Cooper, A. Dittmann, J. Kijima, H.-J. Kretzschmar, A. Kruse, R. Mareš, K. Oguchi, H. Sato, I. Stöcker, O. Šifner, Y. Takaishi, I. Tanishita, J. Trübenbach, and T. Willkommen (2000). "The IAPWS Industrial Formulation 1997 for the Thermodynamic Properties of Water and Steam". In: *Journal of Engineering for Gas Turbines and Power* 122.1, pp. 150–185.

Wagner, W. and H.-J. Kretzschmar (2008). *International Steam Tables: Properties of Water and Steam Based on the Industrial Formulation IAPWS-IF97 : Tables, Algorithms, Diagrams, and CD-ROM Electronic Steam Tables : All of the Equations of IAPWS-IF97 Including a Complete Set of Supplementary Backward Equations for Fast Calculations of Heat Cycles, Boilers, and Steam Turbines*. Berlin, Heidelberg: Springer.

Weiland, C. and P. P. Vlachos (2013). "Round gas jets submerged in water". In: *International Journal of Multiphase Flow* 48, pp. 46–57.

Weimer, J. C., G. M. Faeth, and D. R. Olson (1973). "Penetration of vapor jets submerged in subcooled liquids". In: *AIChE Journal* 19.3, pp. 552–558.

Weinberg, S. (1952). "Heat transfer to low pressure sprays of water in a steam atmosphere". In: *Proc. Inst. Mech. Engrs, London* 1.6, pp. 240–252.

Wert, K. L. (1995). "A rationally-based correlation of mean fragment size for drop secondary breakup". In: *International Journal of Multiphase Flow* 21.6, pp. 1063–1071.

Wissen, R. J. E. van, K. R. A. M. Schreel, C. W. M. van der Geld, and J. Wieringa (2004). "Turbulence production by a steam-driven jet in a water vessel". In: *International Journal of Heat and Fluid Flow* 25.2, pp. 173–179.

With, A. de (2009). "Steam plume length diagram for direct contact condensation of steam injected into water". In: *International Journal of Heat and Fluid Flow* 30.5, pp. 971–982.

Wolf, T. (1993). "Comment on 'Approximate Formula of Weak Oblique Shock Wave Angle'". In: *AIAA Journal* 31.7, p. 1363.

Wu, X.-Z., J.-J. Yan, W.-J. Li, D.-D. Pan, and D.-T. Chong (2009a). "Experimental study on sonic steam jet condensation in quiescent subcooled water". In: *Chemical Engineering Science* 64.23, pp. 5002–5012.

Wu, X.-Z., J.-J. Yan, W.-J. Li, D.-D. Pan, and G.-Y. Liu (2010a). "Experimental investiga-

tion of over-expanded supersonic steam jet submerged in quiescent water". In: *Experimental Thermal and Fluid Science* 34.1, pp. 10–19.

– (2010b). "Experimental study on a steam-driven turbulent jet in subcooled water". In: *Nuclear Engineering and Design* 240.10, pp. 3259–3266.

Wu, X.-Z., J.-J. Yan, D.-D. Pan, G.-Y. Liu, and W.-J. Li (2009b). "Condensation regime diagram for supersonic/sonic steam jet in subcooled water". In: *Nuclear Engineering and Design* 239.12, pp. 3142–3150.

Wu, X.-Z., J.-J. Yan, S.-F. Shao, Y. Cao, and J.-P. Liu (2007). "Experimental study on the condensation of supersonic steam jet submerged in quiescent subcooled water: Steam plume shape and heat transfer". In: *International Journal of Multiphase Flow* 33.12, pp. 1296–1307.

Xu, Q., L. Guo, S. Zou, J. Chen, and X. Zhang (2013). "Experimental study on direct contact condensation of stable steam jet in water flow in a vertical pipe". In: *International Journal of Heat and Mass Transfer* 66, pp. 808–817.

Xu, Y., X. Fang, X. Su, Z. Zhou, and W. Chen (2012). "Evaluation of frictional pressure drop correlations for two-phase flow in pipes". In: *Nuclear Engineering and Design*. SI : CFD4NRS-3 253, pp. 86–97.

Yan, J.-J., S.-F. Shao, J.-P. Liu, and Z. Zhang (2005). "Experiment and analysis on performance of steam-driven jet injector for district-heating system". In: *Applied Thermal Engineering* 25.8-9, pp. 1153–1167.

Yan, J.-J., X. Wu, D. Chong, and J. Liu (2011). "Experimental Research on Performance of Supersonic Steam-Driven Jet Injector and Pressure of Supersonic Steam Jet in Water". In: *Heat Transfer Engineering* 32.11-12, pp. 988–995.

Young, J. B. and A. Guha (1991). "Normal shock-wave structure in two-phase vapour-droplet flows". In: *Journal of Fluid Mechanics* 228, pp. 243–274.

Young, J. (1995). "The fundamental equations of gas-droplet multiphase flow". In: *International Journal of Multiphase Flow* 21.2, pp. 175–191.

Young, R. J., K. T. Yang, and J. L. Novotny (1974). "Vapor liquid interaction in a high velocity vapor jet condensing in a coaxial water flow". In: *Proc. 5th Int. Heat Transfer Conf., Tokyo*. Vol. 3, pp. 226–230.

Zhang, B., J. Lv, and F. Xue (2011). "An Experimental Study on Water-Steam Two-Phase Injector Performance". In: *Asia-Pacific Power and Energy Engineering Conference (APPEEC)*. Wuhan.

Zierep, J. (1972). *Theoretische Gasdynamik*. Karlsruhe: Braun.

Zong, X., J.-P. Liu, X.-p. Yang, and J.-J. Yan (2015). "Experimental study on the direct contact condensation of steam jet in subcooled water flow in a rectangular mix chamber". In: *International Journal of Heat and Mass Transfer* 80, pp. 448–457.
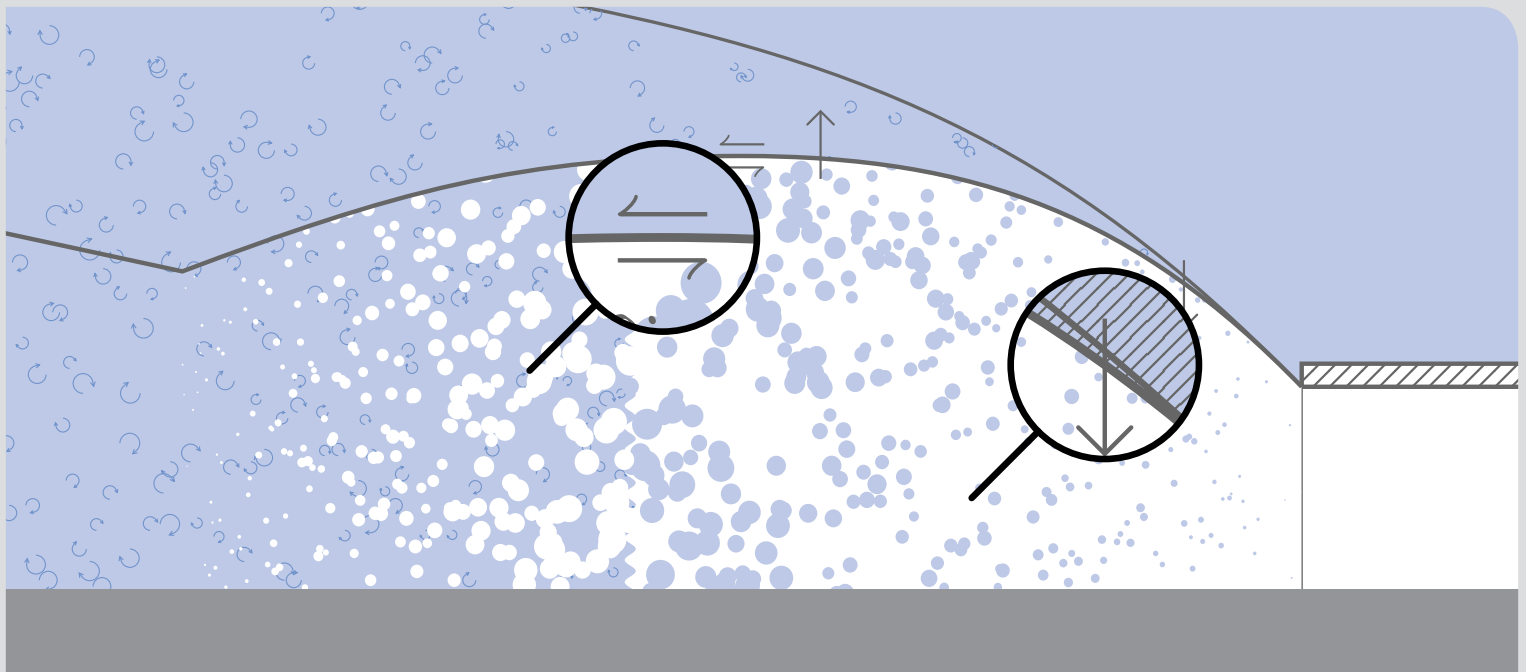
A passive emergency system based on a steam injector could ensure the heat re-
moval from a nuclear reactor core without electric power supply. This book presents
simulation models for the two-phase condensing flow in steam injectors that allow
determination of major flow parameters on a physically sound basis. The investi-
gated phenomena are steam expansion, gas dynamic jet adaptation and direct
contact condensation. The developed models can serve as basis for a universally
valid, computationally efficient simulation tool to be used in thermalhydraulic
system codes for further analysis.